

TECHNISCHE UNIVERSITÄT MÜNCHEN

LEHRSTUHL FÜR LEICHTBAU

**Mechanical characterization and modeling of
extruded and steel-wire-reinforced aluminum sections
with respect to impact loading**

Alexander Morasch

Vollständiger Abdruck der von der Fakultät für Maschinenwesen der Technischen Universität München zur Erlangung des akademischen Grades eines Doktors

Doktor-Ingenieur (Dr.-Ing.)

genehmigten Dissertation.

Vorsitzender: Prof. Dr.-Ing. M. Zäh

Prüfer der Dissertation:

1. Prof. Dr.-Ing. H. Baier
2. Prof. Dr.-Ing., Dr.-Ing. E.h. A. E. Tekkaya
Technische Universität Dortmund

Die Dissertation wurde am 03.12.2015 bei der Technischen Universität München eingereicht und durch die Fakultät für Maschinenwesen am 06.06.2016 angenommen.

Danksagung

Mein Dank gilt Prof. Horst Baier für die Ermöglichung der Promotion am Lehrstuhl für Leichtbau. Meine Berufung in das Beamtenverhältnis auf Zeit als Akademischer Rat und zahlreiche Aufgaben in der Lehre empfand ich als Auszeichnung und die damit verbundene Lehrtätigkeit habe ich jederzeit genossen. Vor allem auch für die fachliche Unterstützung und das vertrauensvolle Verhältnis bedanke ich mich herzlich.

Ebenso geht mein Dank an Prof. A. Erman Tekkaya für stets hilfreiche konstruktive Kritik zu meiner Forschungstätigkeit im Sonderforschungsbereich SFB Transregio 10. Diese hat die wissenschaftliche Aussagekraft der vorliegenden Arbeit wesentlich gesteigert. Für die Übernahme des Prüfungsvorsitzes bedanke ich mich bei Prof. Michael Zäh.

Meinen Kollegen danke ich für die angenehme und freundschaftliche Zusammenarbeit, zahlreiche gewinnbringende Diskussionen und natürlich auch für gemeinsame private Unternehmungen. Hervorheben will ich Dr. Erich Wehrle für die Kooperation im SFB Transregio 10, Herrn Luiz daRocha-Schmidt für die Rechner- und Clusteradministration, sowie meinen Bürokollegen Herrn Peter Krempl für stets hilfreiche Kritik und das erstellte L^AT_EX-Kompendium.

Ein herzliches Vergelt's Gott dem Werkstattpersonal des Lehrstuhls für Leichtbau für die Vorbereitung und die fachkundige Unterstützung bei der Durchführung von Versuchen. Besonders gilt dies für Manfred Bauer für die Hilfe in Sachen Messtechnik und Elektronik.

Ein großes Lob gebührt nicht zuletzt auch den von mir betreuten Studenten und wissenschaftlichen Hilfskräften, ohne deren Engagement und Forschungsergebnisse die vorliegende Dissertation nicht möglich gewesen wäre.

Für die Übernahme des Lektorats bedanke ich mich bei Dr. Erich Wehrle und Herrn Stephan Endler.

Die Forschung zu dieser Dissertation entstand im Rahmen des Sonderforschungsbereichs SFB Transregio 10, Teilprojekt C6, und wurde von der Deutschen Forschungsgemeinschaft (DFG) gefördert.

Acknowledgements

The research presented in this dissertation was carried out within the Collaborative Research Centre SFB/Transregio 10, subproject C6, which was kindly supported by the German Research Foundation (DFG).

Kurzfassung

Hybride Werkstoffe und Faserverbundwerkstoffe kommen vermehrt bei Verkehrsmitteln zum Einsatz und treiben den strukturellen Leichtbau voran. In dieser Arbeit wird ein Verbundwerkstoff aus einer Aluminiummatrix untersucht, welche mit Stahldrähten verstärkt ist. Um dessen strukturmechanisches Verhalten zu erörtern wird eine Materialcharakterisierung durchgeführt, Modelle parametrisiert und experimentell verifiziert. Mit hochdynamischen Impaktversuchen werden Simulationsmodelle validiert und das Strukturverhalten auf Bauteilebene analysiert. Zukünftig zu erwartende Fortschritte in der Werkstoffgestaltung werden simuliert und bewertet.

Abstract

Hybrid and fiber reinforced materials are increasingly applied in modern vehicles and advance lightweight design. This work investigates on a composite material composed of an aluminum matrix reinforced with steel wires. In order to assess its structural-mechanical behavior, the material is characterized, material models are parametrized and experimentally verified. Simulation models for the analysis of the structural behavior are validated using highly dynamic impact tests and prospective progress in the material technology is evaluated by numerical simulation.

Contents

1. Introduction	1
1.1. Motivation	1
1.2. Scientific framework - the collaborative research center Transregio 10	3
1.3. Outline of the thesis	4
2. Basic elasto-plastic properties of steel-wire-reinforced aluminum (SWRA)	6
2.1. Structural stiffness	6
2.2. Structural strength	10
2.3. Influence of the extrusion process on the mechanical properties	12
2.3.1. Influence of the extrusion process on the material's microstructure and strength	12
2.3.2. Thermal residual stresses	14
2.3.3. Effects of thermal residual stresses on structures of steel-wire-reinforced aluminum	16
2.4. Investigations on the suitability of SWRA for energy absorbing structures	18
3. Material models for dynamic impact loading and parameter identification	23
3.1. Basic mathematical descriptions for the behavior of ductile metals . .	23
3.1.1. Measures of strain for infinitesimal and finite strains	24
3.1.2. Isotropic elasticity	26
3.1.3. Plastic yielding	26
3.1.3.1. Isotropic yield functions	28
3.1.3.2. Orthotropic yield functions	29
3.1.4. Plastic strain hardening	33
3.1.4.1. Experimental determination by compression testing .	34
3.1.4.2. Experimental determination by the torsion testing .	35
3.1.4.3. Correction methods for the strain hardening determined from post-necking tensile test data	37
3.1.5. Strain rate and temperature dependent strain hardening . . .	40
3.2. Experimental determination of the plastic properties of aluminum matrix and steel wire	42
3.2.1. Plastic yield surface	43
3.2.2. Strain hardening properties	44
3.2.3. Properties of strain rate dependent hardening	45

3.3.	Properties of the wire-matrix interface	48
3.3.1.	Microstructure of the interface	48
3.3.2.	Experimental determination	48
4.	Description of material failure and fracture	51
4.1.	Mechanisms of material failure and fracture	51
4.2.	Modified Gurson yield function for porous ductile media	52
4.2.1.	Theoretical background	52
4.2.2.	Parameter identification for the shear-modified GTN model for the aluminum matrix	54
4.3.	Phenomenological fracture model for the steel wire	57
4.4.	Failure criterion for the cohesive wire-matrix interface	58
4.5.	Validation of the material and fracture model for SWRA	59
4.5.1.	Tension of SWRA in wire direction	59
4.5.2.	Tension of SWRA perpendicular to wire direction	61
4.6.	Sensitivity analyses of the fracture model of SWRA	63
4.6.1.	Sensitivity toward interface normal strength	64
4.6.2.	Sensitivity toward the wire's fracture strain	65
4.7.	Summary and discussion of the material model for SWRA	66
5.	Performance of SWRA in structural components undergoing high defor- mations and impact loads	69
5.1.	Validation of the simulation methodology on structural level with bolt-pull-out tests	69
5.1.1.	Bolt-pull-out in the non-reinforced aluminum matrix	71
5.1.2.	Bolt-pull-out in SWRA in wire direction	71
5.1.3.	Bolt-pull-out in SWRA perpendicular to wire direction	74
5.1.4.	Summary and discussion of the bolt-pull-out test results	74
5.2.	Axial crushing of extruded non-reinforced and steel-wire-reinforced aluminum crash tubes	75
5.2.1.	Design constraints for axial crash tubes	75
5.2.2.	Quasistatic compression behavior of steel-wire-reinforced crash tubes	78
5.3.	Three-point bending with an impact load	81
5.3.1.	Experimental test setup	81
5.3.2.	Interpretation of test results	81
5.4.	Validation of the simulation methodology by dynamic three-point bending test with an impact load	86
5.5.	Fully clamped section under impact load	87
6.	Outlook on improvements to steel-wire-reinforced aluminum with re- spect to energy absorption	91
6.1.	Improved interface strength	92
6.2.	Increased wire content	93

6.3. Aluminum matrix with higher strain hardening	93
6.4. Summary and discussion of energy absorption of SWRA with prospective improvements	96
7. Conclusion	97
A. Appendix	109
A.1. Mass-specific bending stiffness – SWRA in comparison to non-reinforced aluminum	109
A.2. Temperature-dependent elasto-plastic material properties and CTE of aluminum matrix and steel wire	110
A.2.1. Temperature-dependent CTE	110
A.2.2. Temperature-dependent elasto-plastic material properties . . .	111
A.3. Geometry of the dynamic tensile test specimen	111
A.4. Geometry of flat tensile specimen and flat shear specimen used for identification of the parameters of the shear-modified GTN model . .	112
A.5. Age hardening of EN AW-6060T4(F)	112

List of Figures

1.1.	Lightweight extruded aluminum car frame with circular crash tubes and progressive buckling of the crash tube	3
1.2.	Composite extrusion process and extruded SWRA section	4
2.1.	Tensile test specimens parallel and perpendicular to wire direction. Excentric wires and thermal residual stresses lead to the in figure 2.1(a) shown curvature	8
2.2.	Ratio of mass-specific bending stiffness of SWRA and non-reinforced aluminum, bending around x-axis	9
2.3.	Stress–strain diagrams for SWRA with a wire content of 2% and for the non-reinforced aluminum matrix material	13
2.4.	Micrograph of SWRA in the vicinity of the reinforcing wire and simulated distribution of longitudinal residual stresses in the aluminum matrix (2% wire content)	16
2.5.	Effects of thermal residual stresses on the compressive failure behavior of SWRA	18
2.6.	Non-reinforced and reinforced tensile specimens and test results for tension in and perpendicular to wire direction as well as in and perpendicular to extrusion direction	22
3.1.	Interrelationship of yield function and strain hardening function . . .	28
3.2.	Isotropic yield loci according to the predictions of von Mises, Tresca and Hershey ($m = 8$) with a solution derived with a full constraint model of an isotropic fcc material, adapted from [12]	29
3.3.	Layered compression test and specimen geometry before and after testing	36
3.4.	Determination of the strain hardening curve by inverse FEM approach	39
3.5.	Extrapolation of experimental strain hardening data with analytical functions — unconstrained and constrained fitting approaches	40
3.6.	Strain rate and temperature dependent yield stress for mild steel En3B determined from shear tests [23]	42
3.7.	Experimental strain hardening of the steel wire and extrapolation with Voce’s strain hardening function [81]	45
3.8.	Results of dynamic strain hardening tests of aluminum alloys of group 6xxx	46
3.9.	Experimentally determined strain rate sensitivity of the high-strength austenitic steel 1.4310 (SS301)	47

3.10. Wire specimen with short gauge length for determination of strain rate dependency	48
3.11. Microstructure and chemical composition of the matrix-wire interface	49
3.12. Specimens for determination of axial shear strength and normal strength of the interface	50
4.1. Void growth and coalescence due to ligament necking and shear [120]	52
4.2. Experimental and simulated stress–strain curves with optimized Gurson material parameters [81], simulated specimens depict the gauge length	58
4.3. Experimental and simulated stress–strain curves for SWRA with tension in wire direction	60
4.4. Wire debonding and evolution of failure and fracture in SWRA at tension perpendicular to wire direction, the plots show the equivalent strain	62
4.5. Experimental and simulated stress–strain curves for SWRA with tension perpendicular to wire direction	63
4.6. Development of interface normal stress for tension in and perpendicular to wire direction	65
4.7. Sensitivity of SWRA with respect to the interface’s normal strength of the wire-matrix interface and to the wire’s fracture strain	67
5.1. Bolt-pull-out test and corresponding simulation model [81]	70
5.2. Experimental and simulated bolt-pull-out fracture modes for non-reinforced aluminum (a, b, c), SWRA in wire direction (d, e) and perpendicular to wire direction (f, g) [81]	72
5.3. Experimental and simulated force versus bolt–displacement curves [81]	73
5.4. Geometry and force–displacement curve of a triggered extruded section with square cross section	77
5.5. Circular crash tube made from SWRA after impact with 1350 J (photos courteously provided by M. Wedekind)	79
5.6. Square crash tube made from SWRA before and after quasistatic crushing	80
5.7. Experimental setup and test specimen for three-point bending test with an impact load; pre-damaged SWRA section with drilled holes .	82
5.8. Four characteristic stages of the three-point bending test with an impact load	83
5.9. Force–displacement curves for non-reinforced and reinforced specimens with drilled holes of 16 mm and 26 mm diameter	84
5.10. Twofold–symmetric simulation model of reinforced section with drilled holes under impact load and bending support	87
5.11. Experimental and simulated force–displacement curves for reinforced specimens with drilled holes of 16 mm and 26 mm diameter	88

5.12.	Twofold–symmetric simulation model of fully clamped reinforced hollow section under impact load and bending support	88
5.13.	Fracture of a fully clamped, wire reinforced section under dynamic impact crushing and bending support	90
6.1.	Flat reinforced section with a wire content of $\phi_w = 13.5\%$	91
6.2.	Cross section geometries of simulated sections with prospective improvements	92
6.3.	Experimental and simulated stress–strain curves with optimized Guron parameters for EN AW-6082	94
A.1.	Temperature-dependent CTE of the steel wire alloy 1.4310 — adapted from [79]	110
A.2.	Geometry of dynamic tensile test specimen	112
A.3.	Specimens for determination of GTN model parameters	112
A.4.	Derived strain hardening curves from tensile tests at the time of material characterization and from layered-compression tests 20 months after material characterization	113

List of Tables

2.1.	Determined Young’s moduli of tensile specimens in and perpendicular to wire direction with centric and excentric wires	8
2.2.	Determined elastic material properties (Young’s modulus E , Poisson’s ratio ν) and CTE (CTE averaged for the cooling interval of $20^{\circ}\text{C} \leq T \leq 260^{\circ}\text{C}$)	14
2.3.	Comparison of strain energy density until uniform elongation strain e_u and until fracture strain e_{fr} for steel-wire-reinforced and non-reinforced aluminum	21
3.1.	Analytical strain hardening functions for the approximation and extrapolation of experimental strain hardening data	34
3.2.	Determined orthotropic yield stresses and yield ratios of the extruded, non-reinforced aluminum matrix EN AW-6060T4, values in brackets are standard deviations	44
3.3.	Determined strain hardening parameters of the Hockett–Sherby function for the non-reinforced aluminum matrix EN AW-6060	44
3.4.	Parameters of Voce’s strain hardening function for the high-strength steel wires [81]	45
3.5.	Sensitivity of the steel wire’s UTS towards strain rate	47
4.1.	GTN material fracture parameters for the aluminum matrix for a characteristic finite element length of $l_c=0.5\text{ mm}$ (adapted from [81])	57
5.1.	Energy absorption of bending sections with drilled holes made from SWRA and non-reinforced aluminum	85
5.2.	Comparison of energy absorption of reinforced bending sections with drilled holes from experiment and simulation	86
6.1.	Identified strain hardening parameters of Voce’s function for EN AW-6082T6	94
6.2.	Energy absorption of fully clamped sections under impact bending load, SWRA with varying interface strength	95
6.3.	Energy absorption of fully clamped sections, SWRA with varying wire content	95
6.4.	Energy absorption of fully clamped sections under impact bending load, SWRA with increased matrix strength	95

A.1. Temperature-dependent CTE of aluminum alloy EN AW-6060 [94]	. . . 110
A.2. Tabulated data on temperature-dependent elasto-plastic material data of EN AW-6060 and austenitic stainless steel [8] 111

List of symbols

Roman symbols - lower case

a	acceleration
a, b, c, f, g, h	parameter in Barlat's yield function "Yld'91"
a, c, h, p	parameter in Barlat's yield function "Yld'89"
e	engineering strain
\tilde{e}	limit strain for integration
e_u	uniform elongation (engineering strain)
f	current void volume content
f^*	modified void growth function
f_C	critical void volume for void coalescence
f_F	void volume for fracture
g	gravity acceleration
k_ω	calibration constant in Nahshon–Hutchinson modification
l_0	initial length
l_c	characteristic element length
m	Hollomon's strain rate hardening parameter
m	yield function exponent
n	strain hardening exponent
p	strain hardening parameter in the Hockett–Sherby function
p	parameter in the Cowper–Symonds model
q_1, q_2, q_3	constitutive parameters of the GTN model
r_b	r-value for biaxial tension
$r_{w_{red}}$	reduced radius of the wire
r_w	radius of the wire
r_φ	r-value for tension at an angle φ to extrusion direction
s	engineering stress
s_N	standard deviation of mean strain for void nucleation
t	wall thickness
$w_{m_{red}}$	reduced width of the matrix
w_m	width of the matrix

Roman symbols - upper case

A	current cross section area
A_0	initial cross section area
A_{fr}	minimum cross section area after fracture
A_{ijkl}	anisotropy coefficients
A_{voids}	area of voids
A, B, C, F, G, H	Bishop–Hill abbreviations
C	parameter in the Cowper–Symonds model
D	damage parameter
E_{II}	Young’s modulus of SWRA in the elasto-plastic regime II
E_m, E_w	Young’s modulus of matrix and wire
E_N, E_T	normal stiffness and in-plane interface stiffness
$E_{ }, E_{\perp}$	Young’s modulus parallel and perpendicular to wire direction
F_{max}	maximum measured force
F, G, H, L, M, N	parameter in Hill’s yield criterion “Hill 1948”
G	dimensionless whole body acceleration
I	area moment of inertia
I_3	third invariant of the stress tensor
J_2	second invariant of the deviatoric stress tensor
K_1, K_2	parameters in Barlat’s yield function “Yld’89”
K	strain hardening coefficient
N	strain hardening parameter in the Hockett–Sherby function
R_e	elastic limit stress
R_m	ultimate tensile strength
R_{pc}	yield strength of the composite
R_{pm}	yield strength of the matrix
$R_{p0.01}, R_{p0.2}$	yield stress at a plastic strain of 0.01 and 0.2
S_1, S_2, S_3	eigenvalues of the deviatoric stress tensor
$S_{p, Al}, S_{p, SWRA}$	mass-specific bending stiffness of aluminum and SWRA section
T_i	impulse duration
T_M	melting temperature
T_{rec}	temperature of recrystallization
U	strain energy
U_0	strain energy density per unit volume

Greek symbols

$\alpha_{\text{th,m}}$	coefficient of thermal expansion of the matrix
$\alpha_{\text{th,w}}$	coefficient of thermal expansion of the wire
β	buckling factor
γ	distortion
δ	stretching factor
δ_1, δ_2	limits of constraint function
ΔT	temperature difference during cooling
ε_0	prestrain parameter
$\varepsilon_{\text{fail}}^{\text{P}}$	plastic strain level for onset of failure
$\varepsilon_{\text{fr}}^{\text{P}}$	plastic strain level for fracture
ε_{N}	mean strain for void nucleation
ε_{u}	ultimate true strain
$\dot{\varepsilon}$	strain rate
$\dot{\varepsilon}^{\text{qs}}$	strain rate under quasistatic conditions
λ	slenderness ratio
λ_{crit}	critical slenderness ratio for global buckling
$d\lambda$	plastic multiplier
$\mu_{\text{G}}, \mu_{\text{S}}$	friction coefficient for gliding and sticking
ν	Poisson's ratio
$\omega(\boldsymbol{\sigma})$	Lode-cosine function
$\phi(\sigma_{ij})$	yield function
ϕ_0	reference value for yield function
ϕ_{w}	wire volume content of the composite
Φ	yield condition

σ_b	yield strength at biaxial tension
σ_{eq}	equivalent stress (von Mises)
σ_{hyd}	hydrostatic stress
$\sigma_{n_{max}}$	interface normal strength
σ_s	saturation stress
σ_y	yield stress
τ	shear stress
τ_{max}	maximum axial interface shear strength
$\tau_{13_{max}}$	maximum shear stress in Tresca's yield criterion

Tensors and Vectors

γ_{ij}	shear components of engineering strain tensor
δ_{ij}	Kronecker's delta
e_{ii}	diagonal components of engineering strain tensor
\mathbf{E}	Green–Lagrange strain tensor
E_{ij}	components of the Green–Lagrange strain tensor
\mathbf{E}^{lin}	linearized Green–Lagrange strain tensor
E_{ij}^{lin}	components of the linearized Green–Lagrange strain tensor
$\boldsymbol{\varepsilon}$	strain tensor
$\boldsymbol{\varepsilon}^{log}$	logarithmic strain tensor (Hencky-strain tensor)
\mathbf{F}	displacement gradient
\mathbf{I}	identity matrix
$[\mathbf{s}]$	deviatoric stress tensor
$\boldsymbol{\sigma}$	stress tensor
$\sigma_{ij}^{(2PK)}$	components of 2 nd Piola–Kirchhoff stress tensor
\mathbf{u}	displacement vector
\tilde{u}_i	continuous displacement field
\mathbf{x}	point coordinates in undeformed state
\mathbf{X}	point coordinates in deformed state

Abbreviations

bcc	body-centered cubic
fcc	face-centered cubic
CP	complex-phase
CTE	coefficient of thermal expansion
DFG	German Research Foundation
DP	dual-phase
FEM	finite element method
FRP	fibre-reinforced-plastics
GLARE	glass laminate aluminium reinforced epoxy
GTN	Gurson–Tvergaard–Needleman
KIT	Karlsruhe Institute of Technology
MMC	metal-matrix-composite
LED	light-emitting diode
MMC	metal matrix composite
SWRA	steel-wire-reinforced Aluminum
TR10	collaborative research center Transregio 10
TRIP	transformation-induced plasticity
TWIP	twinning-induced plasticity
UTS	ultimate tensile strength

1. Introduction

High-performance composite materials such as carbon-fiber-reinforced plastics have found their way from a vast utilization in the aerospace sector (Airbus A350, Boeing 787) into the consumer market (bicycles, rackets) and eventually the automotive sector (BMW i3). The combination of strong and stiff carbon fibers with a ductile and lightweight polymer matrix leads to a hybrid material with superior mass-specific stiffness and strength. This serves as a good example for a hybrid material which combines strengths and eliminates weaknesses of its constituents such as almost no compressive resistance of the fibers and low strength and stiffness of the polymer matrix.

Using a metal matrix instead of a polymer matrix results in a metal matrix composite (MMC) with much less commonly known applications [73]. One example is glass laminate aluminum reinforced epoxy (GLARE) for airplane fuselages which is mainly used for its good impact resistance. Some advantages of a metal matrix over a polymer matrix aside from a better impact tolerance are also a low susceptibility to moisture and a possible use at higher operating temperatures. In the automotive sector, a common use of MMC are aluminum pistons and cylinder liners which are reinforced with silicon carbide particles and carbon fibers in order to increase the wear resistance [70].

Within the collaborative research center Transregio 10 (TR10), which is funded by the German Research Foundation (DFG), an aluminum matrix reinforced with high-strength steel wires is discussed for applications in the automotive and aviation sector. The material was shown to possess increased stiffness and ultimate tensile strength (UTS¹) [124] as well as better fatigue life [43, 77] compared to the non-reinforced aluminum alloy. Being produced in a composite extrusion process, lightweight extruded car frames for small batch series or stringers for aircraft fuselages [43] or train coaches are possible applications for this MMC.

Considering extruded and reinforced aluminum sections as load-bearing, structural elements for the transportation sector, their behavior at crash events must be known and, therefore, will be investigated in this thesis.

1.1. Motivation

Over the last decades, the safety of vehicles has been drastically improved via a multitude of protection systems which assist the driver at driving safely and actively

¹UTS: the UTS is the highest measured force during a tensile test divided by the initial cross section area of the tensile specimen

help avoiding accidents. Despite the fact that the percentage of fatal accidents is continuously decreasing [113], a total prevention probably will never be reached. Therefore, measures of passive safety need to be further improved, which protect the vehicle's occupants. They can be summarized as [17]:

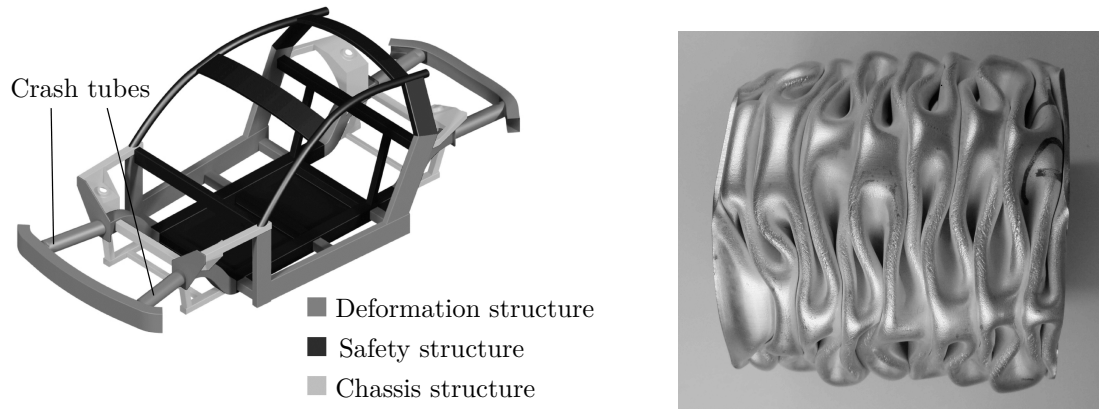
- seatbelts
- airbags
- safety cell (occupant cell)
- energy absorption in "crumple zones"

During a crash, the safety cell has to withstand the occurring loads, while the deformable zones have to dissipate the kinetic energy of the crash. In the car's front-end, special absorbing structures crumple at designed force levels and convert the kinetic energy into deformation energy. Deformation zones in an aluminum frame structure of a lightweight electrical vehicle are shown in figure 1.1(a) with special crash tubes in the front- and rear-end. A circular crash tube after deformation can be seen in figure 1.1(b).

As the energy dissipates mainly by plastic deformation, a high energy absorption can be reached with materials having a high strength and a high ductility (i.e. high ability of deformation prior to fracture). However, for most conventional metallic alloys strength and ductility are opposing properties, meaning that an increase in strength leads to a decrease in ductility. Improvements can be reached by using new materials like advanced steels, fiber-reinforced-plastics and other, hybrid materials. Advanced steels are for instance transformation-induced plasticity (TRIP) and twinning-induced plasticity steels (TWIP), which offer high strength and high ductility, as well as complex-phase (CP) and dual-phase (DP) steels, which combine a high UTS with a low yield strength and good formability. Fiber-reinforced-plastics in contrast, rely on a high strength and brittle fracture processes for energy absorption.

During the design of energy absorbing structures, aside from a structural-mechanically sound concept, further aspects of lightweight design have to be considered like manufacturability, cost-effectiveness, electro-chemical and thermo-mechanical compatibility and ecological footprint. One promising hybrid material for crash energy absorption is steel-wire-reinforced aluminum (SWRA), since it offers an increased UTS in comparison to non-reinforced aluminum, while at the same time preserving good ductility. Many further properties amount to the energy absorption of a material, e.g. strain-rate sensitivity, material failure and fracture and overall elasto-plastic behavior. This research, therefore, characterizes SWRA and analyzes structure-related specimens made of non-reinforced and steel-wire-reinforced extruded aluminum sections with respect to fracture behavior and response to dynamic impact loading. With experimental studies and numerical simulations, the crash-worthiness is assessed and recommendations for a further development of SWRA are given.

The composite extrusion process for the production of SWRA was investigated



(a) Deformation structures in the Lightweight Extruded Aluminum Frame (“LEAF”) with front and rear circular crash tubes [122] (b) Circular crashtube after axial crushing

Figure 1.1.: Lightweight extruded aluminum car frame with circular crash tubes and progressive buckling of the crash tube

in the collaborative research center Transregio 10, which constitutes the scientific framework of this research.

1.2. Scientific framework - the collaborative research center Transregio 10

The collaborative research center Transregio 10 investigates the integration of forming, cutting and joining for the flexible production of lightweight frame structures. Aspects of design, construction and production with extruded sections are treated by nearly 20 subprojects with researchers from three cooperating universities: Karlsruhe Institute of Technology, TU Dortmund University and Technische Universität München. Two main targets are the automation and the flexibilization of the fabrication of lightweight frame structures, used for instance in aircraft fuselages or in car body structures. Forming of the extruded sections, cutting into defined length and joining are conventionally separate manufacturing operations which make the production of lightweight frame structures inefficient for mass production. Within TR10, an integration of these manufacturing steps into one manufacturing chain was reached, allowing for a time and cost-efficient production of extruded sections.

A further novelty is a three-dimensional bending of the extruded sections into final shape, which is performed directly after extrusion, with the sections still in a hot state. This reduces the stresses during bending tremendously compared to a conventional cold bending process. Consequently, manufacturing forces and shape distortion reduces. The sections can subsequently be cut into defined length, positioned and joined, as well as quality controlled in one line of manufacture [20]. This leads to a high flexibility of the production line in terms of varying lot sizes, product

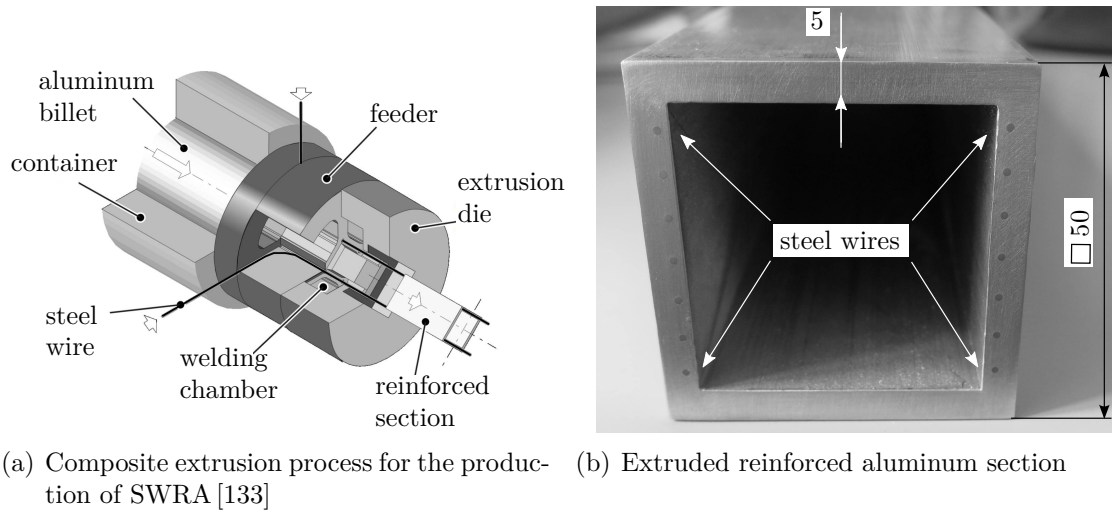


Figure 1.2.: Composite extrusion process and extruded SWRA section

variety and rapid manufacturability. Further aspects of flexibilization are an in-line variation of wall thicknesses of the extruded sections during extrusion and the introduction of functionalizing or reinforcing elements into aluminum or magnesium matrices. The hybridization is performed during extrusion with no further joining steps necessary, which is beneficial in regard to short production cycles. This is accomplished using a composite extrusion process shown in figure 1.2(a), which feeds the modifying elements to the matrix in the extrusion die.

Varying the content of reinforcement, the mechanical properties of the extruded section can be adjusted and intelligent designs of the extrusion die allow for selective reinforcements. The composite extrusion process of TR10 leads to heterogeneously, but continuously wire-reinforced metal matrices as shown in figure 1.2(b). Aside from reinforcing elements, functionalizing elements like insulated cables as electrical conductors or fiber-optic sensors for structural health monitoring may be embedded into extruded sections. Insulated cables were already successfully inserted and used for the electrical supply of LEDs [59].

As reinforcing elements, high-strength metallic wires and cables, ceramic wires and carbon-fibers were successfully integrated and the resulting hybrid materials were analyzed. The combination of high-strength austenitic steel wires (material number 1.4310 (SS301)) with a ductile aluminum matrix (EN AW-6060T4) was found as a promising combination with respect to mechanical properties and cost-effectiveness [124]. The resulting hybrid material is the herein analyzed SWRA.

1.3. Outline of the thesis

During the course of TR10, a multitude of investigations on the material and structural behavior of SWRA were successfully carried out. Chapter 2 sums up the state

of knowledge of SWRA with a focus on those findings, which are vital for the understanding of the further conducted research with respect to the structural response during dynamic impacts, high strains and fracture.

With respect to this special load case of dynamic impact, chapter 3 provides the theoretical framework for the mathematical description of material plasticity including strain rate sensitivity. The parameters of the plastic material models for SWRA are further determined experimentally. As material failure and fracture processes dominate the structural behavior of many structures during crash events, special emphasis is placed on a physically meaningful description of the material's failure and fracture in chapter 4. This is done by subdividing the fracture behavior of SWRA into failure initialization and final fracture of its constituents. For the aluminum matrix, a shear-modified Gurson fracture model is discussed and parametrized. A failure model of the cohesive interface is based on interface normal stresses; the fracture of the steel wire is modeled with a strain based fracture criterion including a description of material softening. The validity of this modeling approach is checked based on experimental testing with tensile specimens. Moreover, parameter studies clarify the effect of a theoretically increased interface strength and increased fracture strains of the wire in order to identify future potential of SWRA.

In chapter 5, the material model is subsequently validated with the help of bolt-pull-out tests which offer a complex load case with several fracture modes. A good agreement with simulated data in terms of force–displacement curves and predicted fracture modes proves the validity of the material model and the simulation technique. The bolt-pull-out tests also help to identify weaknesses and strengths of SWRA for pin–joint connections in terms of reinforcing and crack arresting effects of the steel wires. Further studies concern the capability of energy absorption of SWRA during crash events. Two representative crash-energy absorbing structures are considered: an axial crash tube as it is found in the front-end of cars or in train bumpers, and a reinforced hollow section representing a simplified B-pillar under a bending impact load. For the latter example, drop tower tests provide experimental data at high strain rates and, as for all herein conducted experiments, samples of non-reinforced aluminum serve as reference for comparison.

Chapter 6 gives a prediction of further attainable performance of SWRA by means of numerical simulation. Therefore, three possible improvements for a future SWRA are assessed. Firstly, effects of a higher interface strength, secondly, a higher wire volume content and lastly the use of an aluminum matrix with higher strength (EN AW-6082T6) are evaluated.

A conclusion on the findings is drawn in chapter 7.

2. Basic elasto-plastic properties of steel-wire-reinforced aluminum (SWRA)

This research benefits from numerous previous investigations on the topic of heterogeneously reinforced aluminum extrusions. A summary and discussion of previous findings on the material properties of SWRA is given in the following and is complemented with additional own analyses. The topics of basic material properties as stiffness, strength, ductility and fracture behavior are covered, as well as influences of the extrusion process on the mechanical properties of extruded sections. The state of knowledge is discussed, mainly with respect to aspects of crashworthiness of SWRA.

2.1. Structural stiffness

Young's modulus of an unidirectionally wire reinforced (MMC) in wire direction is calculated by rule of mixture [58],

$$E_{\parallel} = E_w \cdot \phi_w + E_m \cdot (1 - \phi_w), \quad (2.1)$$

with the wire volume content ϕ_w and the Young's moduli E_c , E_w and E_m of the composite, the wire and the matrix, respectively.

Hill [47] showed, that equation (2.1) gives a lower boundary for the composite's Young's modulus, as differing Poisson's ratios of wire and matrix lead to a higher stiffness. In addition, a perfect interface between wire and matrix is a premise, guaranteeing equality of strains in wire and matrix. It can be deduced from equation (2.1) that for reaching a stiffening effect, the reinforcing wires must have a higher Young's modulus than the matrix itself.

Merzkirch [77], reports a good agreement between experimentally determined and calculated Young's modulus for the aluminum alloy EN AW-6082 with steel wires of 1.4310 at various wire volume fractions ranging from 1 to 25 %. Weidenmann [124] also confirmed the rule of mixture for the aluminum alloy EN AW-6060 with embedded steel wires of 1.4310 and a wire volume content of 11 %. Wedekind [121], however, encountered a disagreement in theoretical and experimental modulus of

more than 20 % for specimens with a low wire volume content of 2 %, which was attributed to thermal residual stresses in the specimens. Wedekind [121] further tested specimens with a higher reinforcement content which were in good agreement with the theoretical prediction. The higher reinforcement content was reached — similar as in [77, 124] — by reducing the thickness of the matrix by milling or turning. Wedekind [121] argues that the stresses on the composite, which are introduced by the machining process, may have reduced or released the thermal residual stresses. The issue of thermal residual stresses caused by the extrusion process, is addressed in section 2.3. Their effect on the structural properties of SWRA sections is firstly not considered in order to gain a more fundamental understanding of the composite.

As SWRA is an unidirectionally reinforced MMC, its stiffnesses are orthotropic, which needs to be taken into account for construction tasks. Especially at intersections of extruded sections, stress states are multiaxial and the material's Young's modulus perpendicular to the wire direction E_{\perp} must be known in order to predict and assess the response of the structure. This is done with the inverse rule of mixture [73] with the assumptions of an elastic and isotropic behavior of matrix and wire, as well as a rigid connection between them. Further, the wire must be embedded centric with respect to the thickness of the matrix,

$$E_{\perp} = \frac{1}{\frac{\phi_w}{E_w} + \frac{1-\phi_w}{E_m}}. \quad (2.2)$$

During the process of composite extrusion, the wires are positioned by the material flow of the matrix. It can occur that the wires are shifted and not positioned centrically. The arising thermal residual stresses then lead to a bending of the tensile test specimens as shown in figure 2.1. In consequence, a uniaxial tensile test can no longer be performed as an additional bending load is introduced. Therefore, the measured Young's moduli tend to be lower than the actual ones. Tensile test data in table 2.1 of the specimens in figure 2.1 shows, how an excentricity of the wire position affects the measured Young's moduli. The curved specimens were cut by waterjet cutting from the in figure 1.2(b) shown reinforced section. This was done to exclude any influence on the specimens due to a heating during cutting. A measurement of the curved specimens was done by Stöckl [106]. Test data of non-curved specimens of SWRA with centric wires were taken from Wedekind [121] and complemented with additional measurements. It can be concluded, that a stiffening effect of a steel wire reinforcement is given and can be calculated by the rules of mixture. This was confirmed for higher contents of reinforcement and other aluminum matrices by [77, 121, 124]. During experimental determination of Young's modulus care has to be taken not to use specimens with excentric wires which lead to a distortion of the specimen.

From a structural point of view, the stiffness of a structure is not only determined by its material's Young's modulus, the geometric stiffness often plays a major role. Designing a lightweight structure at a given stiffness with no further restrictions,



(a) Tensile test specimen with wires parallel to tension direction and a visible distortion



(b) Cross section of the tensile specimen in a)



(c) Tensile specimen with wires perpendicular to tension direction

Figure 2.1.: Tensile test specimens parallel and perpendicular to wire direction. Excentric wires and thermal residual stresses lead to the in figure 2.1(a) shown curvature

Table 2.1.: Determined Young's moduli of tensile specimens in and perpendicular to wire direction with centric and excentric wires

Property	E_{\parallel} according to equation (2.1)	E_{\parallel} , centric wires, test data	E_{\parallel} , excentric wires, test data	E_{\perp} according to equation (2.2)	E_{\perp} , centric wires, test data	E_{\perp} , excentric wires, test data
Young's modulus E in MPa	72800	73669	36005	70946	74538	39295
Standard deviation in MPa	-	2161	6723	-	7287	8433

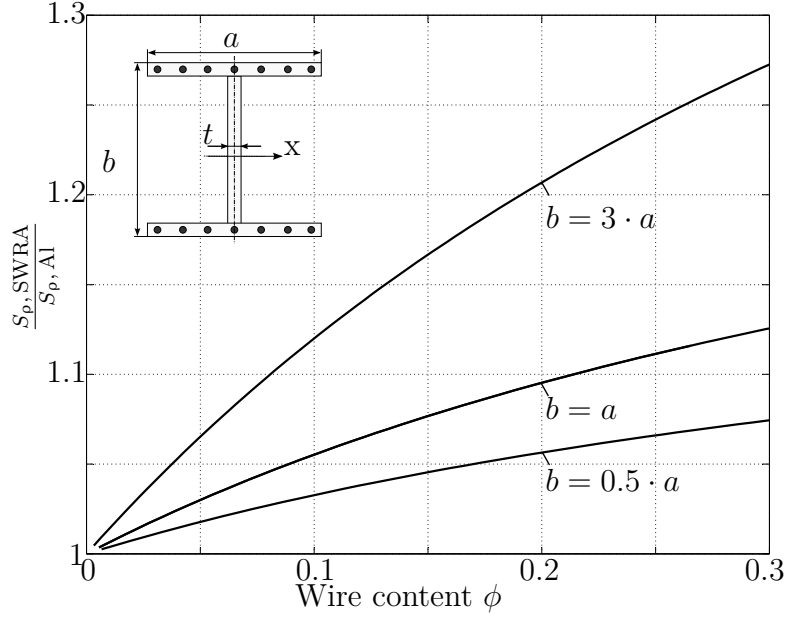


Figure 2.2.: Ratio of mass-specific bending stiffness of SWRA and non-reinforced aluminum, bending around x-axis

different densities of the materials must be taken into account. For the design task of a bar under axial loading, whose weight should be minimized at a given stiffness, the material with the highest mass-specific stiffness E/ρ is favorable [6]. The mass-specific stiffness, however, remains nearly unchanged by reinforcing an aluminum alloy with steel wires, due to similar mass-specific stiffnesses of aluminum matrix and steel wire [77, 124].

This is different for a pure bending loading, where the higher modulus of the wire is amplified by Steiner's moment of inertia, which overcompensates the higher density of the wire. Therefore, an increase in the mass-specific bending stiffness can be reached. The calculated increase is given for the example of a reinforced double-T beam and varying reinforcement content. The deriving equations for figure 2.2 are given in appendix A.1. Figure 2.2 shows the ratio of mass-specific bending stiffness of SWRA $S_{\rho, SWRA}$ to non-reinforced aluminum $S_{\rho, Al}$ depending on the wire content. The mass-specific bending stiffness of the section here is defined as

$$S_{\rho} = \frac{E \cdot I}{\rho} \Big|_{\text{section}} \quad (2.3)$$

Since the increase in bending stiffness mostly results from Steiner's moment of inertia times the higher Young's modulus of the wires, lanky sections profit more of a steel-wire reinforcement than stubby sections.

2.2. Structural strength

Most mechanical structures are designed to resist the loading in a way that the arising strains stay in the elastic regime. If the material leaves the elastic regime and plastifies, a premise of the structural layout is no longer valid and the structural behavior is unknown. Plastification is critical for structural integrity, as it goes along with a drastic decrease in the material's stiffness. The stress at which the material switches from an elastic behavior to a plastic behavior is called elastic limit or yield strength R_e .

Most aluminum alloys do not show an abrupt change from elastic to plastic behavior as it is known for example from carbon-rich steel alloys (cf. Cottrell atmosphere). It is rather a smooth transition from the elastic to the plastic state. This can be explained by different orientations of the aluminum grains to the acting force, with the favorably oriented grains first turning into plastic state (cf. Schmid's law). Therefore, it is necessary to introduce a technical yield strength, which gives the stress at a given plastic strain. Commonly, the plastic strain is chosen as 0.01% or 0.2% with the corresponding yield strengths $R_{p0.01}$ and $R_{p0.2}$, respectively. R_m is the maximum engineering stress during an uniaxial tensile test. For most structural design tasks, it is of less importance than the yield strength, since a plastification is not admissible. It may, however, serve as an indicator for the material's hardening capability.

A representative stress-strain curve for SWRA with a wire content of 2% and the discussed stress limits are shown in figure 2.3(a) and compared to the stress-strain curve of the non-reinforced matrix material. Both specimens were cut from the extruded section shown in figure 1.2(b). This guarantees equal extrusion and cooling conditions, allowing for a meaningful comparison.

In figure 2.3(a) four regions are marked which are typical for SWRA and generally for unidirectionally reinforced ductile metal matrices. The following regions were described by Kelly [58]:

- I elastic deformation of matrix and wire
- II plastic deformation of the matrix, still elastic deformation of the wire
- III plastic deformation of matrix and wire
- IV material failure and fracture.

Disregarding residual stresses, the yield strength of SWRA can be predicted knowing the material properties of steel wire and aluminum matrix. Therefore, the theoretical model of Kelly [58] can be used for the elastic limit [121] and also predicts R_m well [124]. Since the matrix plastifies first, the composite's uniaxial yield strengths $R_{p0.01}$ and $R_{p0.2}$ are determined by the stresses in the matrix by

$$R_{pc} = \frac{E_w \cdot \phi_w + E_m \cdot (1 - \phi_w)}{E_m} \cdot R_{pm}, \quad (2.4)$$

with R_{pc} being the yield strength of the composite and R_{pm} being the yield strength of the matrix.

As the steel wire is more brittle than the aluminum matrix, it reaches its UTS at a lower strain than the matrix. Assuming that at the point that the wires reach their UTS, the softening of the composite due to necking of the wires is higher than the persisting strain hardening of the aluminum matrix, R_m of the composite can be calculated as [58]

$$R_{mc} = \phi_w \cdot R_{mw} + (1 - \phi_w) \cdot \sigma_{m'}, \quad (2.5)$$

with the composite's UTS R_{mc} , the wire's UTS R_{mw} and the current stress in the matrix when the wires reach their UTS $\sigma_{m'}$.

Comparing the overall stress–strain curves of non-reinforced and reinforced aluminum in figure 2.2, the most striking change caused by a steel wire reinforcement of only 2 % is a significant increase in R_m , which rises by about 30 % [81]. Overall low yield strengths for the aluminum alloy are due to a missing heat treatment. After extrusion, the sections were neither specially cooled nor heat treated (condition "T4" [31]). A subsequent stretch-forming and precipitation heat treatment increases the overall strength of the composite as shown by Hammers [43] for similar material systems.

In contrast to a rising R_m , the elastic limit has decreased as can be seen in figures 2.3(a) and 2.3(b). Contradictory results are reported for the yield strength $R_{p0.2}$. Weidenmann [124] performed tensile tests at a higher reinforcement content of 11 % and confirms an increase in $R_{p0.2}$. Merzkirch [77] reports elastic limits for a similar material system of a matrix of EN AW-6082 and wires of 1.4310 with a reinforcement content ranging from 3.3 % to 25 %. Up to a reinforcement content of 16 %, the elastic limit is decreasing, and increasing from 16 % on, which cannot be explained by the model of Kelly [58]. This material behavior is explained by the aforementioned thermal residual stresses [82] as further clarified in section 2.3. The by equation (2.5) calculated R_m was for every reinforcement content in good agreement with Kelly's equation, showing a steady increase in UTS with increasing reinforcement content [77].

For structural design tasks, it has to be considered that with a decreasing elastic limit up to a wire content of 16 %, the elastic regime of SWRA is also shortened [77]. At stresses higher the elastic limit, the matrix plastifies and for further loading resists with a greatly reduced tangent modulus. A lower boundary for the tangent modulus in regime II is given by Young's modulus of the reinforcing wires, assuming ideal-plastic behavior of the aluminum matrix,

$$E_{II} \geq \phi_w \cdot E_w. \quad (2.6)$$

Whereas for most technically used alloys, the ratio of yield strength to elastic limit $R_{p0.2}/R_e$ is close to unity, the ratio for SWRA is increasing with increasing wire content. Normally taking $R_{p0.2}$ as limit stress and applying a safety margin, it can be assured that the structure does not leave the elastic regime. Taking $R_{p0.2}$ as limit stress for SWRA, one has to bear in mind that even with high safety margins a plastification of the structure is likely. Therefore, it has to be individually assessed whether this plastification can be tolerated.

For off-axis loads acting on SWRA, it is known from uniaxially reinforced materials, that strength and stiffness towards the acting load decrease with increasing angle α between acting load and direction of reinforcement. SWRA, therefore, performs best for uniaxial loads in wire direction. However, multiaxial loading cannot fully be avoided for any load case so that a failure criterion for structural strength analysis is necessary. Wedekind introduced a mode-based failure criterion for SWRA which takes three reasons for plastic behavior into account [82, 121], namely

- Mode I: Plastification of the matrix
- Mode II: Plastification of the wire
- Mode III: Debonding of the wire.

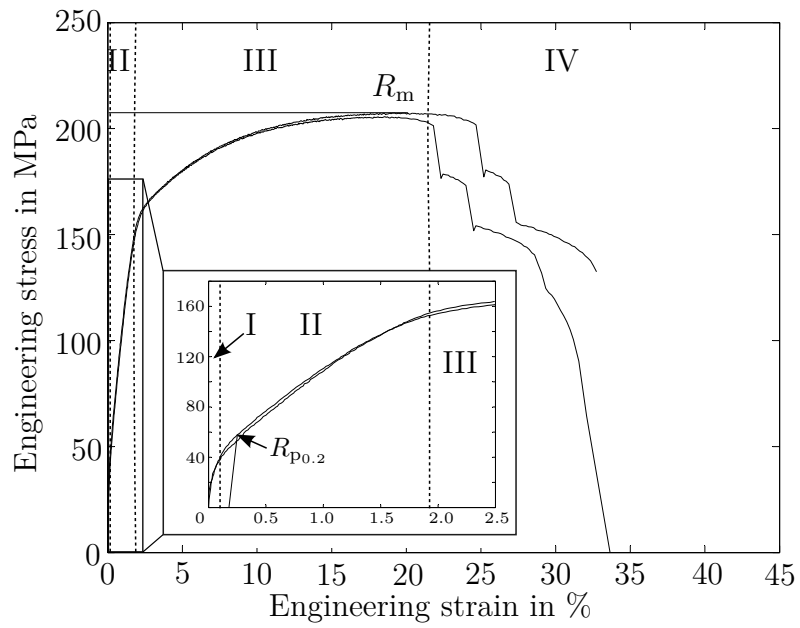
For SWRA with high elastic limits of the steel wire, failure mode II as one mode of initial plastification is not observed. Mode I is dominant for loads in wire direction, while for loads not acting in wire direction, mode I and mode III initiate plastic behavior. For further information on the failure criterion, please refer to [121].

2.3. Influence of the extrusion process on the mechanical properties

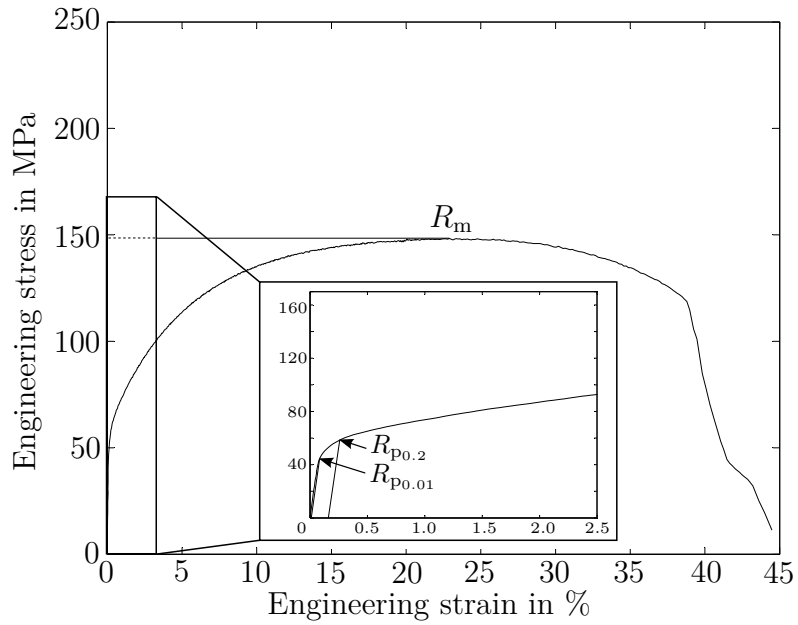
During the composite extrusion process, aluminum matrix and steel wires are joined at high temperatures and at a high degree of deformation of the aluminum matrix. A subsequent cooling or quenching of the extruded sections and a defined heat treatment further alter the material properties, mainly of the aluminum alloy. The heat treatment of extruded sections for aluminum alloy EN AW-6056 and aluminum alloy EN AW-2099 with Nanoflex-wires and its influence on the material properties is discussed in detail in [43]. This section concentrates on non-heat-treated sections in favor of focusing on the issue of thermal residual stresses.

2.3.1. Influence of the extrusion process on the material's microstructure and strength

Schomäcker [102] investigated on the process temperatures measuring the temperature of the extruded section using video thermography. Directly after the extrusion



(a) Stress-strain diagram for SWRA at a wire content of 2%, data from [81]



(b) Stress-strain diagram for the non-reinforced matrix material, data from [106]

Figure 2.3.: Stress-strain diagrams for SWRA with a wire content of 2% and for the non-reinforced aluminum matrix material

Table 2.2.: Determined elastic material properties (Young’s modulus E , Poisson’s ratio ν) and CTE (CTE averaged for the cooling interval of $20^\circ\text{C} \leq T \leq 260^\circ\text{C}$)

Property	E in MPa	ν	CTE in 10^{-6} K
Steel wire	197000	0.30	14.5
Aluminum matrix	66538	0.34	24.5

die, the temperatures vary from approximately 400°C up to 550°C , increasing with the extruded length of the section. As the temperatures are higher than the recrystallization temperature of aluminum, the aluminum matrix dynamically and statically recrystallizes during the process [57]. Due to different deformation grades and cooling rates in the vicinity of the steel wire, the recrystallization leads to a locally finer grain in the matrix (see figure 2.4(a)). This adds to an increase in the matrix’s strength compared to the non-reinforced aluminum alloy [81]. By testing the steel wires prior and after a heat treatment similar to the extrusion conditions, Weidenmann [124] found that the extrusion process does not decrease the wire’s strength. Therefore, it is reasonable to assume that the steel wires have approximately the same properties before and after embedding.

2.3.2. Thermal residual stresses

As the steel wire and the aluminum matrix possess different coefficients of thermal expansion (CTE), the cooling leads to thermal residual stresses in matrix and wire. In order to predict their magnitude, the CTE of aluminum alloy EN AW-6060 and steel wire 1.4310 are calculated as mean values for the cooling interval during composite extrusion. Data on the temperature dependent CTE of aluminum is given by [94], data on the steel alloy 1.4310 stems from [79]. The elastic properties are further extracted from measurements of [77, 132] and summarized in table 2.2. Assuming a fully elastic, temperature-independent behavior and equal Poisson’s ratios of wire and matrix, the thermal residual stresses can be calculated with a model of two rigidly joined trusses [121].

According to this model, the stresses in the matrix are tensile stresses, the stresses in the wire are compression stresses with the magnitude

$$\sigma_{\text{th,m}} = + \frac{\phi_w \cdot E_w \cdot E_m}{\phi_w \cdot E_w + (1 - \phi_w) \cdot E_m} \cdot (\alpha_{\text{th,w}} - \alpha_{\text{th,m}}) \cdot \Delta T \quad (2.7)$$

$$\sigma_{\text{th,w}} = - \frac{(1 - \phi_w) \cdot E_w \cdot E_m}{\phi_w \cdot E_w + (1 - \phi_w) \cdot E_m} \cdot (\alpha_{\text{th,w}} - \alpha_{\text{th,m}}) \cdot \Delta T \quad (2.8)$$

with $\alpha_{\text{th,w}}$ being the CTE of the wires, $\alpha_{\text{th,m}}$ being the CTE of the matrix and ΔT being the temperature difference during cooling.

As soon as the thermally induced stresses exceed the elastic limit of either wire or matrix, this model is no longer valid. For a material combination with the thermoelastic properties in table 2.2 and a cooling temperature of $\Delta T = 500 \text{ K}$, this is the case for a wire content of $\phi_w \approx 10 \%$. A further simplifying assumption of this model is a homogeneous stress distribution in wire and matrix.

While the stress distribution in the wire is rather homogeneous due to its slender geometry, the distribution in the matrix is inhomogeneous. Wedekind [121], Morasch [82] and Weidenmann [124] simulated the cooling process determining local stress concentrations around the wire with a partial plastification of the matrix. The simulations assumed a temperature interval for cooling which starts with the processing temperature of $T \geq 450^\circ\text{C}$ and ends at room temperature. The processing temperature, however, lies above the temperature of recrystallization T_{rec} of the aluminum matrix and, thus, was chosen too high for a cooling simulation.

During recrystallization, the grains in the aluminum matrix are newly formed, and a distortion due to thermal stresses is released [22]. Therefore, it is reasonable to estimate an effective cooling temperature with the magnitude of the temperature of recrystallization. As a rule of thumb, the temperature of recrystallization for pure metals is

$$T_{\text{rec}} \approx 0.4 \cdot T_{\text{M}} \quad (2.9)$$

where T_{M} is the melting temperature in Kelvin.

However, the temperature of recrystallization for technical alloys varies with the alloying elements. It varies further with the initial plastic deformation and with the heating rate. This makes it very difficult to estimate a recrystallization temperature for the extrusion process of SWRA. Since the residual stresses cause a reduction of the elastic limit, coupled thermo-mechanical finite element simulations of tensile specimens with residual stresses were made and the effective cooling temperature was assessed as $T_{\text{rec}} \approx 260^\circ\text{C}$.

The resulting longitudinal stresses (in wire direction) in the matrix at a wire content of 2% are shown in figure 2.4(b), taking temperature dependent Young's moduli, plastification and CTE of matrix and wire into account. The data on temperature dependent material properties of matrix and wire is summarized in appendix A.2.

As can be seen from figure 2.4(b), the stress distribution in the matrix is non-uniform with mainly tensile longitudinal stresses in the matrix, as predicted by equation (2.7). Yet, compressive stresses are found at the wire-matrix interface. The compressive stresses were also experimentally determined by [124]. The stress magnitudes are restricted to the elastic range of the matrix, so that no plastification occurs. For higher wire volume contents, the longitudinal stresses exceed the elastic limit of the matrix, so that a partial plastification occurs. This leads to a reduced

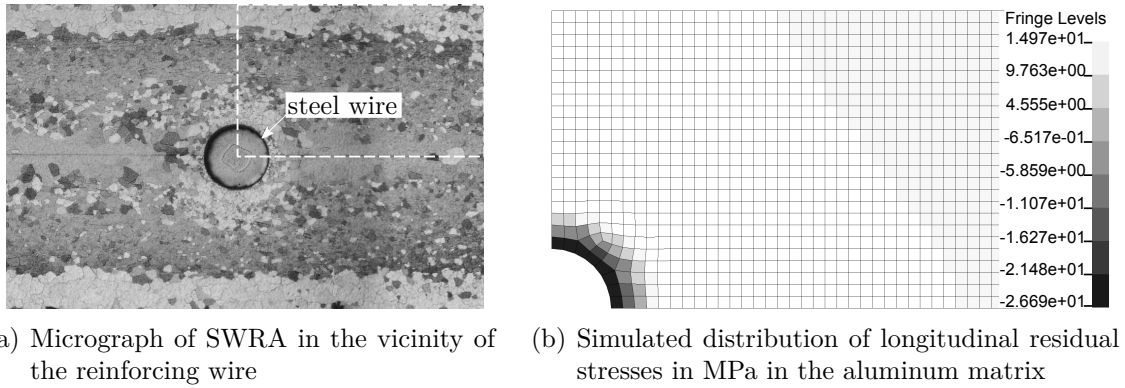


Figure 2.4.: Micrograph of SWRA in the vicinity of the reinforcing wire and simulated distribution of longitudinal residual stresses in the aluminum matrix (2% wire content)

Young's modulus, as the plastified regions of the matrix resist with a low plastic modulus to further longitudinal straining. The simulation predicts this effect for the given material combination for wire contents of $\phi_w \geq 13\%$.

An experimental determination of the stress state in the matrix had been determined by neutron scattering experiments [124, 133], however, the stress magnitudes are uncertain due to a non-uniform grain size [133]. The strain state in the reinforcing wire at a wire content of 2% was measured with neutron scattering experiments and simulated by FEM [100, 133]. The measurements showed a longitudinal stress component between -1175 MPa and -1100 MPa, whereas the FEM-results gave a longitudinal component of only -420 MPa. A possible explanation for this big difference is given by the microstructure of the steel-wire, which consists mainly of the two phases austenite and martensite, which may give misleading measurement results. The simulation does not consider the microstructure of the wire and gives averaged results, whereas the measurement gives different values, which depend on the phase that was measured. Based on the longitudinal stresses in the wire and an equilibrium of forces, an average longitudinal tensile stress in the aluminum matrix lies between 8.42 MPa and 23.5 MPa. These values agree well with the simulation results in figure 2.4(b) and reductions in the elastic limit of the composite reported by [82, 132].

2.3.3. Effects of thermal residual stresses on structures of steel-wire-reinforced aluminum

As the elastic limit of SWRA in pure tension is defined by the elastic limit of the aluminum matrix, the dominating tensile prestress in the matrix lowers the composite's elastic limit in tension. This was experimentally observed by [77, 82, 121] for a wire volume content of 2%. A higher wire content lowers the composite's yield

stress and, therefore, shortens the elastic region I [77] (see figure 2.3(a)) and it may even vanish completely for high wire volume contents [43].

Merzkirch [77] reports tensile test data with wire contents up to 25 % and a constant increase in the elastic limit from a wire content of 11 % on. This is contradictory to the thermal residual stresses in the aluminum matrix which increase with the wire content. A possible explanation can be found in the production process of the specimens used by Merzkirch [77]. An increased wire content was reached by extruding sections with a wire content of 2 %. Subsequently, the matrix was milled down in order to get specimens with a higher wire content. However, the mechanical treatment is likely to influence the stress state in the specimen. Moreover, the residual stresses depend on the wire content during cooling (equations (2.7), (2.8)), so that the stress state in milled down specimens is not fully comparable to the stress state which arises in a transient cooling of a specimen with higher wire content.

In case of compression in wire direction, the elastic limit is increased [75], so that SWRA shows a strength–differential effect. An increased Young’s modulus of SWRA compared to the non-reinforced matrix, for tensile loads, thus, can only be used until the stresses reach the reduced elastic limit σ_{yc} . For compressive axial loads, in contrast, the elastic region I is extended. This behavior is particularly interesting for axially compressed struts and trusses. The increased stiffness adds to the buckling resistance and the in compression extended yield limit postpones the onset of plastification.

The critical buckling stress is given by

$$\sigma_{\text{crit}} = \frac{\pi^2 \cdot E}{\lambda^2}, \quad (2.10)$$

with the slenderness ratio λ ,

$$\lambda = \beta \cdot l \cdot \sqrt{\frac{A}{I}}. \quad (2.11)$$

β here is a parameter for the considered Euler buckling case, l is the length of the truss, A is its cross section and I is its relevant area moment of inertia.

Using the elastic material data given in table 2.2, a reinforcement of 2 % leads to an increase in Young’s modulus and, therefore, an increase in critical buckling force of approximately 4 %, when comparing to a truss of non-reinforced aluminum. For a compact, axially compressed truss, failure due to plastification sets in before the critical buckling load is reached. For the wire content of 2 %, the yield limit in compression σ_{yc} is increased from 60 MPa for the non-reinforced matrix to 80 MPa for SWRA. This equals an increase of about 30 %.

A summarizing scheme of the effects of thermal residual stresses on SWRA is given in figure 2.5(a). A graph of the critical compression stress depending on the slenderness ratio is given in figure 2.5(b) and shows the benefits of a steel wire rein-

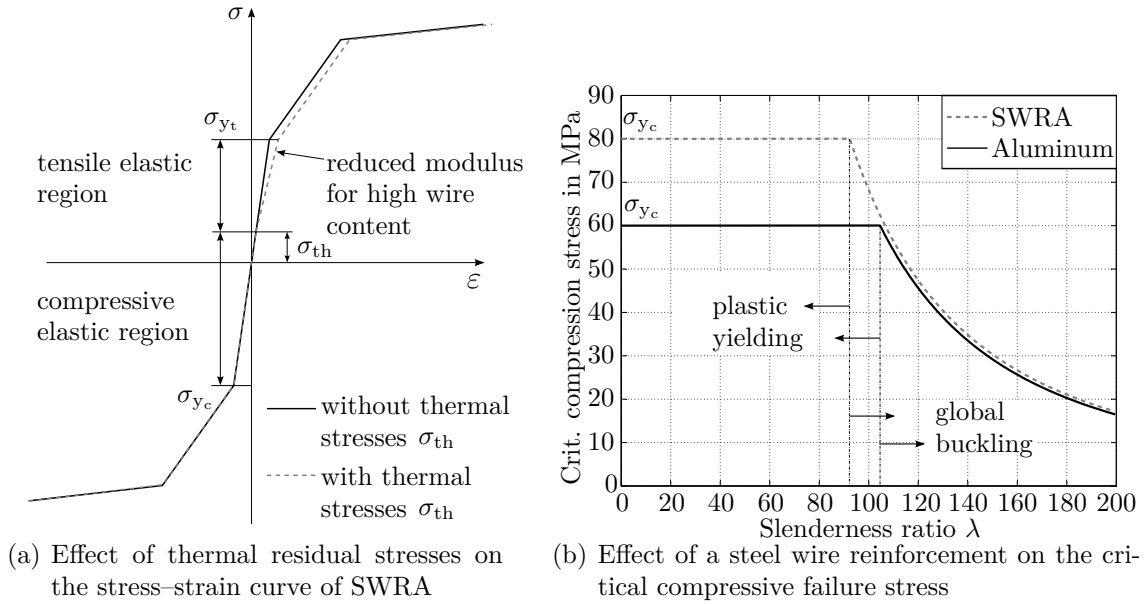


Figure 2.5.: Effects of thermal residual stresses on the compressive failure behavior of SWRA

forcement with 2% wire content with respect to the non-reinforced aluminum alloy. Further benefits from a steel-wire reinforcement for controlling a local buckling or progressive buckling modes were not found [7].

Using SWRA in crash absorbing structures, no relevant decrease of the material's crashworthiness due to thermal residual stresses is probable. With usually high strains arising during crash events, the residual stresses are released by plasticification of the material and do not further influence the plastic yield behavior. The initial prestress is further at a low level of prestrain, so that a significant reduction of the material's ductility does not occur. For a first estimation of the crashworthiness of structures made from SWRA, previous investigations on the fracture behavior of the material are discussed in the following.

2.4. Investigations on the suitability of SWRA for energy absorbing structures

Many previous analyses, albeit not focusing on the crashworthiness of structures made of SWRA, allow insight on the fracture behavior of SWRA. The resistance to fracture is one keypoint to a crashworthy structure, and, therefore is discussed in this section.

Crashworthiness does not directly translate into one exclusive material property, as many structural properties amount to a crashworthy structure. For the example of an axially compressed crash tube, which is often used as a crash absorber in the

crumple-zone of a car, its geometry, its folding behavior, the robustness of the folding pattern and many other, non-material related properties determine the absorbed energy [2, 53]. Focusing on material properties, the kinetic crash energy is converted into strain energy which is

$$U = \int_V \boldsymbol{\sigma} : \boldsymbol{\varepsilon} dV \quad (2.12)$$

with the stress tensor $\boldsymbol{\sigma}$ and the strain tensor $\boldsymbol{\varepsilon}$.

It can be deduced, that high strains at a high level of stress translate into a high energy absorption. A late onset of material failure and fracture is necessary to reach and sustain high stress and strain levels. The theoretical increase in ultimate strength was discussed in section 2.2 according to the model of Kelly [58] and was experimentally confirmed for SWRA by Weidenmann [124]. For a wire content of 2%, the ultimate strength is increased by about 30%, which is promising for a high energy absorption. This increased stress level must be accompanied by high bearable strains, so that a benefit in terms of energy absorption results.

The reinforcing wire, however, possesses a fracture strain of only about $e_{fr} \approx 1.8\%$, so that despite its high tensile strength, the strain energy until fracture is relatively low. The wire fails — in non-embedded state — due to necking and subsequent fracture. Embedding the wires into the aluminum matrix results in a tremendously increased fracture strain of the wires to approximately $e_{fr} > 20\%$ (see figure 2.3(a)). Piehler [90] attributes the increase in fracture strain to a lateral restraint which the matrix applies on the wire and, thus, keeping it from necking and subsequent ductile fracture. This was confirmed by [81] by means of FEM simulation of the interface stresses during axial straining of SWRA.

Based on the tensile test results of non-reinforced matrix and SWRA in figure 2.3(a), a comparison of the strain energy until fracture at pure axial tension is possible. Although pure tension is certainly not a representative load case for crash events, it is the load case at which SWRA benefits most of the reinforcement. A comparison of the strain energy until fracture can, therefore, indicate the suitability of SWRA for energy absorption. In addition, tension transversal to the reinforcement direction is known as a load case provoking early fracture for unidirectionally reinforced composites and, therefore, exposes how critical loads influence the capacity for energy absorption of SWRA.

Test specimens were taken from one extruded section similar to the one shown in figure 1.2(b) so that the non-reinforced and reinforced aluminum specimens possess equal extrusion and cooling conditions. For further information see also [106].

As measure for strain energy during the tensile tests, the engineering strain energy density per unit volume is taken which is

$$U_0 = \int_0^{\tilde{\varepsilon}} s de \quad (2.13)$$

with the upper strain integration limit $\tilde{\epsilon}$, the engineering strain e and the engineering stress s .

A base length between two reference points on the specimens for strain measurement was chosen and recorded using an optical measurement system¹. For the tests in wire direction, the gauge length is 15 mm, for the tests transversal to wire direction it is reduced to 6 mm, as the width of the extruded section limited the specimen's width. The requirements of the standard specification² for the geometry of the transversal test specimens could, thus, not be met. The specimens' geometries are shown in figure 2.6(a).

Necking and fracture took place in all cases within the measurement length. Due to the different measurement lengths, the test results in wire direction (in 0°-direction for non-reinforced aluminum) and transversal to wire direction (in 90°-direction for non-reinforced aluminum) are only comparable up to the end of uniform elongation e_u . After onset of necking, the measured strains depend on the measurement length, causing increased calculated strains for smaller measurement lengths. The comparability between all specimens, thus, is given until uniform elongation e_u and after that only persists for the specimens of each direction. The results of the tensile tests are shown in figure 2.6(b) and the resulting strain energy densities are summed up in table 2.3.

Comparing SWRA in wire direction with the non-reinforced aluminum, it is obvious that SWRA gains in strain energy density due to a higher strain hardening capability. However, material failure by necking sets in earlier compared to the non-reinforced aluminum matrix. The gain in strain energy density until uniform elongation is at about 17%. After the onset of material failure, SWRA shows a less ductile material fracture with a decreased fracture strain. The profit in strain energy density is at a mere 5.4% compared to the non-reinforced aluminum.

Comparing the tensile test data transversal to wire direction with the non-reinforced aluminum in 90°-direction, an early failure and fracture of the reinforced specimen is striking. This is caused by an early debonding of the wire from the matrix, creating a void in the material and leading to necking and fracture [106]. The strain energy density compared to non-reinforced aluminum is reduced by 62% taking the uniform elongation as integration limit and by an overall 56.4% taking the fracture strain as a integration limit. These values serve as a first indication of the suitability of SWRA for crash energy absorbing structures.

Since material failure and fracture are local processes, the determined strain energy densities until final fracture are less significant, than the values until uniform elongation. Nevertheless, the higher strain energy density until final fracture points towards a higher fracture toughness of SWRA in wire direction, compared to the non-reinforced aluminum alloy.

An obvious decrease in strain energy density during tension transversal to wire di-

¹GOM Aramis

²DIN EN ISO 6892-1 [36]

Table 2.3.: Comparison of strain energy density until uniform elongation strain e_u and until fracture strain e_{fr} for steel-wire-reinforced and non-reinforced aluminum

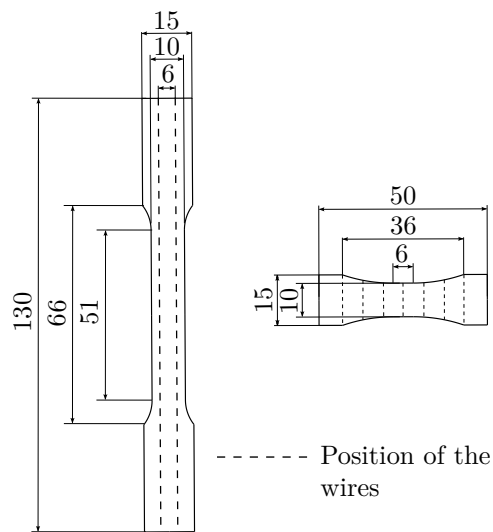
Property	SWRA wire direction	EN AW-6060 0°-direction	SWRA transversal direction	EN AW-6060 90°-direction
Strain energy density until e_u in $\frac{mJ}{mm^3}$	36.92	31.60	12.95	33.98
Strain energy density until e_{fr} in $\frac{mJ}{mm^3}$	64.10	60.84	35.20	80.67

rection is typical for unidirectionally reinforced composites. Diez [30] showed, that the failure and fracture strains for SWRA decrease with increasing tension transversal to the wire direction, so that these load cases ought to be avoided for structures of SWRA which are designed for energy absorption.

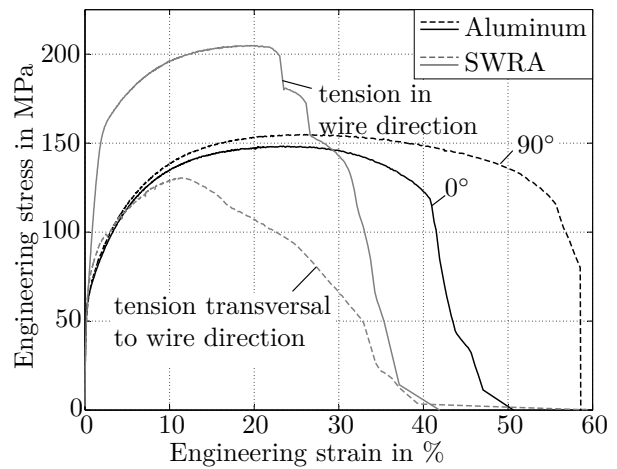
The previous analyses of SWRA are limited to quasistatic conditions. A crash incident, however, is by definition a highly dynamic event. This goes along with high strain rates in crash absorbing structures, which typically lie in the range of $\dot{\epsilon} = 70..200$ 1/s [126]. The high strain rates have an influence on the material behavior as they modify the strain hardening and fracture behavior. The results from quasistatic testing can be taken as first indicators for the crash behavior of a structure albeit they do not replace analyses at elevated strain rates.

One standard test to determine the impact toughness of a material is the notch impact test³. Weidenmann performed this tests at specimens of non-reinforced aluminum and SWRA with a wire content of 2.2% and a geometry according to the DVM specimen of DIN 50115 [33]. With an impact speed of $5 \frac{m}{s}$, the strain rate in the specimen lies above the usual strain rates for crash events, yet, the test gives a characteristic value for the material's impact strength at highly dynamic impacts. Weidenmann found an increase in notched impact strength for SWRA of 5.7..7.4%, which is in good accordance with the increase in strain energy density until fracture in wire direction at the tensile test (ca. 5.4%). Further, a small dependence of the notched impact strength on the surface-treatment of the steel wires prior to the composite extrusion was encountered [124].

³Charpy-test according to DIN EN 10045 [35]



(a) Geometry of tensile specimens in and perpendicular to wire direction; the non-reinforced specimens share the same geometry



(b) Tensile test results in and perpendicular to wire direction with the results of non-reinforced aluminum in and perpendicular to extrusion direction as reference

Figure 2.6.: Non-reinforced and reinforced tensile specimens and test results for tension in and perpendicular to wire direction as well as in and perpendicular to extrusion direction

3. Material models for dynamic impact loading and parameter identification

The experiments discussed in section 2.4 evaluate possible improvements in the energy absorption of an aluminum alloy by steel wire reinforcement and give insight into the mechanical behavior of SWRA. For a fundamental determination of the behavior of structures made of SWRA subjected to impact loads, a thorough material characterization must be completed. Based on this characterization, calibrated material models and simulation models allow for a more general understanding of SWRA and structures made of it.

This chapter first introduces basic theory for the mathematical material description for elasticity and plasticity. Subsequently, the experimental identification process for each aspect of the material's elasticity and plasticity is described in general and for SWRA in particular. A determination of material failure and fracture properties is equally important and, therefore, is treated in detail in chapter 4.

3.1. Basic mathematical descriptions for the behavior of ductile metals

Material characterization must be carried out with respect to the objective of the analysis. For a purely elastic analysis of the material, the determination of linear-elastic properties is sufficient. For high plastic deformations, an additional identification of the material's plastic behavior in terms of yield surface and strain hardening is vital. If the plastic deformation is at high strain rates, a strain rate hardening has to be anticipated.

For structures subjected to a crash event, a continuum description of the material's plasticity excluding failure must include

- elastic properties
- plastic properties as
 - yield surface,
 - strain hardening,
 - strain rate hardening.

Before discussing these aspects of a material description, the used strains and stresses need to be defined.

3.1.1. Measures of strain for infinitesimal and finite strains

Measuring strains and stresses, a manifold of strain and corresponding stress tensors can be used. Thus, it is important to define the here used measures to ensure comparability of the presented results. The theory on strain measures is kept as brief as necessary and [38, 61] are recommended for further information.

Starting with the fundamentals of continuum mechanics and the description of deformations, the shift of a point with coordinates \mathbf{X} in undeformed state to a new position with coordinates \mathbf{x} in deformed state is either described by the displacement vector \mathbf{u} or the displacement gradient \mathbf{F} [38]

$$\mathbf{x} = \mathbf{X} + \mathbf{u} \quad (3.1)$$

and

$$\mathbf{F} = \frac{\partial \mathbf{x}}{\partial \mathbf{X}}. \quad (3.2)$$

For the description of an elastic deformation with (infinitesimally) small strains, the Green-Lagrange strain tensor \mathbf{E} is calculated from \mathbf{F} by [38]

$$\mathbf{E} = \frac{1}{2} (\mathbf{F}^T \mathbf{F} - \mathbf{I}). \quad (3.3)$$

with \mathbf{I} being the identity matrix.

Using the continuous displacement field \tilde{u}_i acting on a three-dimensional body in the i -dimension (with $i=1..3$), the Green-Lagrange strains are expressed by [61]

$$E_{ij} = \frac{1}{2} \left(\frac{\partial \tilde{u}_i}{\partial x_j} + \frac{\partial \tilde{u}_j}{\partial x_i} + \frac{\partial \tilde{u}_k}{\partial x_i} \frac{\partial \tilde{u}_k}{\partial x_j} \right). \quad (3.4)$$

As the elastic strains are usually small, a linearization of the Green-Lagrange strains is, in this domain, admissible and valid over a broad range of structural operational conditions. As the linearization also includes a small-angle approximation, care has to be taken for rotations. The then resulting linearized tensorial strain components are

$$E_{ij}^{\text{lin}} = \frac{1}{2} \left(\frac{\partial \tilde{u}_i}{\partial x_j} + \frac{\partial \tilde{u}_j}{\partial x_i} \right). \quad (3.5)$$

They correspond to the well-known engineering strains via

$$E_{ii}^{\text{lin}} = e_{ii} \text{ and} \quad (3.6)$$

$$E_{ij}^{\text{lin}} = \frac{1}{2} \gamma_{ij}, \quad (3.7)$$

$$(3.8)$$

with e_{ii} being the diagonal components of the engineering strain tensor and γ_{ij} the shear components of it.

For finite strains of plastic deformations with comparably high deformations, usually the logarithmic strains (Hencky strains) $\boldsymbol{\varepsilon}^{\text{log}}$ are used [38]

$$\boldsymbol{\varepsilon}^{\text{log}} = -\frac{1}{2} \ln \left(\left(\mathbf{F}^{-1} \right)^T \mathbf{F}^{-1} \right). \quad (3.9)$$

Using logarithmic strains offers some uniquenesses compared to other strain measures [15, 84], that are advantageous for high deformations as in crash incidents and forming operations, which include the following:

1. additivity of coaxial strains
2. possible decomposition of the strain tensor in a volumetric and isochoric part
3. for isochoric transformation, the trace of the strain tensor is zero
4. compression and tension are symmetric, so that the strain arising from stretching by a factor δ is minus the strain resulting from a compression by $1/\delta$.

The first and the last listed advantages of Hencky's strain tensor shall be briefly examined, where property 2 and 3 are important for the formulation of yield criteria, which are being discussed in section 3.1.3.

In order to visualize the property of additivity of coaxial strains, consider a rod of length l_0 being stretched to a final length l_3 . This shall be done in one step and alternatively in three steps with two intermediate stretches to the lengths l_1 and l_2 .

$$e_{\text{tot}} = \frac{l_1 - l_0}{l_0} + \frac{l_2 - l_1}{l_1} + \frac{l_3 - l_2}{l_2} \neq \frac{l_3 - l_0}{l_0}. \quad (3.10)$$

The total engineering strains for the three subsequent stretches are not equal to the engineering strains that would arise for the one step stretch. Using the logarithmic strain measure, the additivity of coaxial strains is proven by

$$\varepsilon_{\text{tot}} = \ln \left(\frac{l_1}{l_0} \right) + \ln \left(\frac{l_2}{l_1} \right) + \ln \left(\frac{l_3}{l_2} \right) = \ln \left(\frac{l_1 \cdot l_2 \cdot l_3}{l_0 \cdot l_1 \cdot l_2} \right) = \ln \left(\frac{l_3}{l_0} \right) \quad (3.11)$$

The symmetry of the strain arising from an equal compression and tension stretch follows from the additivity of coaxial strains. Ensuring additivity, the logarithmic

strain measure, therefore, is better suited to capture the influence of the strain path on the final strain, particularly for high deformations. Their energy conjugate stresses are the Kirchhoff stresses, which are equal to the Cauchy stresses for incompressible material [55]. The Cauchy stress σ is defined as current force F divided by current cross sectional area A

$$\sigma = \frac{F}{A}. \quad (3.12)$$

Determining the Cauchy stress is experimentally difficult as the current cross section area must be known. Measuring the engineering strain e , a transformation of the engineering stresses s into Cauchy stresses σ and of engineering strain to Hencky strain ε is possible,

$$\sigma = s \cdot (1 + e) \quad (3.13)$$

$$\varepsilon_{ii} = \ln(1 + e_{ii}). \quad (3.14)$$

In order to make a clear distinction, the Cauchy stress is referred to as “true stress” σ and the Hencky strain as “true strain” ε ; engineering values are referred to as “engineering strain” e and “engineering stress” s .

3.1.2. Isotropic elasticity

A mathematical description of isotropic elasticity is performed based on the Green–Lagrange strains. The energy conjugated stresses to the Green–Lagrange strains are the 2nd Piola–Kirchhoff stresses which are expressed using Kronecker’s delta δ_{ij} as [61]

$$\sigma_{ij}^{(2PK)} = \frac{E}{1 + \nu} \left(E_{ij}^{\text{lin}} + \frac{\nu}{1 - 2\nu} E_{kk}^{\text{lin}} \delta_{ij} \right). \quad (3.15)$$

or in an inverse notation [61]

$$E_{ij}^{\text{lin}} = \frac{1}{E} \left[(1 + \nu) \sigma_{ij}^{(2PK)} - \nu \sigma_{kk}^{(2PK)} \delta_{ij} \right]. \quad (3.16)$$

This shows that there is a unique relationship between strain tensor and stress tensor for isotropic elastic deformations. Such a unique relation is no longer given for plastic material behavior.

3.1.3. Plastic yielding

Reaching the elastic limit stress, the material starts to plastify. The change from elastic to plastic behavior for materials without a clearly distinguishable yield point is not at one definite stress but it is rather a smooth transition. It is common practice

to take the technical yield strengths $R_{p0.2}$ or $R_{p0.1}$ as reference values for onset of plastification, at 0.2 % or 0.1 % plastic strain respectively. Hecker [44] showed, that this arbitrary choice of the yield point has consequences for the attributed material behavior. Choosing the yield point at no offset plastic strain tends to result in a more anisotropically predicted behavior, whereas higher admissible plastic strains at the yield point tends to result in a more isotropically predicted behavior.

The transition from elastic to plastic behavior is described by the yield condition

$$\Phi = \sigma - \sigma_y = 0 \quad (3.17)$$

with Φ being the yield condition and σ_y being the chosen yield strength.

Generalizing this for arbitrary multiaxial stress state, leads to a yield condition of the form

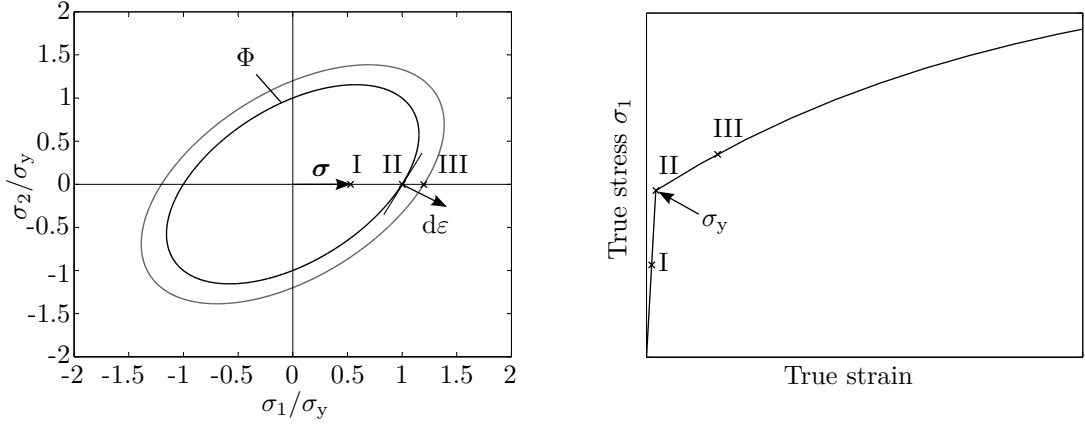
$$\Phi = \phi(\sigma_{ij}) - \phi_0 = 0. \quad (3.18)$$

$\phi(\sigma)$ is a general yield function with the stress tensor as argument and ϕ_0 is the chosen reference value depending on the yield function. The value of Φ determines whether a stress state is still in the elastic regime ($\Phi < 0$) or causes plastic yielding ($\Phi = 0$). Values of $\Phi > 0$ are not admissible, as the stress state must stay on the yield surface $\Phi = 0$ for plastic yielding. For a polycrystal material, Bishop and Hill [12, 19] showed, that the yield function is convex and the strain increment is normal to the yield function. Demanding convexity of the yield function, further, is necessary to ensure that the transition from one elastic state to another elastic state does not cross the plastic regime and cause plastic yielding. Convexity allows for the strain and strain increment to be decomposed into an elastic and plastic part, and a separate consideration of elasticity and plasticity. Although a general convexity of the yield function and normality of the strain increment are assumptions and deviations can be found [12], they are commonly accepted and allow an easy calculation of incremental plastic strains and stresses.

The yield function is then a potential for the plastic strain increments which are calculated differentially for plastic yielding according to the associated flow rule

$$d\varepsilon_{ij} = d\lambda \frac{\partial \phi}{\partial \sigma_{ij}}. \quad (3.19)$$

The directions of the strain increments are given by the yield function and the magnitude by the plastic multiplier $d\lambda > 0$. For a homogeneous convex yield function of first degree, the plastic multiplier equals the associated equivalent strain ε_{eq} , which is here chosen as the von Mises equivalent strain $d\lambda = \varepsilon_{eq}$ [12]. The magnitude of the strain increment is, therefore, given by a reference stress–strain relationship, which is given by the strain hardening function (see section 3.1.4). The interrelationship of strain hardening curve and yield function is visualized in figure 3.1. It is customary to use the stress–strain relationship from uniaxial tension as reference



(a) Plane stress von Mises yield locus with stress tensor for uniaxial tension (b) Exemplary stress–strain diagram of an uniaxial tensile test

Figure 3.1.: Interrelationship of yield function and strain hardening function

curve, although other reference stress states may be chosen.

The strain increment for an arbitrary, multiaxial stress state is then given by the plastic work equivalence

$$d\varepsilon_{\text{eq}} = \frac{\sigma_{ij}d\varepsilon_{ij}}{\sigma_{\text{eq}}} \quad (3.20)$$

with the von Mises equivalent stress σ_{eq} .

3.1.3.1. Isotropic yield functions

Widely used isotropic yield functions $\phi(\sigma_{ij})$ are for instance the von Mises yield function which relates yielding to the second invariant J_2 of the deviatoric stress tensor. In terms of principal stresses $\sigma_1 \geq \sigma_2 \geq \sigma_3$ it is

$$\Phi = (\sigma_1 - \sigma_2)^2 + (\sigma_2 - \sigma_3)^2 + (\sigma_3 - \sigma_1)^2 = 2\sigma_{\text{eq}}^2. \quad (3.21)$$

It can be interpreted as a criterion for maximum elastic distortion strain energy [138] or as maximum octahedral shear stress criterion [130]. It was originally proposed as an approximation to Tresca's yield criterion [12], which predicts yielding, once a maximum shear stress stress $\tau_{13_{\text{max}}}$ is reached

$$\Phi = \frac{\sigma_1 - \sigma_3}{2} = \tau_{13_{\text{max}}}. \quad (3.22)$$

The yield surface of isotropic metals with body-centered cubic (bcc) and face-centered cubic (fcc) lattices lies between the yield loci of von Mises and Tresca [12] and Hershey's yield function can be parametrized to fit experimental data by adapt-

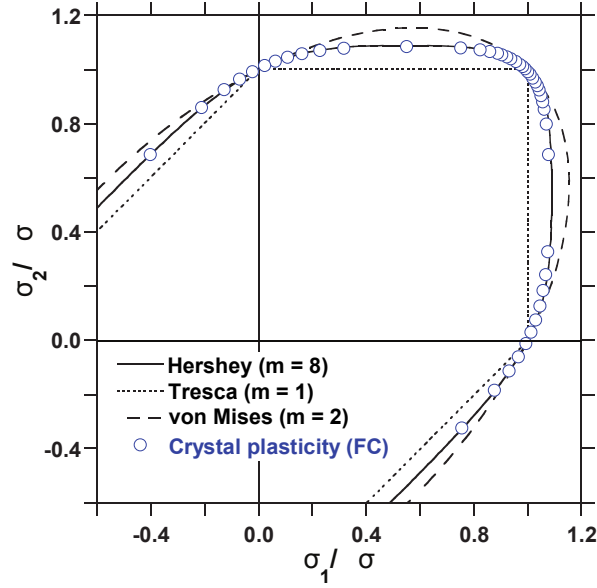


Figure 3.2.: Isotropic yield loci according to the predictions of von Mises, Tresca and Hershey ($m=8$) with a solution derived with a full constraint model of an isotropic fcc material, adapted from [12]

ing the yield function exponent m [45]. Hershey's criterion can be seen as a generalization of von Mises' criterion

$$\Phi = |\sigma_1 - \sigma_2|^m + |\sigma_2 - \sigma_3|^m + |\sigma_3 - \sigma_1|^m = 2\sigma_{\text{eq}}^m. \quad (3.23)$$

It reduces to von Mises' criterion for $m=2$ and $m=4$ and to Tresca's for $m=1$ and $m \rightarrow \infty$ [12]. The discussed isotropic yield functions are shown in figure 3.2 together with a calculated yield locus for an isotropic fcc material based on a full constraint model [12].

3.1.3.2. Orthotropic yield functions

Hundreds of yield functions have been formulated during the 20th century [129], making a thorough discussion infeasible. A good overview is, nevertheless, given by Życzkowsky [138] and also by Yu [129, 130]. This section is confined to three yield functions frequently used in engineering practice: Hill's "Hill'48" [46] and Barlat's "Yld'89" [14] as well as "Yld'91" [13] and discusses them for the description of plastic yielding of extruded aluminum sections.

Due to the extrusion conditions, the sections exhibit an orthotropic plastic yield behavior with three axes of symmetry. These are the extrusion direction x , the transverse direction y and the normal direction z of the extruded product. Whereas the isotropic yield functions are independent to the coordinate system, the orthotropic yield functions must be expressed with respect to these axes of symmetry.

Von Mises proposed a general yield criterion for anisotropic materials [12],

$$A_{ijkl}\sigma_{ij}\sigma_{kl} = 1 \text{ with } A_{ijkl} = A_{jikl} = A_{ijlk} = A_{ijlk}, \quad (3.24)$$

with the anisotropy coefficients A_{ijkl} . Due to the symmetry condition of the stress tensor, the number of coefficients reduces from 81 to 21.

Hill's criterion Hill'1948 Hill [46] generalized the isotropic von Mises yield criterion (3.21) to orthotropic conditions with F, G, H, L, M, N being the parameters of orthotropy. The resulting criterion can be regarded as a special case to equation (3.24) [12],

$$F(\sigma_y - \sigma_z)^2 + G(\sigma_z - \sigma_x)^2 + H(\sigma_x - \sigma_y)^2 + 2L\sigma_{yz}^2 + 2M\sigma_{xz}^2 + 2N\sigma_{xy}^2 = \sigma_{eq}^2. \quad (3.25)$$

For plane stress conditions, its coefficients are determined from tensile tests at thin sheet specimens in different orientations to the extrusion direction, making parameter identification an easy process. It can be fully parametrized knowing the Lankford parameters or r -values, [3]

$$r_\varphi = \frac{\varepsilon_w}{\varepsilon_t}, \quad (3.26)$$

which give the relation of plastic strain in width direction ε_w to plastic strain in thickness direction ε_t for a given orientation φ to the extrusion direction.

For plane stress conditions and with principal stresses, the criterion is [10]

$$\sigma_1^2 - \frac{2r_0}{1+r_0}\sigma_1\sigma_2 + \frac{r_0(1+r_{90})}{r_{90}(1+r_0)}\sigma_2^2 = \sigma_{eq}^2. \quad (3.27)$$

The simple experimental identification of the parameters contributes to the wide use of Hill's criterion in engineering practice. However, it is not suitable for most aluminum alloys, since it cannot properly describe the behavior of plastic yielding. Since aluminum alloys did not follow the predicted behavior by Hill's criterion, their behavior was termed *anomalous behavior* [128].

Having an average strain ratio of width to thickness strain $\bar{r} < 1$, it can be shown by Hill's yield criterion, that the yield stress in biaxial tension σ_b must not be higher than the yield stress in uniaxial tension since [3]

$$\frac{\sigma_b}{\sigma_0} = \left(\frac{1+\bar{r}}{2}\right)^{\frac{1}{2}} > 1 \text{ for } \bar{r} < 1. \quad (3.28)$$

A further *anomalous behavior* can be stated when looking at a case of pure tension in transverse (90°) -direction which gives [3]

$$\frac{\sigma_0}{\sigma_{90}} = \sqrt{\frac{r_0(r_{90} + 1)}{r_{90}(r_0 + 1)}} \quad (3.29)$$

with the yield strengths σ_0 and σ_{90} in 0° -direction and 90° -direction, respectively. According to Hill's criterion, a ratio of $r_0/r_{90} < 1$, thus, demands that the yield strength σ_0 must be lower than σ_{90} , i.e., $\sigma_0/\sigma_{90} < 1$, which is not always given for aluminum alloys. The considered aluminum alloy experiences the anomalous behavior of equation (3.28) as seen in table 3.2. Thus, Hill's yield criterion is not suitable for further analyses.

Barlat's criterion Yld'89 Barlat suggested a plane stress orthotropic yield function, which can capture the anomalous behavior and whose parameters can also be identified by simple tensile test data [14]. It is referred to as Yld'89 and described by

$$\Phi = a |K_1 + K_2|^m + a |K_1 - K_2|^m + c |2K_2|^m = 2\sigma_{\text{eq}}^m, \quad (3.30)$$

with

$$K_1 = \frac{\sigma_x + h\sigma_y}{2}, \quad (3.31)$$

$$K_2 = \sqrt{\left(\frac{\sigma_x - h\sigma_y}{2}\right)^2 + p^2\sigma_{xy}^2} \quad (3.32)$$

and

$$a = 2 - 2\sqrt{\frac{r_0}{1+r_0} \frac{r_{90}}{1+r_{90}}}, \quad (3.33)$$

$$c = 2 - a, \quad (3.34)$$

$$h = \sqrt{\frac{r_0}{1+r_0} \frac{1+r_{90}}{r_{90}}}. \quad (3.35)$$

The remaining exponent m is chosen as $m = 6$ for bcc lattice and $m = 8$ for fcc lattice similar as in Hershey's function. For $m = 2$, Yld'89 reduces to Hill'48. The remaining parameter p is chosen numerically by following procedure.

The r-value in each orientation φ to the extrusion direction can be expressed as [14]

$$r_\varphi = \frac{2m\sigma_{\text{eq}}^m}{\left(\frac{\partial\Phi}{\partial\sigma_x} + \frac{\partial\Phi}{\partial\sigma_y}\sigma_\varphi\right)} - 1. \quad (3.36)$$

Using equation (3.36) and an experimental r-value for a direction φ is then used to search for a parameter p , which gives the best prediction for the chosen experimental r-value [67].

Even though Barlat's plane stress yield function is able to capture the previously described anomalous behavior, it was found erroneous for the use with aluminum alloys exhibiting high anisotropy [9]. Yld'89 was successfully used to simulate three-point-bending tests of extruded, non-reinforced aluminum sections and performed reasonably well [80]. As it is limited to plane stress conditions, it is not suited for the use with SWRA, which has a non-planar stress state, particularly around the steel wires.

Barlat's six-component yield criterion Yld'91 For SWRA extrusions, the out-of-plane stresses cannot be neglected, since the through-thickness strains are influenced by the wires. In order to take three-dimensional states into account, Barlat introduced a six-component yield criterion [13]. It operates on Hershey's isotropic yield function and is referred to as Yld'91,

$$\Phi = |S_1 - S_2|^m + |S_2 - S_3|^m + |S_3 - S_1|^m = 2\sigma_{\text{eq}}^m, \quad (3.37)$$

with the eigenvalues S_k ($k = 1..3$) of the stress deviator $[\mathbf{s}]$

$$[\mathbf{s}] = \begin{bmatrix} \frac{cC-bB}{3} & hH & gG \\ & \frac{aA-cC}{3} & fF \\ \text{sym} & & \frac{bB-aA}{3} \end{bmatrix}, \quad (3.38)$$

with the Bishop–Hill abbreviations [19]

$$A = \sigma_{yy} - \sigma_{zz}, \quad (3.39)$$

$$B = \sigma_{zz} - \sigma_{xx}, \quad (3.40)$$

$$C = \sigma_{xx} - \sigma_{yy}, \quad (3.41)$$

$$F = \sigma_{yz}, \quad (3.42)$$

$$G = \sigma_{zx}, \quad (3.43)$$

$$H = \sigma_{xy}, \quad (3.44)$$

$$(3.45)$$

and the anisotropy coefficients a, b, c, f, g, h .

Knowing the yield strengths from several load cases, these coefficients are usually determined numerically in a non-linear fitting process. Additional knowledge can be introduced into the fitting process by using the associated flow rule (3.19) and the corresponding yield strengths. The r-values are, thereby, calculated depending on the anisotropy coefficients and compared with the experimental r-values. Since the yield function parameters are not directly defined by r-values or yield strengths, the effort for parameter identification is higher compared to Hill's yield function. Wang [118] used the associated flow rule to calculate the anisotropy coefficients solely depending on measured r-values, which is a direct and convenient approach for parameter identification. For a simulated sheet metal forming process, the deduced

yield function fit well. However, his formulae are erroneous, which was discussed with the author. The formulae shown here are based on a revision by Wang [117], which is in accordance with a calculation by Pfaffinger [88].

Using the associated flow rule and after a lengthy calculation, it can be shown that [117]

$$r_0 = \frac{2c^2 + ac + bc - ab}{2b^2 + bc + ab - ac} \quad (3.46)$$

$$r_{45} = \frac{9h^2 - b^2 - ab - a^2}{2b^2 + 2ab + 2a^2} \quad (3.47)$$

$$r_{90} = \frac{2c^2 + ac + bc - ab}{ab - bc - 2a^2 + ac} \quad (3.48)$$

$$r_b = \frac{2a^2 + ac + ab - bc}{2b^2 + bc + ab - ac} \quad (3.49)$$

$$(3.50)$$

or generally for an arbitrary angle φ to the extrusion direction

$$r_\varphi = \frac{9\sin(2\varphi)\sigma_{xy}h^2 - \sin^2(\varphi)[2\sigma_{xx}(b^2 + c^2 + bc) + \sigma_{yy}(ab - 2c^2 - ac - bc)]}{\sigma_{xx}(2b^2 + bc + ab - ac) + \sigma_{yy}(ab - bc + 2a^2 + ac)} - \frac{\cos(\varphi)[\sigma_{xx}(ab - 2c^2 - ac - bc) + 2\sigma_{yy}(a^2 + c^2 + ac)]}{\sigma_{xx}(2b^2 + bc + ab - ac) + \sigma_{yy}(ab - bc + 2a^2 + ac)} \quad (3.51)$$

These formulae may add to a simplification of the process of parameter identification. Experimentally determining the out-of-plane parameters f and g , however, is demanding so that often $f = g = 1$ has to be assumed.

The advantages of Yld'91 are a high flexibility due to six stress components and an easy implementation to FEM code [9]. It can further be used with three-dimensional volume elements unlike many other yield criteria, which are restrained to plane stress conditions. Hence, it can for instance be used for the simulation of forming limits with a three-dimensional model and volume elements, allowing for a precise representation of geometrical imperfections in sheet metal as presented by [80].

3.1.4. Plastic strain hardening

As shown in figure 3.1, the amount of strain hardening is given by the strain hardening curve, which is usually taken from a tensile test. The multiaxial strain hardening is related to the uniaxial stress state by the plastic work equivalence (3.20). It is, therefore, essential that the tensile test is performed at pure uniaxial tension. Since elasticity and plasticity are considered by separate models, the strain is decomposed into elastic and plastic parts.

The elastic part is often much smaller than the plastic part (for instance at for-

Table 3.1.: Analytical strain hardening functions for the approximation and extrapolation of experimental strain hardening data

Analytical function	Hardening function
Ludwik (1909) [68]	$\sigma_{\text{eq}} = \sigma_y + K \cdot \varepsilon^n$
Hollomon (1945) [49]	$\sigma_{\text{eq}} = K \cdot \varepsilon^n$
Voce (1948) [114]	$\sigma_{\text{eq}} = \sigma_s - (\sigma_s - \sigma_y) \cdot \exp(-\varepsilon/\varepsilon_0)$
Swift (1952) [108]	$\sigma_{\text{eq}} = K \cdot (\varepsilon_0 + \varepsilon)^n$
Hockett–Sherby (1975) [48]	$\sigma_{\text{eq}} = \sigma_s - (\sigma_s - \sigma_y) \cdot \exp(-(N \cdot \varepsilon)^p)$

ming operations) and can be neglected [95]. In cases that the elastic part cannot be neglected, for instance with high strength steels with high ultimate strain ε_u , the true plastic strain needs to be separated from the measured total strain according to [37]

$$\varepsilon_{\text{pl}} = \ln \left(\frac{l_0 + \Delta l}{l_0} - \frac{F}{A_0 \cdot E} \right) \quad (3.52)$$

with the initial gauge length l_0 , the length in deformed state l and the initial cross section area A_0 .

The experimentally determined relation between true stress σ and true plastic strain provides data for the determination of the plastic strain hardening relationship. However, the data becomes invalid after the onset of necking, which is at ultimate strain ε_u , i.e. at maximum force. Beyond this point, the tensile specimen starts to neck, the uniaxial stress state transforms to a triaxial stress state and can no longer serve as a reference stress state. Therefore, the measured data must be extrapolated for higher strains. In order to extrapolate the limited experimental data, analytical functions are used. Table 3.1 lists some of the most popular functions.

While the fitted functions often closely approximate the experimental data, the validity of the extrapolated strain hardening curve is uncertain. Figure 3.5(a) shows, how different strain hardening functions lead to different extrapolations.

The uncertainty of the extrapolated data is problematic for the simulation of processes with high strains as in forming operations or crash simulations. Therefore, different approaches for the determination of the post-necking strain hardening behavior are discussed in the following.

3.1.4.1. Experimental determination by compression testing

At tensile tests, a reduction of the specimen's cross section and onset of necking ultimately limit the validity of the data. For compression tests of small coupon-specimens, necking does not occur and the strain hardening data is valid over a

wider range. The specimen is compressed between two hardened plates, leading to a stress state of uniaxial compression. Assuming an isosensitive¹ behavior of the material, the strain hardening data from uniaxial compression is equivalent to the one from uniaxial tension.

A lubrication between specimen and compression plates is necessary to reduce friction and keep the specimen from bulging out (also called “barreling”). This would lead to an unknown state of stress, rendering the obtained data invalid. Graphite and teflon lubricant sprays were found effective for the use with aluminum coupons [11, 88]. Rastegaev [96] suggested a cylindrical specimen with lubrication pockets for further reducing the friction and Taylor and Quinney [109] proposed to perform gradual compression tests with an intermediate removal of the barreling after each step. Both methods are able to reduce the barreling of the compression specimens, however, the preparation of the specimens is tedious and the milling process influences the mechanical properties of the specimen.

In order to test thin sheet material as in thin walled extrusions, a layered stack of coupons is tested [41]. Lubrication on either sides of the single coupons helps reducing friction and barreling. Since the compression specimens are stacked, care has to be taken for orthotropic sheet, which has to be stacked according to its texture. An experimental setup of a layered compression test is shown in figure 3.3(a) with the stacked coupons prior and after testing in figure 3.3(b).

3.1.4.2. Experimental determination by the torsion testing

A further test method for cylindrical bars is the torsion test. A torsional momentum M on a bar which is fixed at one end results in shear stresses τ and a distortion γ . With the assumption of von Mises isotropy and homogeneity of the material, τ and M relate by [62]

$$\tau = \frac{3M}{2r^2\pi} \left[1 + \frac{1}{3M} \left(\gamma \frac{\partial M}{\partial \gamma} + \dot{\gamma} \frac{\partial M}{\partial \dot{\gamma}} \right) \right] \quad (3.53)$$

with the radius of the cylindrical bar r . Further assuming a Hollomon hardening type [49],

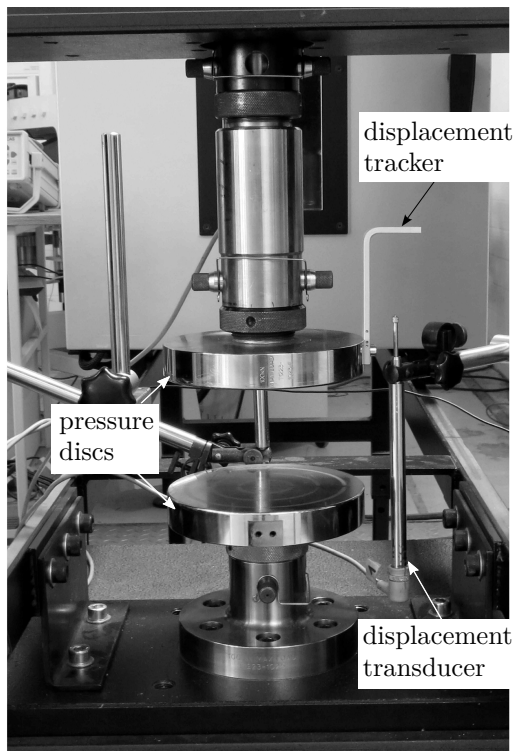
$$\tau = \tau_0 \gamma^n \dot{\gamma}^m, \quad (3.54)$$

the hardening function relates to the measured hardening parameters by [91]

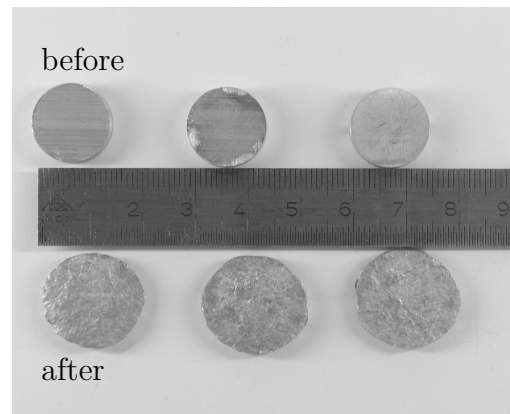
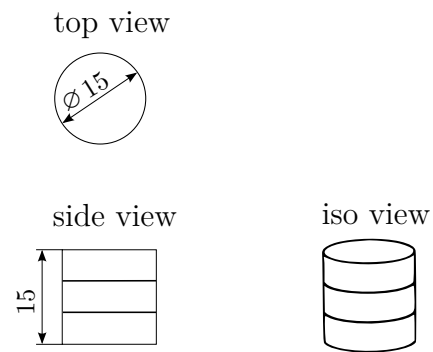
$$\sigma = 3^{(1+n+m)/2} \tau_0 \varepsilon^n \dot{\varepsilon}^m. \quad (3.55)$$

With a torsion test, high strains can be reached easily without material failure. Applying additional compression in the direction of the axis of distortion, the material can withstand even higher strains [21]. Yet, the assumptions of von Mises isotropy and a Hollomon type hardening make it a rather inaccurate method for assessing

¹an isosensitive material does not change in behavior, if the sign of all stress components is changed simultaneously [12]



(a) Test setup for a layered compression test



(b) Geometry of the compression specimens and deformed state after compression

Figure 3.3.: Layered compression test and specimen geometry before and after testing

the real strain hardening. Lange [62] points out that if the material has a Tresca-like yield locus an error in yield stress of up to 24% results thereof. And Pöhlandt [91] argues, that the uncertainty due to the assumption of the validity of the Hollomon hardening is even higher than between a von Mises and Tresca isotropy [93].

In spite of these uncertainties, the torsion test is suitable for the determination of the strain rate sensitivity of a material. This is due to the fact that the calculation of the strain rate sensitivity is independent of the mentioned uncertainties. For sheet material or thin extruded material, a modified torsion test can be done under plane torsion [93].

3.1.4.3. Correction methods for the strain hardening determined from post-necking tensile test data

Torsion tests as well as compression tests are both capable of experimentally determining the strain hardening data for a wide range of strain, without losing validity due to failure or fracture of the specimen. They are, however, difficult to conduct and to analyze. Particularly the torsion test suffers of uncertainty of the determined data. The ordinary tensile test remains the easiest way to gain reliable data and standardized specimens allow for a direct comparison of tensile test data.

After onset of necking, the strains in the neck reach high values due to strain localization, however, the recorded data is invalid, since the current cross section area and the stress state is unknown. Several approaches have been made to use the post-necking test data and extend the significance of tensile test. They are briefly discussed in the following.

Bridgman correction Bridgman [21] recorded the radial-symmetrical neck in cylindrical specimens and derived the stress state after onset of necking, assuming a von Mises isotropy of the material. He then managed to deduce a correction formula for cylindrical specimens, which allows for the use of the post-necking tensile test data for the determination of the strain hardening curve. With optical measurement techniques, it is, nowadays, fairly easy to constantly record the shape of the neck in cylindrical specimens. However, flat specimens are generally preferred, as flat sheet and thin extruded sections are unfit for the machining of cylindrical specimens. Bridgman also suggested a correction formula for flat specimen with the assumption of an infinitely wide specimen in order to avoid boundary effects [21]. This assumption does not hold true for flat specimens of finite geometry, which show a pronounced inhomogeneous flow in width direction also called “cushioning effect” [26].

Inverse FEM approach FE-based approaches offer a simple and versatile method for the determination of the strain hardening curve, based on simple tensile tests. The geometry of the specimen is not bound to a cylindrical shape and many yield loci and strain hardening functions can be considered. Determining the real strain

hardening curve is based on an inverse FEM approach [26, 116, 131, 136], which compares simulated and experimental stress–strain curves or force–elongation curves and iteratively changes the material input parameters for the simulation until an agreement of simulated and experimental data is reached. A general scheme of the procedure is shown in figure 3.4.

If orthotropic yield loci shall be considered, an assessment of the yield behavior must be done prior to the inverse FEM determination of the strain hardening curve. Special care has to be taken to ensure a fully converged discretization of the FE model. Otherwise, the results are mesh-dependent and do not reflect the true strain hardening. As input parameters for the simulated strain hardening curve, polynomial functions [116], piecewise-linear functions [136] or analytical strain hardening functions [26] are reported. The approximating function must be monotonically increasing and smooth, which is ensured by the discussed analytical strain hardening functions in table 3.1, yet not automatically assured by piecewise-linear or polynomial functions. With an iterative fitting, the process can be tedious and the quality of the determined strain hardening function depends on many factors including mesh convergence as well as the approximating function and yield locus chosen.

Constrained fitting approach In order to improve the quality of extrapolated strain hardening data from tensile test data, Hora [50] suggested a constrained least-squares fitting approach. Considère’s criterion [27], determining the onset of necking in a tensile specimen depending on its strain hardening properties, is introduced into the fitting as a constraint. It states, that the onset of necking is at maximum measured force F_{\max} in the tensile test experiment, or

$$dF|_{F=F_{\max}} = 0. \quad (3.56)$$

Translated into the regime of true stress and true strain, this demands that the first derivative of the strain hardening function equals the strain hardening function at the point of ultimate strain

$$\left. \frac{d\sigma(\varepsilon)}{d\varepsilon} \right|_{\varepsilon=\varepsilon_u} = \sigma(\varepsilon_u). \quad (3.57)$$

A set of two constraints can be deduced for a constrained fitting approach

$$\left| \left. \frac{d\sigma^{\text{fit}}}{d\varepsilon} \right|_{\varepsilon=\varepsilon_u} - \sigma^{\text{fit}}(\varepsilon_u) \right| - \delta_1 \leq 0 \quad (3.58)$$

$$\left| \sigma^{\text{exp}}(\varepsilon_u) - \sigma^{\text{fit}}(\varepsilon_u) \right| - \delta_2 \leq 0. \quad (3.59)$$

Equation (3.58) constrains the fitted function to fulfill Considère’s criterion within the limit δ_1 . This constraint alone is not sufficient, as non-fitting functions may meet the criterion at higher or lower stress levels as the real strain hardening function. Therefore, the second constraint (3.59) ensures, that the stress at ultimate strain approaches the experimental ultimate stress within the limit δ_2 .

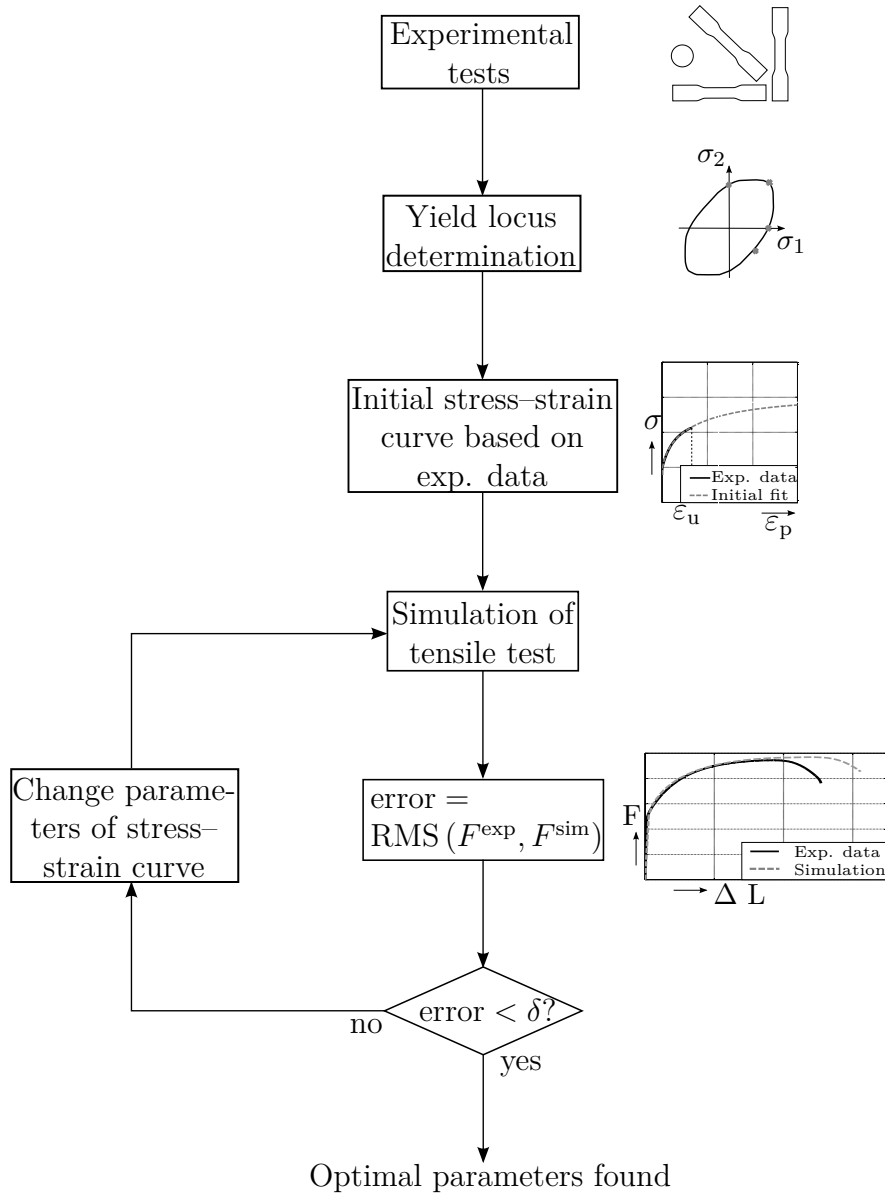


Figure 3.4.: Determination of the strain hardening curve by inverse FEM approach

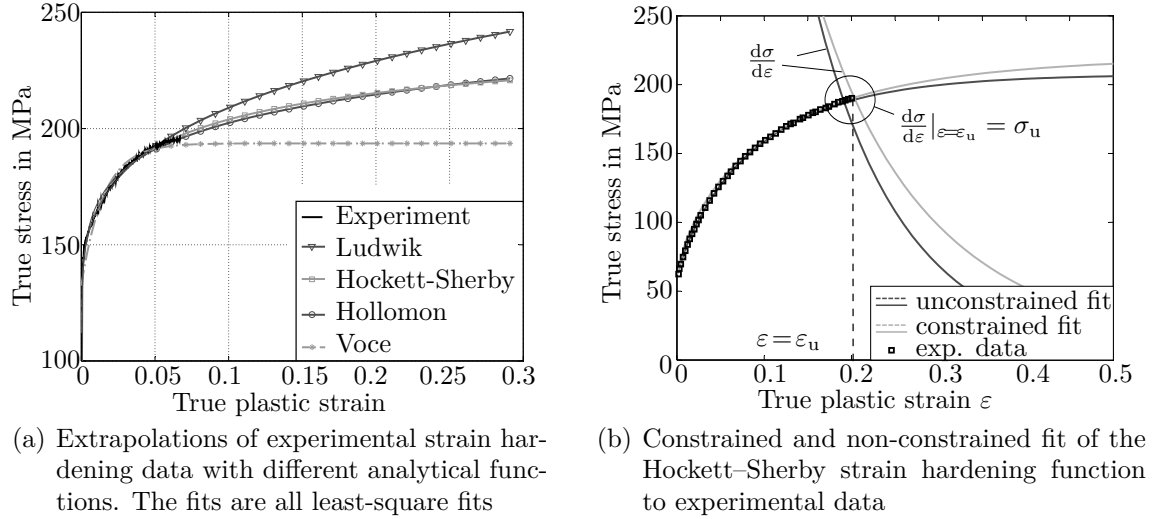


Figure 3.5.: Extrapolation of experimental strain hardening data with analytical functions — unconstrained and constrained fitting approaches

Based on compression test data of specimens from extruded sections of EN AW-6060 alloy, Pfaffinger [88] showed, that the constrained fitting approach gives a better extrapolation of the strain hardening data. This is not surprising, as more knowledge is introduced in the fitting process. If Considère’s criterion cannot be met by the strain hardening function, this indicates, that the strain hardening function chosen is not suitable for the examined material.

In figure 3.5(b), the experimental tensile test data of figure 3.5(a) from extruded sections of EN AW-6060 is taken and a non-constrained and constrained fitting of the Hockett–Sherby function is performed.

3.1.5. Strain rate and temperature dependent strain hardening

Many materials experience a strain rate dependent and temperature dependent hardening behavior, so that the strain hardening function is expressed as

$$\sigma = \sigma(\varepsilon, \dot{\varepsilon}, T). \quad (3.60)$$

During crash events, the maximum strain rates are up to $\dot{\varepsilon}_{\max} \approx 200 \text{ 1/s} \dots 500 \text{ 1/s}$ [99, 126] causing an increased flow stress of the material. Due to the adiabatic condition of the rapid deformation process, the arising deformation heat facilitates the deformation process by thermally activated dislocation motion, and an adiabatic softening of the material occurs [126].

Based on Hollomon’s equation, the strain rate sensitivity can be introduced with an additional multiplicative term

$$\sigma = K_H \varepsilon^{n_H} \dot{\varepsilon}^m \quad (3.61)$$

with m being the strain rate sensitivity exponent. It is generally calibrated based on flow curves at different strain rates and defined as

$$m = \frac{\ln(\sigma_1/\sigma_0)}{\ln(\dot{\varepsilon}_1/\dot{\varepsilon}_0)} \Big|_{\dot{\varepsilon}_{\text{ref}}, T}. \quad (3.62)$$

σ_0 and $\dot{\varepsilon}_0$ are reference values at quasistatic conditions and reference conditions $\varepsilon_{\text{ref}}, T$. σ_1 and $\dot{\varepsilon}_1$ are values at elevated strain rates at equal reference conditions.

From the definition of the strain rate sensitivity m , an easy model of constant strain rate sensitivity is deduced

$$\sigma_{\text{eq}}^{\text{dyn}} = \sigma_{\text{eq}}^{\text{qs}} \cdot \left(\frac{\dot{\varepsilon}^{\text{dyn}}}{\dot{\varepsilon}^{\text{qs}}} \right)^m, \quad (3.63)$$

where $\sigma_{\text{eq}}^{\text{dyn}}$ is the flow stress at the considered dynamic strain rate $\dot{\varepsilon}^{\text{dyn}}$ and $\sigma_{\text{eq}}^{\text{qs}}$ is the corresponding quasistatic flow stress at the quasistatic strain rate $\dot{\varepsilon}^{\text{qs}}$.

Campbell and Ferguson [23] tested mild steel (En3B) at a wide range of strain rates and temperatures by shear tests and Hopkinson-bar tests; the results are shown in figure 3.6. They distinguish three regions with different mechanisms causing a temperature and strain rate dependent flow stress.

The mechanisms leading to a strain rate and temperature dependent hardening were related to the thermal activation of motion of dislocations, a delayed motion of dislocations at obstacles such as stress fields, precipitates, or grain boundaries and a viscous resistance or damping of the dislocation movement (in region IV) [23]. For further theory on strain rate and temperature dependency of dislocation motion, the reader is referred to [23, 39, 115].

For automotive crash events, region IV with impact strain rates of $\dot{\varepsilon} > 5000$ 1/s are not reached and the corresponding effects are irrelevant. For lower strain rates, it can be seen that the strain rate sensitivity is not constant as in the above discussed model, but varies with the strain rate. This can be taken into account with the model of Cowper and Symonds [28]

$$\sigma_{\text{eq}}^{\text{dyn}} = \sigma_{\text{eq}}^{\text{qs}} \cdot \left(1 + \left(\frac{\dot{\varepsilon}}{C} \right)^{1/p} \right) \quad (3.64)$$

with the fitting parameters p and C .

Another empirical equation, which also considers thermal effects was proposed by Johnson and Cook [52]

$$\sigma_{\text{eq}}^{\text{dyn}} = \left(A + B\varepsilon_{\text{eq}}^n \right) \left(1 + C \ln \frac{\dot{\varepsilon}}{\dot{\varepsilon}_0} \right) \left(1 - \left(\frac{T - T_{\text{RT}}}{T_{\text{M}} - T_{\text{RT}}} \right)^m \right) \quad (3.65)$$

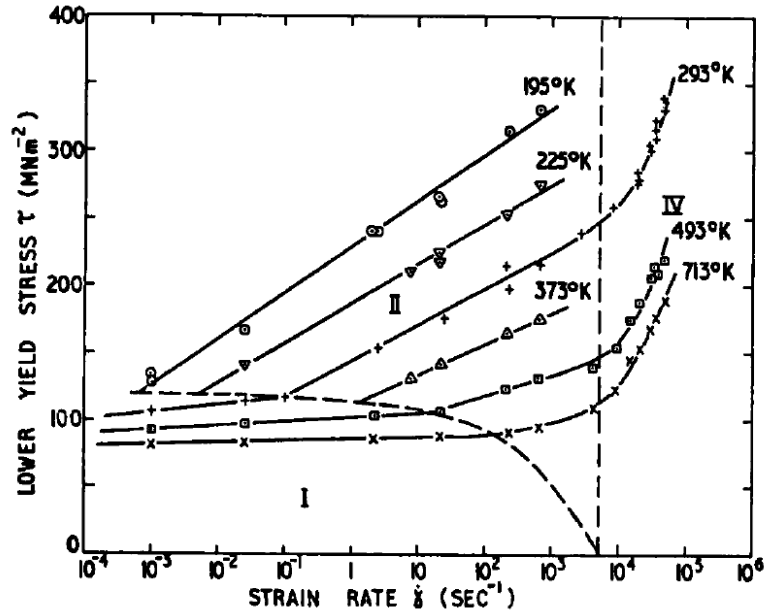


Figure 3.6.: Strain rate and temperature dependent yield stress for mild steel En3B determined from shear tests [23]

with a reference strain rate $\dot{\epsilon}_0$, the room temperature T_{RT} , the melting temperature T_M , the parameters A , B , C , n for the Ludwik-type strain hardening relation and m for the temperature dependence.

The models Cowper–Symonds and Johnson–Cook are available in most commercial FEM software, whereas physically deduced models such as Zerilli–Armstrong [135] or El-Magd [39] can be introduced by tabulated strain hardening curves [67]. A summary of further models taking strain rate and temperature dependency of the flow stress into account is given by [63].

3.2. Experimental determination of the plastic properties of aluminum matrix and steel wire

This section presents the experimental determination of the plastic properties of steel wire and aluminum matrix. The experiments are performed with the target of assessing the behavior of SWRA with respect to its fracture behavior and response to impact loads. As a reference, the non-reinforced aluminum alloy is characterized. Since the material properties of aluminum alloys vary with the production and tempering process, equal conditions need to be guaranteed for SWRA and non-reinforced aluminum alloy for a meaningful comparison. This was ensured by extruding a section with non-reinforced and reinforced sides as shown in figure 1.2(b), from which the test specimens are taken.

At the time of the investigations, the composite extrusion process was — for reinforced sections — limited to a minimum wall thickness of 5 mm and a maximum wire volume content of 2% in the reinforced sides. After extrusion, the sections were cooled down in still air and not further heat treated. This results in the heat treatment state T4(F) [31].

The process of parameter identification for the used models describing the plasticity of aluminum matrix and steel wire is divided in the sections of 'plastic yield surface', 'strain hardening properties' and 'properties of strain rate dependent hardening'.

3.2.1. Plastic yield surface

Aluminum matrix In order to determine a plastic orthotropic behavior introduced by the extrusion process, tensile specimens in 0°, 45° and 90° to the extrusion direction were tested by Matias and Stoeckl [72, 106]. The geometry of the specimens is limited by the geometry of the extruded section, so that standardized specimen geometries could only be met for the 0° direction². For the specimens in 45° and 90° to the extrusion direction, the maximum length was 50 mm, leading to stubby specimens as shown in figure 2.6(a). The strains were recorded with biaxial strain gauges [72] and an optical measurement system [106], enabling the detection of the Lankford parameters. Additionally flat shear specimens and layered-compression specimens were tested.

Table 3.2 lists the evaluated mean yield stresses and Lankford parameters with corresponding standard deviation for the tested specimens. The high scatter in yield strength for the 45°- and 90°-specimens, as well as in the r-values reveals, that the stubby specimens are not suitable for the determination of the data of plastic orthotropy. This is mainly due to their low width to thickness aspect ratio of $w/t = 2$, which leads to:

- a non-homogeneous, non-uniaxial stress state in the gage length
- a non-homogeneous plastic flow due to the specimen's edges, which lead to a higher plastic flow in the middle of the specimen (cushioning effect) [26].

Better aspect ratios could have been reached in two ways. Firstly, by testing extruded wider sections with similar extrusion conditions. Yet, the extruded sections were provided up to a maximum width of 56 mm only, thus, not offering much improvement. Secondly, a higher aspect ratio could have been reached by milling down the specimens on both sides to half of their original thickness, which preserves a representative texture. This would increase the aspect ratio and lead to a better reproduction of the real plastic flow behavior, however, an uniaxial stress state is still not guaranteed due to the limited length of the specimen. How much the milling process is changing the material's properties still needs further investigation.

²Geometry according to DIN EN ISO 10113 [37] and DIN 50125 [34]

Table 3.2.: Determined orthotropic yield stresses and yield ratios of the extruded, non-reinforced aluminum matrix EN AW-6060T4, values in brackets are standard deviations

Angle to extrusion direction	0°	45°	90°	Pure shear	Biaxial tension
Yield strength $R_{p0.2}$ in MPa	60.6 (0.41)	61.8 (7.00)	64.0 (2.12)	60.3 (4.3)	81.3 (0.95)
Flow ratio r_φ	0.50 (0.11)	0.42 (0.14)	0.79 (0.04)	0	0.90 (0.03)

Table 3.3.: Determined strain hardening parameters of the Hockett–Sherby function for the non-reinforced aluminum matrix EN AW-6060

Yield strength σ_y	Saturation stress σ_s	Hardening coefficient N	Hardening exponent p
54.36 MPa	206.87 MPa	10.24	0.819

Despite extruded aluminum having inherent orthotropy, an isotropic plastic yielding had to be assumed, considering the experimental difficulties and uncertainties of ascertainable parameters. With an advance of the current production process and higher press capacities for steel-wire-reinforced extruded sections, wider and thinner sections will allow for a more reliable determination of the parameters of plastic orthotropy and the presented yield functions can be used for a mathematical description.

Steel wire A determination even of simple characteristics of the steel wire is difficult, due to its small diameter of 1 mm. Micrographic analyses allow for a determination of the texture and an estimation of the inherent orthotropy, however, an experimental measurement of the yield strengths and r-values is limited to uniaxial tension and lateral compression [92].

SWRA has embedded steel wires, which are mainly stressed axially. Loads perpendicular to the wire’s axis cause an early debonding, so that the loads in the wire are confined mainly to uniaxial tension [30, 81]. Therefore, the simplifying assumption of an isotropic yield behavior is justifiable.

3.2.2. Strain hardening properties

Aluminum matrix The plastic strain hardening is evaluated with tensile tests of flat tensile specimens according to DIN 6892-1 [36]. An extrapolation of the strain hardening data is done with a constrained fitting approach and the strain hardening function of Hockett and Sherby, with the assessed function parameters shown in table 3.3.

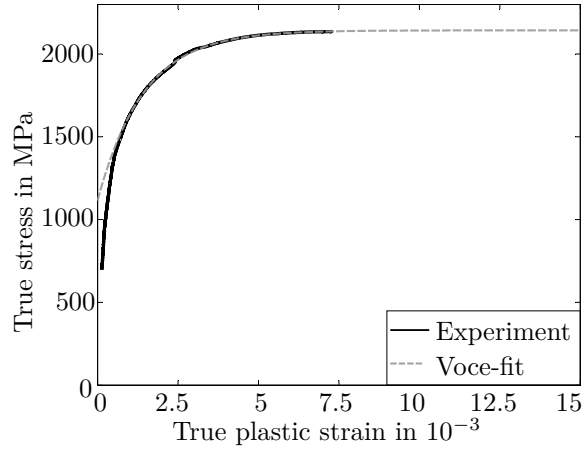


Figure 3.7.: Experimental strain hardening of the steel wire and extrapolation with Voce’s strain hardening function [81]

Table 3.4.: Parameters of Voce’s strain hardening function for the high-strength steel wires [81]

Yield strength σ_y	Saturation stress σ_s	Prestrain ε_0
1115 MPa	2143 MPa	0.00143

Steel wire The strain hardening of the steel wire was determined by Merzkirch and Meissner [76, 77]. Single wires were clamped by friction, winding them around two rolls. Thus, notch stresses from clamping were kept low [76]. The test speed was 10 mm/min and the strain was recorded using strain gauges of type FLA-1-11 [76]. The resulting stress–strain diagram is depicted in figure 3.7, showing a low fracture strain of $e_{fr} < 2\%$ due to necking of the non-embedded wire. An extrapolation of the strain hardening data was done based on Voce’s strain hardening function, giving the parameters listed in table 3.4. Since the experimental data indicates a saturation of the strain hardening, a nearly perfectly plastic extension predicted by the extrapolation is chosen.

3.2.3. Properties of strain rate dependent hardening

Aluminum matrix Experimental analyses show a small increase in flow stress for 6xxx aluminum alloys [25, 40, 126]. Werner [126] further investigated on the influence of strain rate dependent hardening of the aluminum alloy EN AW-6082 on absorbed energy at crash events, showing a negligibly small influence for this alloy. These findings were confirmed for the 6xxx aluminum matrices of TR10 by high speed tensile tests of EN AW-6082T4 specimens at KIT, performed by Reeb³ (see figure 3.8(a)) [80]; the geometry of the specimen is given in the appendix A.3. The

³A. Reeb, Karlsruhe Institute of Technology

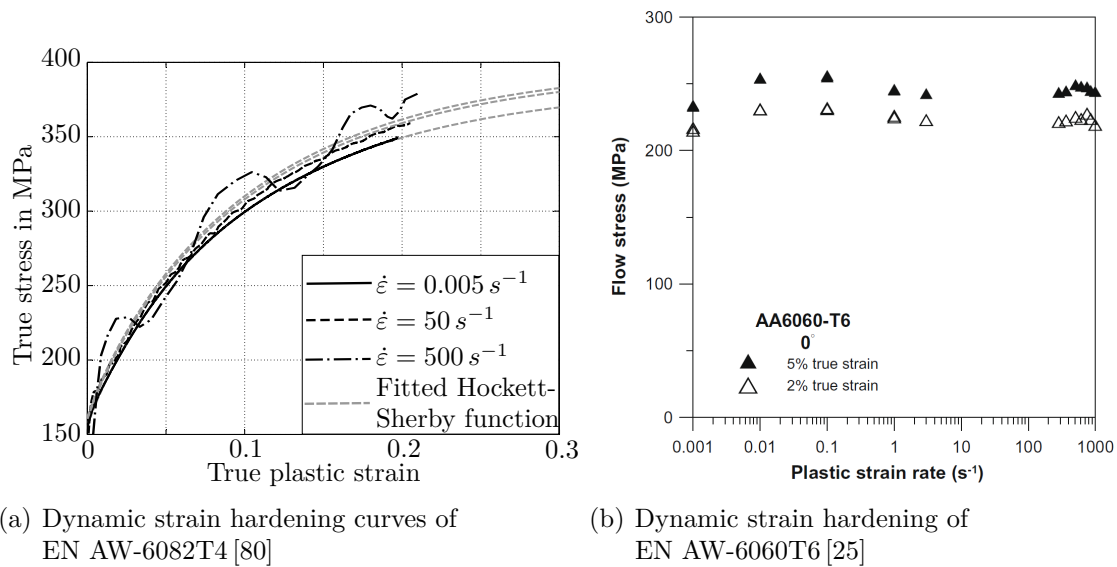


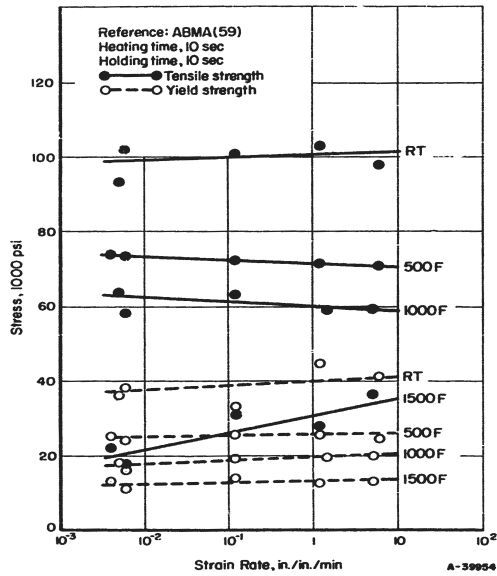
Figure 3.8.: Results of dynamic strain hardening tests of aluminum alloys of group 6xxx

dynamic test data for high strain rates shows typical dynamic oscillations, which are due to the rapid introduction of the tensile force.

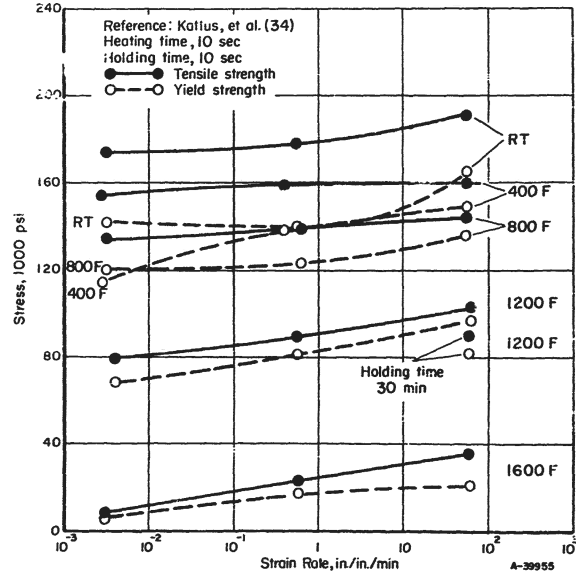
Based on the test data, the strain rate sensitivity exponent m for the model of a constant strain rate sensitivity (equation (3.63)) is calculated. Considering Campbell's results in figure 3.6 an asymptotic increase in strain rate sensitivity (region of damping of dislocation movement) occurs beyond the strain rates which are typical for automotive crash events. For the considered aluminum alloy, experimental results of Chen and Emde [25, 40] confirm, that the region of dislocation damping is beyond the anticipated strain rates.

Figure 3.8(a) shows the experimental results of Reeb and a fitted strain hardening function for the quasistatic tensile test data. This strain hardening function is modified for higher strain rates using the model of constant strain rate sensitivity with a determined sensitivity $m = 0.0035$, leading to the approximated dynamic strain hardening curves. Figure 3.8(b) shows the strain rate dependency of AA 6060T6 for a wide range of strain rates. An increase in flow stress from strain rates of $\dot{\epsilon} = 0.001 \frac{1}{s}$ to $\dot{\epsilon} = 0.1 \frac{1}{s}$ is noticeable, with a decrease for strain rates in the range of $0.1 \frac{1}{s} < \dot{\epsilon} < 400 \frac{1}{s}$, which can be attributed to dynamic strain aging effects as the Portevin–LeChatelier effect [89].

Steel wire The strain rate sensitivity of the high-strength austenitic stainless steel material 1.4310 (SS301) was analyzed quite extensively by the Southern Research Institute in the 1950's [56, 105]. Using specimens from thin sheet material, the material's strain hardening was found to be relatively insensitive towards a variation



(a) Strain rate sensitivity of high-strength austenitic steel 1.4310 (SS301) determined by [105], diagram from [78]



(b) Strain rate sensitivity of high-strength austenitic steel 1.4310 (SS301) determined by [56], diagram from [78]

Figure 3.9.: Experimentally determined strain rate sensitivity of the high-strength austenitic steel 1.4310 (SS301)

Table 3.5.: Sensitivity of the steel wire's UTS towards strain rate

Nominal strain rate $\dot{\epsilon}$ in s^{-1}	0.0001	0.01	0.5
UTS in MPa	2196	2241	2280

in strain rate at room temperature. Their results are shown in figure 3.9.

These findings were confirmed for the here used steel wire based on single-wire tests, however, a determination of the strain rate sensitivity for the whole range of anticipated strain rates ($\dot{\epsilon} \leq 500 s^{-1}$) could not be done, due to the experimental difficulties when testing wire material. Nevertheless, a validation of the strain rate sensitivity as in figure 3.9 is done based on single wire tests for a wide range of strain rates up to $\dot{\epsilon} \leq 0.5 s^{-1}$. The wires were therefore glued into bushings with a free wire length of 30 mm, shown in figure 3.10 With a maximum speed of 1000 mm/min of the tensile testing machine used, the short gage length of the specimens results in a maximum strain rate of $\dot{\epsilon} \approx 0.55 s^{-1}$. Table 3.5 shows the dependence of the UTS on the strain rate.

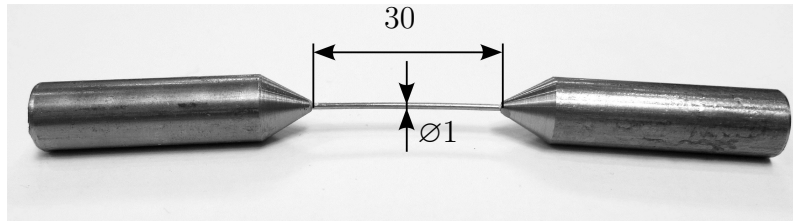


Figure 3.10.: Wire specimen with short gauge length for determination of strain rate dependency

3.3. Properties of the wire-matrix interface

The bonding strength between fiber and matrix is crucial for the mechanical properties of a composite, since mechanical loads are transferred to the reinforcing fiber mainly via interface shear loads. A sufficiently strong interface is desired in order to provide an allow an actual strengthening and stiffening effect of the wires. However, if the interface is overly strong, toughening effects as crack deflection or fiber-pull-out cannot take place [73]. In the following sections, the findings of microstructural evaluations and mechanical testing are presented, which allow for a consideration of interface properties in the further conducted analyses.

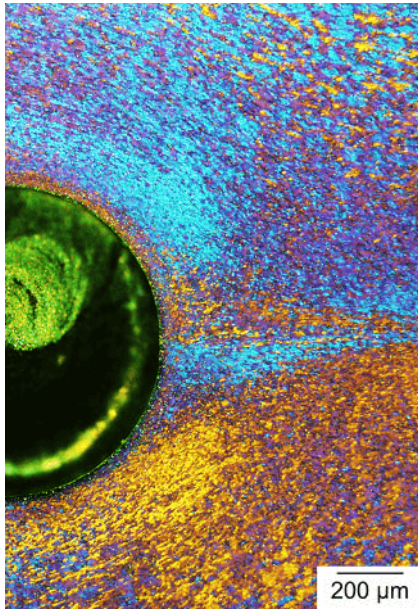
3.3.1. Microstructure of the interface

Weidenmann investigated on the bonding behavior steel fibers in an aluminum matrix of EN AW-6060 [124]. An exemplary micrograph (1.4310 wires in an aluminum matrix of EN AW-6082) is shown in figure 3.11(a), revealing a fine grain formation in the aluminum matrix around the steel wire. This stems from a higher degree of deformation around the wires during extrusion and heterogeneous grain formation during recrystallization, with the steel wires acting as condensation nuclei [81, 124]. The interface is found to be a positive fit free of mesoscopic defects, however, microscopic defects may be present.

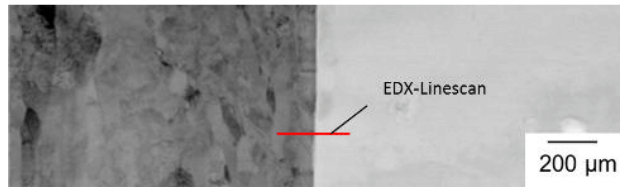
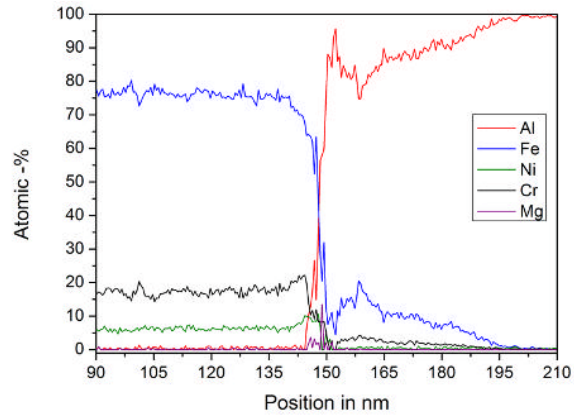
An energy dispersive X-ray spectroscopy (EDX) determined an interdiffusion zone of the elements iron, chromium and nickel in a bonding zone of 5-250 nm for a composite of EN AW-6082+1.4310 [81] and up to 250 nm in a composite of EN-AW6060+1.4310 [124]. Figure 3.11(b) shows the chemical bonding in the vicinity of the wire and gives detailed view of the interface, illustrating the position of the EDX linescan. The lower part is from a transmission electron microscope (TEM), once again showing an interface free of mesoscopic defects.

3.3.2. Experimental determination

Due to the low thickness of the interface layer, the assumption has to be made that only axial shear stresses, hoop shear stresses and normal stresses with respect to the interface layer are transmitted. The experiments determining the interface's shear



(a) Microstructure around the steel wire - Barker-Etching with magnification of 100:1 [81]



(b) TEM image with EDX-linescan across the interface showing the chemical composition of the interface [81]

Figure 3.11.: Microstructure and chemical composition of the matrix-wire interface

and normal strength are described in the following. An assessment of the interface's stiffness is not possible. Since there is no visible sliding between wire and matrix prior to a debonding, it is reasonable to assume a rigid interface.

Assessing the axial shear strength of wire reinforced aluminum matrices, Weidenmann [125] performed push-out tests illustrated in figure 3.12(a). During this test, the reinforcing wire is pushed out of a thin reinforced aluminum plate using a conical indenter. The surrounding matrix is supported in order to minimize bending loads. Force and displacement of the indenter are recorded [71]. The interface's axial shear strength is then calculated as maximum push-out force divided by interface area.

Weidenmann [124] tested the influence of different surface treatments of the steel wire on the interface's shear strength determining strengths ranging from 61 MPa (non-treated steel wire) up to 94 MPa (etched steel wire). The presented SWRA showed an axial interface shear strength evaluated by the push-out test of $\tau_{\max} = 96.1$ MPa [81]. The shear strength of the interface for hoop shear loading was not experimentally assessed and it is assumed that the hoop shear strength equals the axial shear strength.

Reeb performed interface-tensile-tests shown in figure 3.12(b) in order to determine the interface's strength towards normal stress. The tensile specimens were cut by wire eroding with the wire lying in the middle of the gauge length. After fracture, the interface's normal strength is calculated by dividing the maximum force by the area of the fractured surface. The fracture was always located directly at the inter-

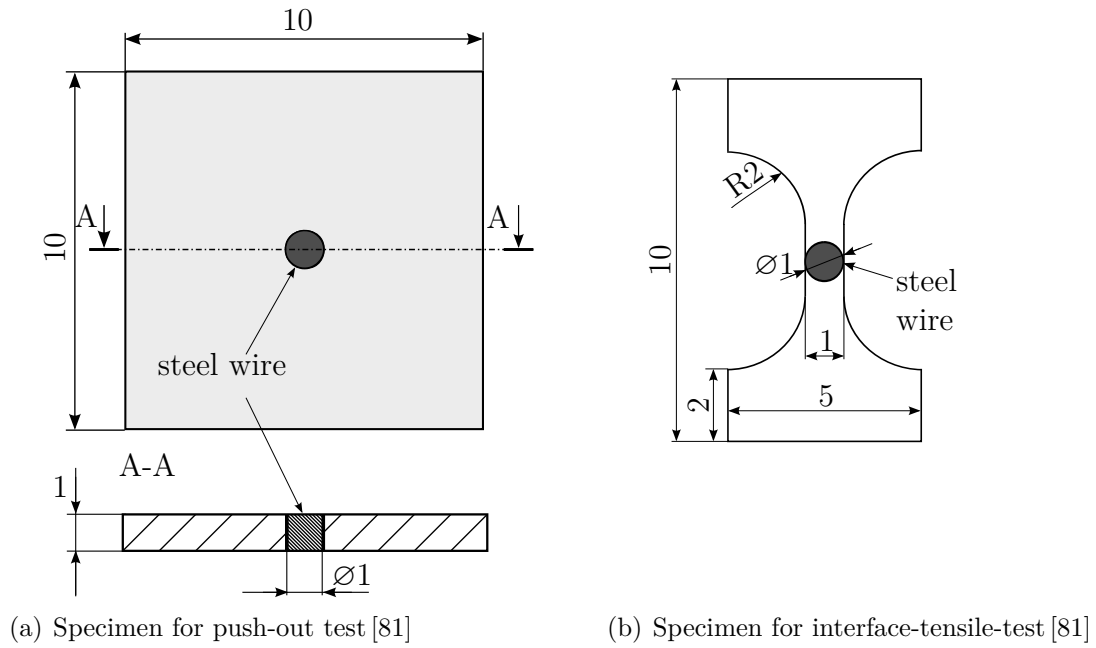


Figure 3.12.: Specimens for determination of axial shear strength and normal strength of the interface

face, hence the area of the fractured surface was equal to the wire's surface [81]. The interface's normal strength was determined to $\sigma_{n_{\max}} = 10.9 \pm 1.25$ MPa. Since the determined strengths are average values over the fractured surface, the maximum interface strengths are likely to be higher [24].

When comparing the interface's normal and shear strength, a significantly higher strength towards axial shear load is striking. This is explained by the simulation of the thermal residual stresses in section 2.3.2, which determines a radial residual stress of up to 70 MPa. Thus, the aluminum matrix compresses radially on the wire, leading to a seemingly increased shear strength by force-closure. The radial expansion of the steel wire, which is caused by the axial push-out force is another minor effect, adding to an additional force-closure.

4. Description of material failure and fracture

Material fracture is well defined as the process of material breakage involving a separation of the material. In contrast to fracture, material failure has many case dependent definitions [4]. It can be defined as the transition from an elastic to a plastic state which is common for structural design tasks. For forming operations, on the contrary, the plastic material state is desirable and the loss of forming capacity is considered as failure. Since crash energy absorbing structures are intended to dissipate the incoming kinetic energy, a loss of energy absorption capacity is considered as failure. This chapter presents the underlying mechanisms of material failure and fracture and further discusses the in this work used phenomenological and physically motivated fracture models.

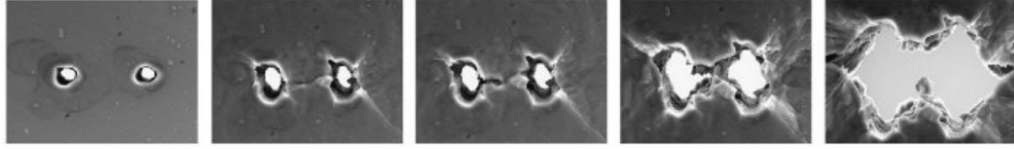
4.1. Mechanisms of material failure and fracture

Closely distinguishing material failure from fracture, no material decohesion develops for failure. The main mechanisms of material failure are a strain localization, which is visible as a ductile necking or as shear bands. Both mechanisms are commonly referred to as “plastic instability” [87] and are considered as precursors to a subsequent fracture process.

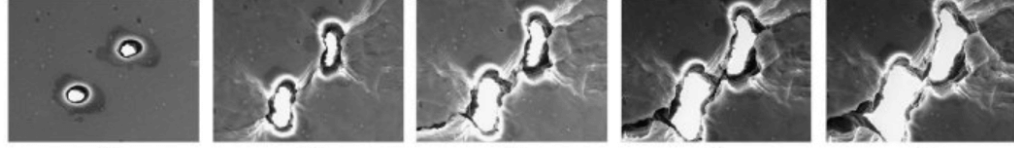
Fracture of ductile materials is linked to the growth and coalescence of inner voids. Voids as inherent material inhomogeneities always exist in non-perfect materials and an additional void nucleation takes place at material inhomogeneities such as inclusions or precipitates. The coagulation of voids is mostly resulting from a necking of the ligament between the voids [16]. This ultimately leads to a macroscopically visible ductile or shear fracture. Figure 4.1 shows the growth and coalescence of two neighboring voids in a series of scanning electron microscope (SEM) images [120].

McClintock [74] and Rice and Tracey [98] first theoretically described the growth of an isolated void in a non-hardening matrix material. It was further shown that the void growth relates to the applied stress state in terms of stress triaxiality η , which is generally defined as

$$\eta = \frac{\sigma_{\text{hyd}}}{\sigma_{\text{eq}}} = \frac{1/3(\sigma_1 + \sigma_2 + \sigma_3)}{1/\sqrt{2}\sqrt{(\sigma_1 - \sigma_2)^2 + (\sigma_2 - \sigma_3)^2 + (\sigma_3 - \sigma_1)^2}} = \frac{I_3}{3\sqrt{3}J_2}, \quad (4.1)$$



(a) Void growth in an aluminum alloy 5052 with the voids oriented 90° to the direction of tension [120]



(b) Void growth in an aluminum alloy 5052 with the voids oriented 45° to the direction of tension [120]

Figure 4.1.: Void growth and coalescence due to ligament necking and shear [120]

where σ_{hyd} is the hydrostatic stress and σ_{eq} is the von Mises equivalent stress.

The stress triaxiality can further be expressed with the third invariant of the stress tensor I_3 and the second invariant of the deviatoric stress tensor J_2 . Consequently, material fracture depends on the stress state and the history of the acting stress states. Based on the theoretical framework of Rice, Tracey and McClintock, Gurson [42] developed a flow function for porous ductile materials. It has been frequently used as a physically motivated fracture model and is employed for this research.

4.2. Modified Gurson yield function for porous ductile media

4.2.1. Theoretical background

Gurson's yield function has undergone many modifications which are presented in this section. In its original form, the yield function is developed based on the analysis of a unit cell of a single spherical void in a rigid-plastic matrix material. The derived yield function is [42]

$$\Phi = \frac{\sigma_{\text{eq}}^2}{\sigma_y^2} + 2f \cosh\left(\frac{\sigma_{\text{hyd}}}{\sigma_y}\right) - 1 - f^2 = 0, \quad (4.2)$$

with the current void volume content f . It should be noted that for $f = 0$, the isotropic von Mises function is recovered.

Tvergaard [111] introduced three constitutive parameters q_1 , q_2 , q_3 in order to improve the prediction for a material behavior of a material with periodically dis-

tributed voids of cylindrical, spherical and circular shape. Based on numerical analyses of a double periodic array of circular cylindrical voids the parameters were identified to match the numerical predictions best with $q_1 = 1.5$, $q_2 = 1$ and $q_3 = q_1^2$.

Since Gurson's model underestimated the evolution of fracture after onset of void coalescence, Tvergaard and Needleman [112] changed the description of void growth by introducing a critical void volume for void coalescence f_C . The deduced model became known as the GTN (Gurson–Tvergaard–Needleman) model and is presented briefly. The following equations are taken from [83, 112] with a unified nomenclature by [67]. The GTN yield function with the constitutive parameters q and a modified void growth f^* is

$$\Phi = \frac{\sigma_{\text{eq}}^2}{\sigma_y^2} + 2q_1 f^* \cosh\left(\frac{3q_2 \sigma_{\text{hyd}}}{2\sigma_y}\right) - 1 - (q_1 f^*)^2 = 0. \quad (4.3)$$

The extended function for void growth now takes a critical void volume f_C into account with a from f_C on changed void evolution by

$$f^*(f) = \begin{cases} f & \text{for } f \leq f_C \\ f_C + \frac{1/q_1 - f_C}{f_F - f_C} (f - f_C) & \text{for } f \geq f_C \end{cases}, \quad (4.4)$$

where f_F and f_C are material parameters and f_F is the void volume fracture for fracture. The present void volume content f increases with the mechanisms of void growth \dot{f}_G and the creation of new voids by nucleation \dot{f}_N ,

$$\dot{f} = \dot{f}_G + \dot{f}_N. \quad (4.5)$$

The growth of voids \dot{f}_G is solely described by the dilatational part of the plastic strain tensor and the current void volume fraction by

$$\dot{f}_G = (1 - f) \dot{\varepsilon}_{\text{kk}}^p. \quad (4.6)$$

A nucleation of voids depends on the plastic equivalent strain and follows a normal distribution by

$$\dot{f}_N = \frac{f_N}{s_N \sqrt{2\pi}} \exp\left(-\frac{1}{2} \left(\frac{\varepsilon_{\text{eq}}^p - \varepsilon_N}{s_N}\right)^2\right) \cdot \dot{\varepsilon}_{\text{eq}}^p. \quad (4.7)$$

ε_N is the mean strain which is necessary for void nucleation, with a corresponding standard deviation s_N . Both parameters are specific for a material and relate to its microstructure and content of void nucleating particles such as inclusions and precipitates.

A closer look at equation (4.6) reveals, that there is no growth of voids without a plastic volume change, i.e. at zero hydrostatic stress. This contradicts with the shown void growth under shear conditions in figure 4.1(b) and with many other experimental surveys (cf. [64, 120, 127]).

Nahshon and Hutchinson [83] proposed an improvement to the void growth func-

tion in order to allow for fracture at shear dominated stress states. The modification of \dot{f}_G alters the void growth only for shear dominated stress states, using the Lode-cosine function $\omega(\boldsymbol{\sigma})$

$$\dot{f}_G = (1 - f) \dot{\epsilon}_{kk}^p + k_\omega \omega(\boldsymbol{\sigma}) f (1 - f) \dot{\epsilon}_{eq}^p \frac{\sigma_y}{\sigma_{eq}}. \quad (4.8)$$

$\omega(\boldsymbol{\sigma})$ is defined as [67]

$$\omega(\boldsymbol{\sigma}) = 1 - \left(\frac{27J_3}{2\sigma_{eq}^3} \right)^2, \quad (4.9)$$

which is $\omega(\boldsymbol{\sigma})=0$ for axisymmetric stress states and $\omega(\boldsymbol{\sigma})=1$ for pure shear stress states plus a hydrostatic stress component. Thus, the GTN model is unaltered for axisymmetric stress states, which it was formulated and calibrated for. k_ω is a calibration constant defining the void growth rate for shear dominated stress states [83].

The shear-modified GTN model proposed by Nahshon and Hutchinson [83] is used as fracture model for the aluminum matrix and the calibration of its parameters is described in the following.

4.2.2. Parameter identification for the shear-modified GTN model for the aluminum matrix

Identifying the nine parameters of the shear-modified GTN model is an error-prone and lengthy process, which asks for a structured approach. Therefore, the parameters are separated into the constitutive parameters q_1, q_2, q_3 , the void growth parameters for axisymmetric stress states $f_0, \epsilon_N, s_N, f_N, f_C, f_F$ and the shear damage parameter k_ω . Good results were reported for a set of constitutive parameters with $q_1 = 1.5$, $q_2 = 1$ and $q_3 = q_1^2$ [60, 65, 107, 112], which are chosen accordingly.

Since the Gurson model is formulated for axisymmetric stress states, the void growth parameters should be determined with cylindrical tensile specimens [83]. This is problematic for sheet material or thin extruded sections with respect to a fabrication of the cylindrical specimens. For this analysis, therefore, the parameters are calibrated with flat tensile specimens shown in figure 4.2, despite of their stress state not being cylindrically axisymmetric.

Once the void growth parameters are found, the shear damage parameter is determined from experiments in pure or simple shear [83]. These stress states are provided for instance by standard tests as Arcan's shear test or Iosipescu's shear test [5, 51]. A drawback of these tests is, that the specimen needs a special testing fixture, making the shear test relatively complex to conduct. Peirs [85] suggested a flat-shear specimen for flat sheet material, which allows testing at stress states close to zero stress triaxiality, using ordinary gripping fixtures. Its geometry was numerically optimized, in order to guarantee low triaxialities until fracture and was successfully employed for thin titanium sheet (0.6 mm, Ti6Al4V). The shear specimen is shown in figure 4.2, with the exact geometry given in appendix A.4. Care

has to be taken, in order to obtain a meaningful set of parameters, since the parameters are non-unique as shown by Zhang [137] and different sets of parameters may lead to the same force-strain result. However, only one set of parameters allows for a physical–microstructural interpretation. A literature survey helps to identify reasonable boundaries for the parameters.

Parameter boundaries from literature Lemaitre [65] gives common ranges for the initial void volume content in metals of $0.001 < f_0 < 0.08$. Micrographical measurements can be used to further assess f_0 [107], however, since the measurements need a high magnification for the detection of small voids at low void contents, the measurement is difficult. The analyses in figure 3.11 do not reveal visual voids at a magnification of 100 times, pointing to a low initial void content; microscopic voids may still be present but cannot be detected at this level of magnification.

A critical void volume content for void coalescence is discussed controversially in the literature. Tvergaard and Needleman [112], who introduced the parameter to Gurson’s model suggest, that $0.15 < f_C < 0.2$. Lemaitre [65] gives a wider range with $0.03 < f_C < 0.15$ and Sun [107] chooses f_C as low as $f_C \approx 0.03$. A reason for these widely different ranges for f_C is given by Zhang [137], who found that f_C depends on the chosen f_0 and vice versa, so that for every chosen f_0 , a corresponding f_C can be found, which will lead to an equal force–strain response of the simulated tensile specimen.

Since fracture is caused by void coalescence, the void volume fraction for final fracture f_F must be bigger than f_C . Having a closer look at the sectionwise–defined equation of void coalescence (equation (4.4)), it is evident that the void content is rapidly rising after reaching the state of void coalescence, which explains a relative insensitivity of final fracture toward f_F . Therefore, $f_F = 0.25$ is often chosen, as initially suggested by [112]. An estimated upper boundary for f_F may be $f_F = 0.36$, which represents the void volume fraction for a “dense random packing of equi-sized spheres” [97, p. 188].

The magnitude of the void nucleation parameters ε_N , s_N and f_N is determined by the microstructure of the material and no common range can be given [65]. These parameters mainly influence the onset and evolution of necking, seen in the uniaxial tensile test [112], which can be used for their assessment. Further, micrographical analyses of the particles which cause a void nucleation give a close estimate for the values f_N and s_N . For the discussed aluminum alloy, these particles are for instance inclusions or precipitates. $f_N \approx 2.5\%$ was estimated based on micrographs [81]. The remaining shear damage parameter lies within the boundaries of $1 < k_\omega < 3$ [83], whereas for $k_\omega = 0$, the unmodified GTN model is obtained [83].

Parameter identification by numerical simulation With the help of the given boundaries, the best fitting parameter values are determined in a fitting process

comparing simulated and experimental stress–strain curves of flat tensile and flat shear specimens. The parameters of void growth are determined solely based on the data of the tensile tests and subsequently, the shear damage parameter is determined with the help of the shear tests. The geometry of the specimens is shown in appendix A.4. An additional difficulty assessing the parameters is a mesh dependency of the fracture model, since a material softening is involved. For the same set of parameters, a small element size leads to an acceleration of softening, whereas a large element size postpones and decelerates the softening. One approach to this problem, followed in this thesis, introduces a characteristic element length for numerical simulation l_c , depending on which the parameters are calibrated. The characteristic element length is defined as:

- 1-D elements: $l_c = l$ (l = element’s length),
- 2-D elements: $l_c = \sqrt{A}$ (A = midsurface area of the element),
- 3-D elements: $l_c = \sqrt[3]{V}$ (V = volume of the element)

As a consequence, the mesh of the fracturing zones in a simulation model must have the same element length. Even though a smaller element size would allow for a closer representation of cracks and crack paths, $l_c = 0.5$ mm was chosen for reasons of numerical efficiency. Figure 4.2 presents the simulation models which are meshed with a characteristic element length $l_c = 0.5$ mm in the fracturing regions.

The simulations were done with LS-DYNA¹ for which the Gurson model is only implemented for an explicit solution scheme. This does not allow for a direct simulation of the slow quasistatic tests, since the small time step of the explicit simulation would lead to unacceptably long calculation times. The simulations were, therefore, carried out at a velocity of $v = 1$ m/s for the tensile test and at $v = 1.33$ m/s for the shear test. With the kinetic energy always staying below 2% of the total energy, no major inertia effects are expected to influence the material’s behavior, so that quasistatic conditions are approximated. However, some dynamic jitter is visible, especially for the shear test data.

Simulated stress–strain curves are overall in good agreement with the experimental ones with respect to stress level, onset of failure and evolution of fracture. Using the best fitting parameters, the stress–strain curve of the tensile test closely follows the experimental data, with minor differences in the fracture evolution. The difference lies within the experimental scatter of five tested specimens.

A bigger deviation of the simulated stress–strain curve is seen for the shear test. Even though an overall good agreement is reached, the simulated strain hardening is below the experimental one. This may be attributed to the orthotropic plastic behavior of the aluminum, not taken into account by the Gurson model which is based on isotropic von Mises plasticity. This explains, why the hardening of the uniaxial tensile test is captured well but the hardening of the flat shear test shows a wider deviation. Another difference is seen in the fracture behavior. Maximum strength and onset of failure and fracture are reproduced closely for both tests, yet,

¹LS-DYNA version 971, revision 6.0.0

Table 4.1.: GTN material fracture parameters for the aluminum matrix for a characteristic finite element length of $l_c = 0.5$ mm (adapted from [81])

Parameter	q_1	q_2	f_0	ε_N	s_N	f_N	f_C	f_F	k_ω
Lower bound	1.0	0.9	0.001	0	0	0	$> f_0 + f_N$	$> f_C$	0
Upper bound	1.5	1.0	0.08	-	-	0.1	0.2	0.25	3.0
Model value-chosen (c) or identified (i)	1.5 (c)	1.0 (c)	0.0033 (i)	0.28 (i)	0.0311 (i)	0.024 (i)	0.032 (i)	0.21 (i)	0.6 (i)

a complete rupture does not set in for the shear test simulation.

It was found that after the deletion of some elements in the fracturing region, the remaining elements become highly distorted and are no longer deleted. Simulations with a smaller element size of $l_c = 0.25$ mm improve this, so that the difference in simulated and experimental fracture is likely to be due to the coarse characteristic element length. However, in favor of lower calculation times, the characteristic element length of 0.5 mm was kept [81]. The identified parameters which led to the best accordance between simulated and experimental data are summed up in table 4.1. Additionally, the findings of the literature survey of reasonable boundaries for the model parameters are added.

4.3. Phenomenological fracture model for the steel wire

Tensile tests of the non-embedded high-strength steel wires show a low engineering fracture strain of $e_{fr} \approx 1.8\%$. Due to the lateral restraint by the aluminum matrix, the low fracture strain is drastically increased by embedding the wire into the aluminum matrix to $e_{fr} > 20\%$ as discussed in section 2.4. A necking and fracture of the wire for uniaxial tension is postponed until necking of the aluminum matrix. For from uniaxial tension different load cases, debonding of the wire occurs at low loads, so that further loads can no longer be introduced into the wire. Therefore, a prevailing uniaxial straining of the wire is expected, allowing for a simple maximum strain fracture criterion.

For this load case, the maximum true fracture strain is calibrated based on the reduction of area of the steel wire

$$\varepsilon_{fr}^p = \ln \left(\frac{A_0}{A_{fr}} \right), \quad (4.10)$$

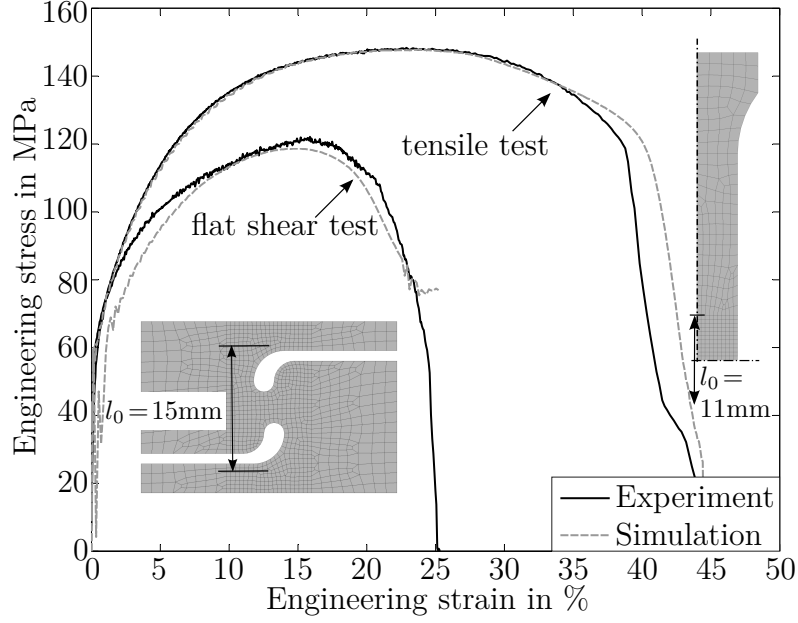


Figure 4.2.: Experimental and simulated stress–strain curves with optimized Gurson material parameters [81], simulated specimens depict the gauge length

with A_0 the initial area of the wire and A_{fr} the minimum area after fracture.

Since there are large differences in the fracture strain of embedded and non-embedded wires, the fracture strain is measured at four tensile specimens of SWRA (see figure 2.6(a)) with two wires each. Using an optical microscope at a magnification of 50 times, first, the diameter of the embedded wire was confirmed to be $d=1$ mm, then the fracture area is measured and the mean fracture strain is assessed as $\varepsilon_{fr}^p \approx 0.7$.

4.4. Failure criterion for the cohesive wire-matrix interface

It was shown that the experimental interface normal strength of SWRA is with $\sigma_n = 10.9 \pm 1.25$ MPa almost one order of magnitude lower than the axial interface shear strength $\tau_{max} = 96.1$ MPa. It is further generally accepted, that a mode I failure due to a normal separation is the most critical fracture mode [103]. Therefore, it seems opportune to use a simple failure criterion for the cohesive interface based on the interface normal stresses only. Once they exceed a failure value, the interface is ought to fail. The applied failure criterion is

$$\sigma_n \leq \sigma_{n_{max}} \quad (4.11)$$

Modeling the interface, cohesive elements² are used, with an elastic cohesive material model³. This model offers a separate definition of the interface’s in-plane stiffness E_T and normal stiffness E_N , as well as a failure stress in terms of a traction, which is defined as force per unit area [67]. In order to block a sliding motion between steel wire and aluminum matrix prior to interface failure, the interface’s stiffness is set to 10 times of the elastic stiffness of the wire to $E_N = E_T = 2 \cdot 10^6$ MPa.

After interface failure at $\sigma_n = \sigma_{n_{max}}$, a frictional contact between wire and matrix is established. This is considered using a segment based erosive contact⁴, which is advantageous over a commonly used node-penalty based contact for edge-to-edge contact problems [66, 67]. The friction coefficients for gliding μ_G and sticking μ_S are taken for the contact pair “mild steel and aluminum” from [18] as $\mu_G = 0.47$ and $\mu_S = 0.61$. Taking post-debonding contact into account is essential, as the wires keep the surrounding aluminum matrix from deforming freely, and affect the stress state in the matrix by transferring compressive loads.

4.5. Validation of the material and fracture model for SWRA

Material and interface models including a fracture description were calibrated for SWRA with tests of each component. It is yet unclear, whether a calibration of material models based on single-component tests is a valid approach. It was shown before, that thermal residual stresses and changed nucleation conditions in the vicinity of the wire change the properties of aluminum matrix and steel wire. Whether the change is of negligible magnitude is evaluated in the following.

A validation of the proposed modeling technique is done based on tensile test data in and perpendicular to the wire direction with the specimens shown in figure 2.6(a). The arising global strains are recorded with the optical measurement system GOM Aramis and the global stresses are calculated as measured force divided by total area of the specimen. They do not represent the actual stress in wire or matrix, since the material is inhomogeneous. The calculated stresses present a mere quantity for comparison between specimens of slightly different cross sectional areas and allow for a comparison to the non-reinforced aluminum matrix.

4.5.1. Tension of SWRA in wire direction

As first validating scenario, the tensile test in wire direction is simulated. Therefore, a symmetrical model of the tensile specimen is created. The reference length for evaluation of the strains is $l_0 = 15$ mm for experiment and simulation. An imperfection, which triggers a symmetrical necking of matrix and wire is introduced

²LS-DYNA ELFORM19 - four point, eight node cohesive element

³*MAT_COHESIVE_ELASTIC

⁴*CONTACT_ERODING_SINGLE_SURFACE

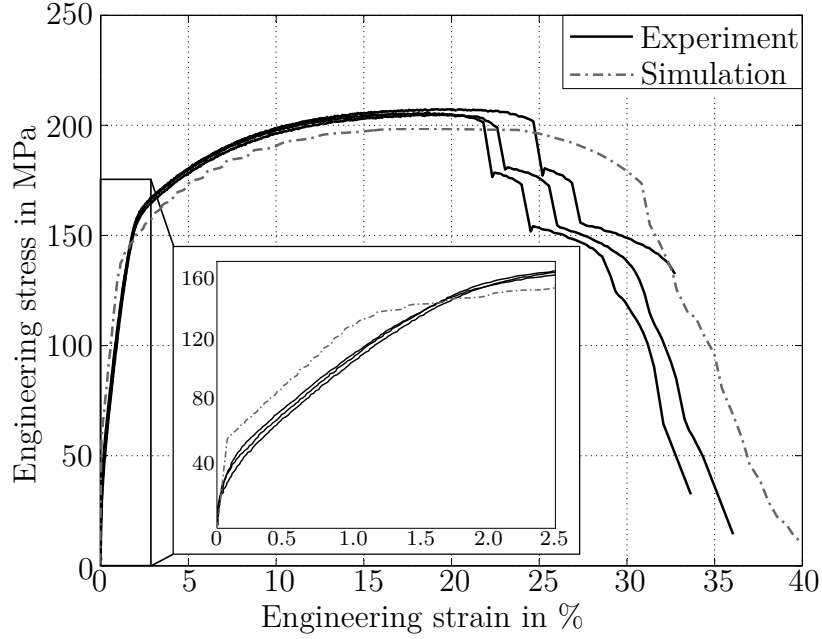


Figure 4.3.: Experimental and simulated stress–strain curves for SWRA with tension in wire direction

as reduction of the wire’s radius of $r_{\text{w,red}} = 0.998 \cdot r_{\text{w}}$ and of the matrix’s width of $w_{\text{m,red}} = 0.998 \cdot w_{\text{m}}$. The explicit simulations are carried out with a tensile speed of $v = 2 \frac{\text{m}}{\text{s}}$, which leads to some dynamic jitter in the simulated data. The kinetic energy, here, is in all cases well below 2% of the total energy and no major inertia effects impair the simulation results.

A simulated stress–strain curve for a normal interface strength of $\sigma_{\text{n,max}} = 11 \text{ MPa}$ and a wire fracture strain of $\varepsilon_{\text{fr}}^{\text{p}} = 0.7$ is compared to three experimental stress–strain curves in figure 4.3. The simulated stress curve is smoothed with a three-point moving average filter in order to reduce noise from dynamic jitter. Differences between simulated and experimental data are discussed in the following.

Differences in the elastic and elasto-plastic regime ($e < 2\%$)

The simulation captures the three characteristic elasto-plastic regions of SWRA. Wire and matrix initially both deform elastically. This is followed by a region, where the wire still behaves elastically and the matrix starts plastifying. In the third region, wire and matrix both deform plastically. The initial material stiffness agrees well with the experimental data, however, the strength in the second region is overpredicted. This is explained by thermal residual stresses in the experimental specimens, which are not considered by the simulation.

Differences in the plastic part ($2\% < e < 20\%$)

Since the residual stresses are released when both matrix and wire deform plastically, they cannot explain the differences in stress level of about 5%. Two possible causes for the varying stress levels can be given. It is possible, that the extrapolation of the matrix's strain hardening is too soft. However, the strain level for the reinforced specimens does not significantly exceed the range of identified strain hardening data, which makes this reason unlikely. It further does not explain the difference between simulated and experimental stress level at the early stage of plastification with low plastic strains.

It is more probable that the strain hardening of matrix or wire is changed during the fabrication process of SWRA. A finer grain size of the matrix around the reinforcing wire as discussed in section 2.3 leads to this higher strain hardening (Hall–Petch relation). A higher strain hardening of the wire due to the extrusion process was excluded by Weidenmann [124].

Differences in failure evolution and fracture ($20\% < e$)

Examining the experimental tensile test, failure starts with a ductile necking process of the aluminum matrix, which is at about the same ultimate strain as in the non-reinforced matrix. This is followed by a visible drop in the force level, due to a rupture of one wire. The load is then redistributed to the remaining wire and matrix. A second wire fractures is detectable as a second drop in the force level. In a final step, the matrix fractures.

The onset of necking is captured well, the speed of the evolution of failure and fracture is underestimated. It was shown, that a necking process of the wire with a subsequent fracture is postponed until an onset of necking in the aluminum matrix [81]. Experiments further show, that at the moment of the distinct drop in the force level, the matrix does not yet fracture. It can be concluded, that the wire necks and fractures rapidly, right after the supporting interface is destroyed due to the necking of the matrix. This necking process with fracture after a failure of the interface is accelerated due to the fact, that the wire can only sustain the high strains by the radially supporting effect of the wire-matrix interface. A high void content before onset of necking is likely to be present in the wire, since it is strained well beyond its uniaxial fracture strain in the non-embedded state. An in-situ monitoring of the wire's necking behavior in SWRA with computer tomography could proof this, however, this was not done so far.

With the used symmetric simulation model which only possesses one steel wire, only one wire fracture is visible.

4.5.2. Tension of SWRA perpendicular to wire direction

Testing SWRA at tension perpendicular to wire direction, the behavior of the specimens is dominated by the aluminum matrix and the wire-matrix interface. The

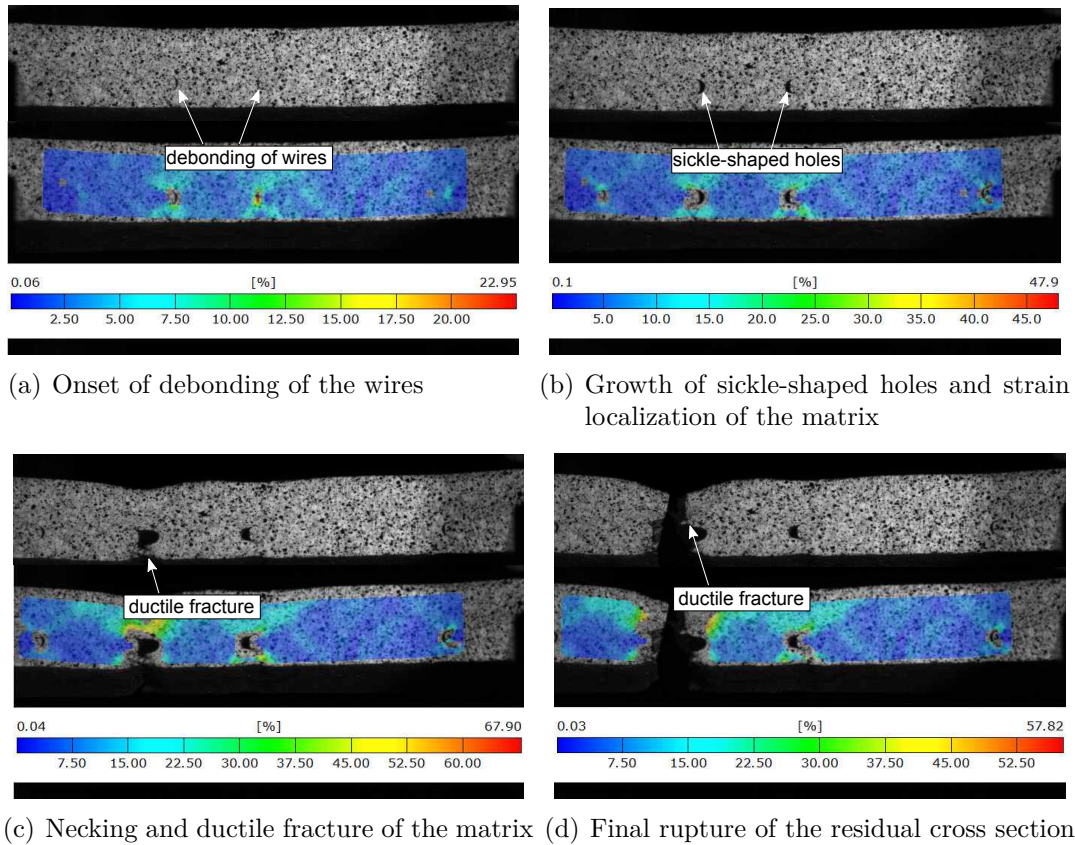


Figure 4.4.: Wire debonding and evolution of failure and fracture in SWRA at tension perpendicular to wire direction, the plots show the equivalent strain

high strain hardening of the wire cannot be made use of, since loads are mainly introduced as interface shear loads via a relatively weak interface and contact. This test, therefore, excludes influences by the material fracture of the steel wire and carves out matrix and interface properties.

For the experimental evaluation, specimens with a geometry as shown in figure 2.6(a) are tested. The elongation is measured for a gauge length of 6 mm with an optical measurement system, which surveils the side of the specimen showing the wire-matrix interface. Thus, the instant of interface failure is detected, as shown in the series of pictures in figure 4.4. Global strains are calculated for a comparison with non-reinforced aluminum.

In comparison to the aluminum matrix, the wire has a three-times higher Young's modulus and a much higher yield strength. The forces that are transferred before interface failure are not sufficient to cause plastic yielding of the wires. The wires behave elastically and the matrix is plastifying so that the interface stresses are mostly defined by the matrix's strain hardening properties. If the wire is regarded as a non-deformable rigid body, the maximum interface normal stresses directly relate to the matrix's strain hardening [81]. An early failure of the interface is, therefore, an-

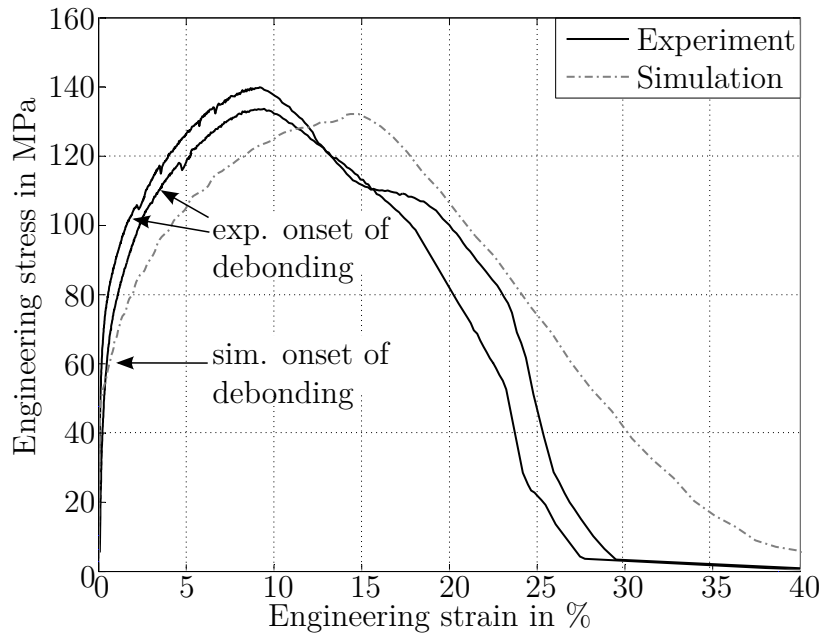


Figure 4.5.: Experimental and simulated stress–strain curves for SWRA with tension perpendicular to wire direction

ticipated. This occurs at a stress level (=force divided by total specimen area) of $s = 60$ MPa, whereas the experimentally determined interface failure starts at higher stress levels of $100 < s < 120$ MPa. After decohesion of the wire, sickle-shaped voids form around the wire, promoting fracture of the aluminum matrix.

The simulation agrees in terms of maximum load, position of fracture and fracture evolution. The differences between simulation and experiment are mostly in the pre-fracture regime and may be attributed to a plastic orthotropy of the aluminum matrix, not being considered by the isotropic Gurson model. Differences in the onset of debonding cannot only be explained by an underestimated interface normal strength, as a debonding at this high load would require an interface normal strength of $\sigma_{n_{\max}} > 250$ MPa (later discussed in section 4.6). More likely is an influence of the grain refinement of the matrix around the wire, which offers a higher strain hardening than the surrounding matrix material, thus lowering the interface normal stresses and postponing debonding. A radial compression from residual thermal stresses also adds to an increase in debonding strength.

4.6. Sensitivity analyses of the fracture model of SWRA

As shown in the previous section, assessing a material model for SWRA based on the characterization of its constituents gives a reasonably well description of the material's behavior. This was proven for two distinct load cases of tension in wire direction and tension perpendicular to wire directions. A tension in wire

direction presents a “best case” scenario exploiting best the wire’s high strength; tension perpendicular to wire direction is the “worst case” scenario, showing an early debonding which significantly weakens the composite. In order to gain deeper insight into the failure and fracture behavior of SWRA, sensitivity analyses are carried out, determining the material’s sensitivity toward interface normal strength and fracture strain of the wire.

4.6.1. Sensitivity toward interface normal strength

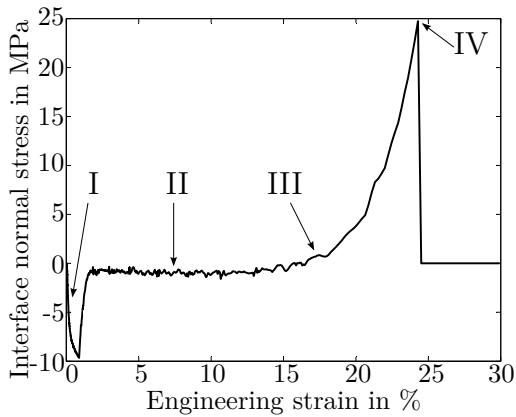
Figure 4.7(a) shows the variation of the stress–strain curve for tension in wire direction with interface normal strengths $\sigma_{n_{\max}} = 2.75, 11, 55, 110, 330$ MPa. The wire’s fracture strain is kept constant at $\varepsilon_{fr}^p = 0.7$.

For tension in wire direction, the material responds relatively insensitive to a change in interface normal strength. Only for the lowest strength of $\sigma_{n_{\max}} = 2.75$ MPa, an immediate debonding of the wire leads to an early fracture of wire and composite. Increasing the interface normal strength, even up to a high strength of $\sigma_{n_{\max}} = 330$ MPa, does not significantly postpone fracture. The interface is intact until matrix fracture, which is enforced by the matrix’s rigid connection to the steel wire.

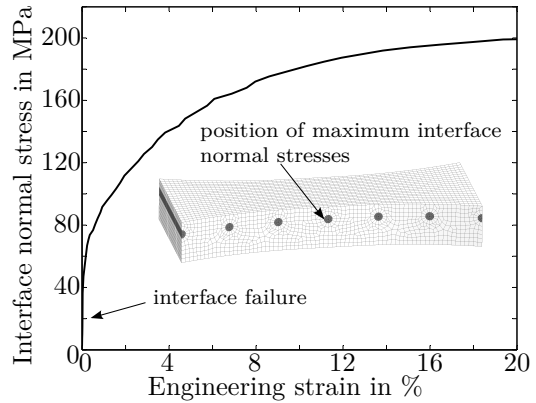
At tension perpendicular to the wire direction, the wire’s fracture strain does not play a role, since the wire stays in the elastic regime throughout the whole test. It can be seen from figure 4.7(c), that up to an interface normal strength of $\sigma_{n_{\max}} = 110$ MPa, the changes of the material’s behavior are negligible. The onset of debonding is slightly shifted to higher loads, however, for the sake of clarity, only one representative curve is drawn for $\sigma_{n_{\max}} = 2.75$ to 110 MPa. Further increasing the interface normal strength to $\sigma_{n_{\max}} = 220$ MPa shifts the onset of debonding noticeably. At $\sigma_{n_{\max}} = 330$ MPa, a debonding of the wire does no longer occur and an actual strengthening of the aluminum matrix is reached. These high interface strengths, however, are more than 20 times higher than the currently reached strengths and an improvement of this order of magnitude is improbable.

In order to clarify the low sensitivity of SWRA toward the interface normal strength, the interface normal stress was analyzed for tension in wire direction and perpendicular to wire direction [81]. For tension in wire direction, four regions are distinguished (see figure 4.6(a)):

- Region I: wire and matrix both deform elastically. Due to a higher Poissons’s ratio of the aluminum matrix, the interface bears compression stresses
- Region II: wire and matrix both deform plastically with a plastic Poisson’s ratio of 0.5. Therefore, the normal stresses at the interface are close to zero
- Region III: onset of necking in the aluminum matrix leads to a quickly rising interface normal stress
- Region IV: the normal stress reaches the interface’s normal strength, the interface fails and the wire debonds.



(a) Development of interface normal stress for tension in wire direction, shown for an interface normal strength of $\sigma_{n_{\max}} = 25$ MPa [81]



(b) Development of maximum interface normal stress for tension perpendicular to wire direction [81]

Figure 4.6.: Development of interface normal stress for tension in and perpendicular to wire direction

As the interface normal stresses quickly rise due to necking in the aluminum matrix, increasing the interface's normal strength has a limited effect on the composite's fracture behavior. Both analyses with tension in and perpendicular to the wire direction show, that even a significantly increased interface strength cannot alter the composite's fracture behavior substantially.

4.6.2. Sensitivity toward the wire's fracture strain

In addition to the investigations focusing on the interface normal strength, the fracture strain of the steel wire was varied from $\varepsilon_{fr}^p = 0.2$ to $\varepsilon_{fr}^p = 1$, leading to a pronounced change in the composites fracture behavior. The interface normal strength was kept at $\sigma_{n_{\max}} = 11$ MPa. For the lowest fracture strain, wire fracture sets in before the aluminum matrix starts to neck. This is a non-physical behavior, since necking of the matrix is a necessary condition for failure of the interface, which in turn allows for the wire to neck. The highest simulated fracture strain $\varepsilon_{fr}^p = 1$ showed an onset of matrix fracture prior to fracture of the wire, which was not observed in the experiments. Even higher fracture strains cannot increase the composite's overall fracture strain, since the matrix already starts fracturing prior to wire fracture for $\varepsilon_{fr}^p = 1$.

The experimental data indicates, that shortly after onset of necking of the aluminum matrix, the wires fracture. Lower simulated fracture strains of the wire than the measured of $\varepsilon_{fr}^p = 0.7$ lead to an earlier wire fracture, however, the rapid necking process of the wire cannot be modeled by only reducing the fracture strain. As discussed, the wire is likely to be pre-damaged, since the high strains can only be sustained due to the radial support, which does not allow for necking. After debon-

ding of the wire, the necking process of the wire is accelerated by the pre-damage. This behavior is simulated best with a damage model including material softening.

The model used in this thesis considers pre-damage by inherent voids as growth of a void area A_{void} , increasing the stress in the remaining wire material by material by

$$\sigma = \frac{F}{A - A_{\text{void}}}. \quad (4.12)$$

The void area grows according to

$$A_{\text{void}} = D \cdot A = \frac{\varepsilon_{\text{eq}}^{\text{p}} - \varepsilon_{\text{fail}}^{\text{p}}}{\varepsilon_{\text{fr}}^{\text{p}} - \varepsilon_{\text{fail}}^{\text{p}}} \cdot A \text{ with } \varepsilon_{\text{fail}}^{\text{p}} \leq \varepsilon_{\text{eq}}^{\text{p}} \leq \varepsilon_{\text{fr}}^{\text{p}}. \quad (4.13)$$

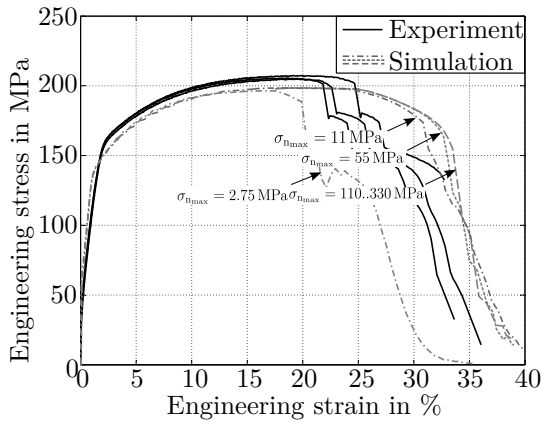
D is the damage parameter with $0 \leq \omega \leq 1$, which is defined by the failure strain $\varepsilon_{\text{fail}}^{\text{p}}$ for onset of softening and $\varepsilon_{\text{frac}}^{\text{p}}$ for end of softening at material fracture [67]. A good matching softening curve is reached with $\varepsilon_{\text{fail}}^{\text{p}} = 0.23$ and $\varepsilon_{\text{fr}}^{\text{p}} = 0.5$ [106], shown in figure 4.7(b) as “ $\varepsilon_{\text{fail}} = 0.23$, soft”.

4.7. Summary and discussion of the material model for SWRA

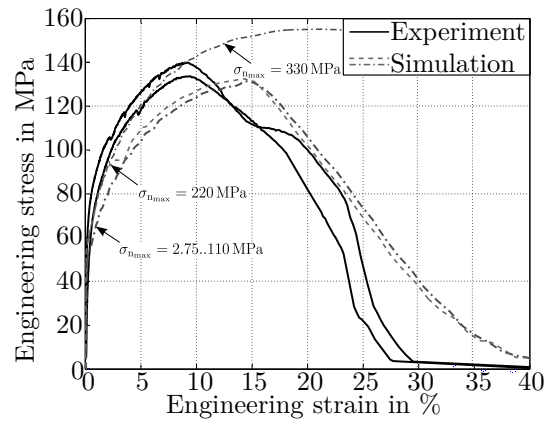
A material model for SWRA including fracture is presented based on the shear modified GTN model for the aluminum matrix and an isotropic von Mises material with a phenomenological maximum strain fracture criterion with softening option for the wire. As the process of material failure is triggered by a debonding of the wires, a cohesive model for the interface is applied and its parameters are experimentally determined.

Comparing simulated predictions and experimental results of uniaxial tensile specimens of SWRA in and perpendicular to the wire direction, simulated and experimental data agree well. It can be concluded, that separately characterising the mechanical properties of steel wire and aluminum matrix and combining the so found material models to a description of SWRA is a valid approach. Differences in simulated and experimental data in the pre-fracture region are mainly attributed to an orthotropic plastic behavior of the aluminum matrix, which is not considered by the isotropic shear modified GTN model. An improvement could be reached by coupling an orthotropic yield function to a Gurson like fracture description of void growth as suggested by Schmeing [101].

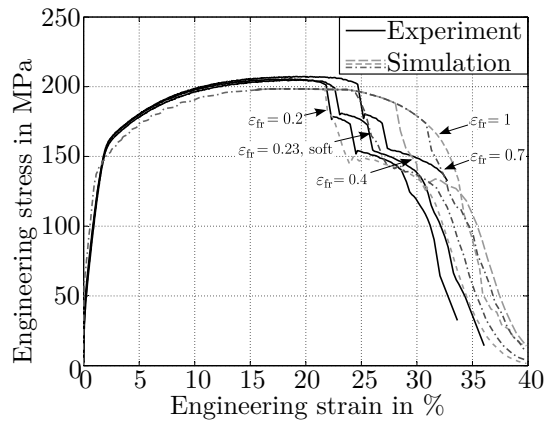
Further differences in the fracture behavior are related to the wire’s fracture criterion based on a maximum strain criterion, which does not account for possible void growth and pre-damage in the radially supported wire, prior to interface failure. The wire’s necking behavior seems to be accelerated by pre-damage, however, this needs to be further verified, for instance by in-situ computer tomography tensile tests. A



(a) Sensitivity of SWRA toward interface normal strength at tension in wire direction



(b) Sensitivity of SWRA toward interface normal strength at tension perpendicular to wire direction



(c) Sensitivity of SWRA toward the wire's fracture strain at an interface normal strength of $\sigma_{n_{max}} = 11$ MPa

Figure 4.7.: Sensitivity of SWRA with respect to the interface's normal strength of the wire-matrix interface and to the wire's fracture strain

modified maximum strain criterion including material softening after necking is able to give a closer prediction of material failure.

Sensitivity analyses of SWRA toward interface normal strength and wire fracture strain elucidate the influence of wire debonding, which accelerates the fracture process of the composite. Due to the acting mechanisms, neither a major increase in interface normal strength, nor an increase in the wire's fracture strain can significantly postpone the fracture of the composite. Based on these findings, tension in wire direction is a "best case" load scenario for SWRA, which offers the highest capacity of energy absorption. Yet, compared to the non-reinforced aluminum matrix, SWRA does not offer a significantly better performance at quasistatic conditions (see also table 2.3).

5. Performance of SWRA in structural components undergoing high deformations and impact loads

Previously presented investigations had well-defined load cases and a foreseeable fracture behavior. Good agreement between simulation and experiment is also due to the fact, that the material and fracture model is calibrated with load cases similar to the simulated ones. The validity of the presented material model is, thus, not generally given.

In this chapter, a further validation of the material model for complex load scenarios of structural components is performed. This is done with bolt-pull-out tests, which present a fracture scenario at a bolt-connection. Aside from the aspect of validation, the test allows for a comparison of SWRA and non-reinforced aluminum for pin-joint connections and assesses fracture process and crack propagation in the reinforced aluminum. With the validated material model, two crash energy absorbing structures are analyzed by means of simulation and experiments.

The first example is a dynamic axial crushing of an extruded crash tube, which would be employed in the crumple-zone of a car as shown in figure 1.1(a), absorbing crash energy for a front impact. The second example is a dynamic three-point bending of a reinforced section, which is taken as an abstraction of a side-impact load case at the B-pillar or the side sill impacting a pole. The simulated results are confirmed by dynamic three-point bending tests in a drop tower.

5.1. Validation of the simulation methodology on structural level with bolt-pull-out tests

Aiming at a comprehensive validation of the suggested material modeling methodology, the bolt-pull-out test is suggested. In contrast to the tensile tests, the fracture behavior is less foreseeable, the stress state less uniform and multiaxial. A scheme of the test setup is shown in figure 5.1(b) and the simulation model for a bolt-pull-out in SWRA is shown in figure 5.1(c). As for the simulation of the tensile tests, the element length is kept close to $l_c = 0.5$ mm, in order to meet the element length for which the shear modified GTN model was calibrated for.

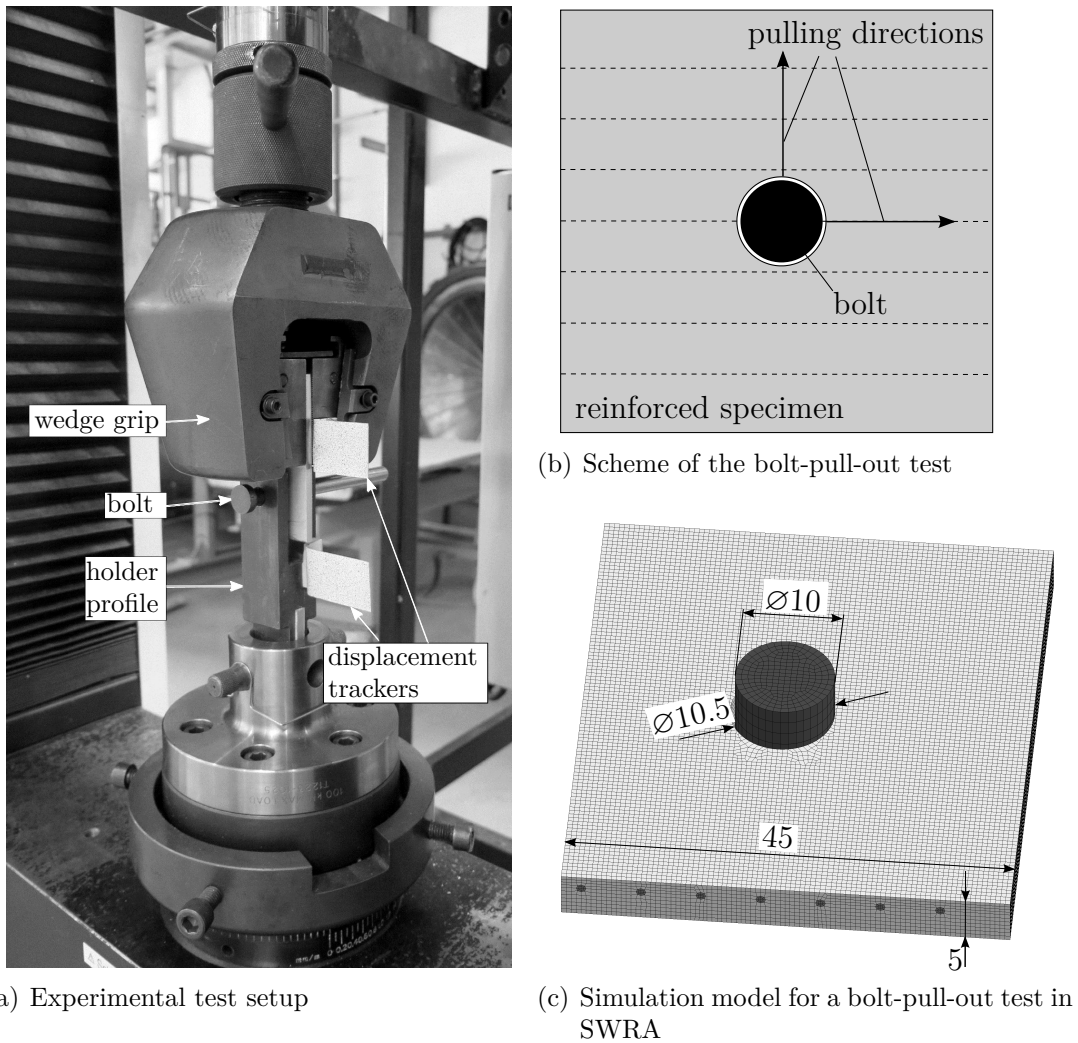


Figure 5.1.: Bolt-pull-out test and corresponding simulation model [81]

The tests are performed for SWRA in the direction of and perpendicular to the reinforcement direction, as well as for non-reinforced aluminum in extrusion direction. The specimens are all cut from the same extruded sections as shown in figure 1.2(b) by waterjet cutting. A hardened, high-strength steel bolt with a diameter of 10 mm is inserted in the hole and pulled through the specimen until final fracture. For the sake of an easy experimentation, the hole is slightly oversized with a diameter of 10.5 mm. The specimens are clamped on one side using wedge gripping jaws and the bolt is held in a stiff holder profile.

Only a short gripping length of 5 mm could be realized for tests perpendicular to wire direction. This led to a noticeable rotation and sliding of the gripping jaws. However, the specimens were tightly gripped until final fracture. A correction of the tensile test data is done by recording the sliding motion of the gripping jaws and the deformation of the testing machine. The here presented bolt displacement

is a relative displacement between two measuring points, one mounted alongside the upper grip jaw, the other mounted on the stiff fork which holds the bolt. The experimental setup is shown in figure 5.1(a).

5.1.1. Bolt-pull-out in the non-reinforced aluminum matrix

Four non-reinforced specimens were tested in extrusion direction, showing two distinct fracture modes presented in figures 5.2(a), 5.2(b). All specimens neck in tension in the side flank, with the neck developing into a ductile crack as in figure 5.2(a) for one of four specimens. For two specimens, the by necking initiated crack turns into the direction of pull-out, which results in a shear fracture. One specimen fractured exclusively in a shear-out fracture type. A high plastic deformation of the front edge is evident as orange-peel effect.

The simulation predicts the experimentally observed initial ductile failure in the side flank at the right position. This is followed by a crack which grows in the direction of maximum shear with a sudden shear-out fracture. Using a symmetric simulation model, the unsymmetric fracture mode of figure 5.2(a) cannot be reproduced. Comparing the evolution of the shear crack, the simulation does not capture the sharp crack parallel to pull-out direction. This is due to a mesh dependency of the crack evolution, which can hardly be avoided at the chosen element size.

Comparing simulated and experimental curves of force versus bolt displacement in figure 5.3(a), several differences can be noticed. The initial slope of the force is stiffer in the simulation, which is most likely due to a deformation of steel bolt and holder profile, not being compensated by the experimental measurements. The force level in the pre-fracturing regime is overall lower than the three experimental curves, which was already observed at the reinforced tensile specimens. This can be attributed to an age hardening of the aluminum matrix given the time between the experimental material characterization (November 2013) and the bolt-pull-out tests (July 2014). This was confirmed by layered-compression tests in July 2015 (see appendix A.5), revealing a significant amount of age hardening. A further source for the discrepancy in the simulation model is the inherent plastic orthotropy in the aluminum matrix. Onset of fracture, evolution of fracture and final rupture are predicted satisfactory.

5.1.2. Bolt-pull-out in SWRA in wire direction

For a bolt-pull-out in wire direction, SWRA exhibits a quite similar fracture as the non-reinforced aluminum matrix, as shown in figure 5.2(f). An initial neck develops in the tension regime, however, an initiated ductile crack perpendicular to the pulling direction is stopped as it reaches the first reinforcing wire. This shows a crack arresting property of the wire reinforcement. A subsequent shear fracture develops quite analogous to the non-reinforced aluminum. The crack evolution is along the wire-matrix interface and is accelerated by it, as the interface is the weakest link in the composite.

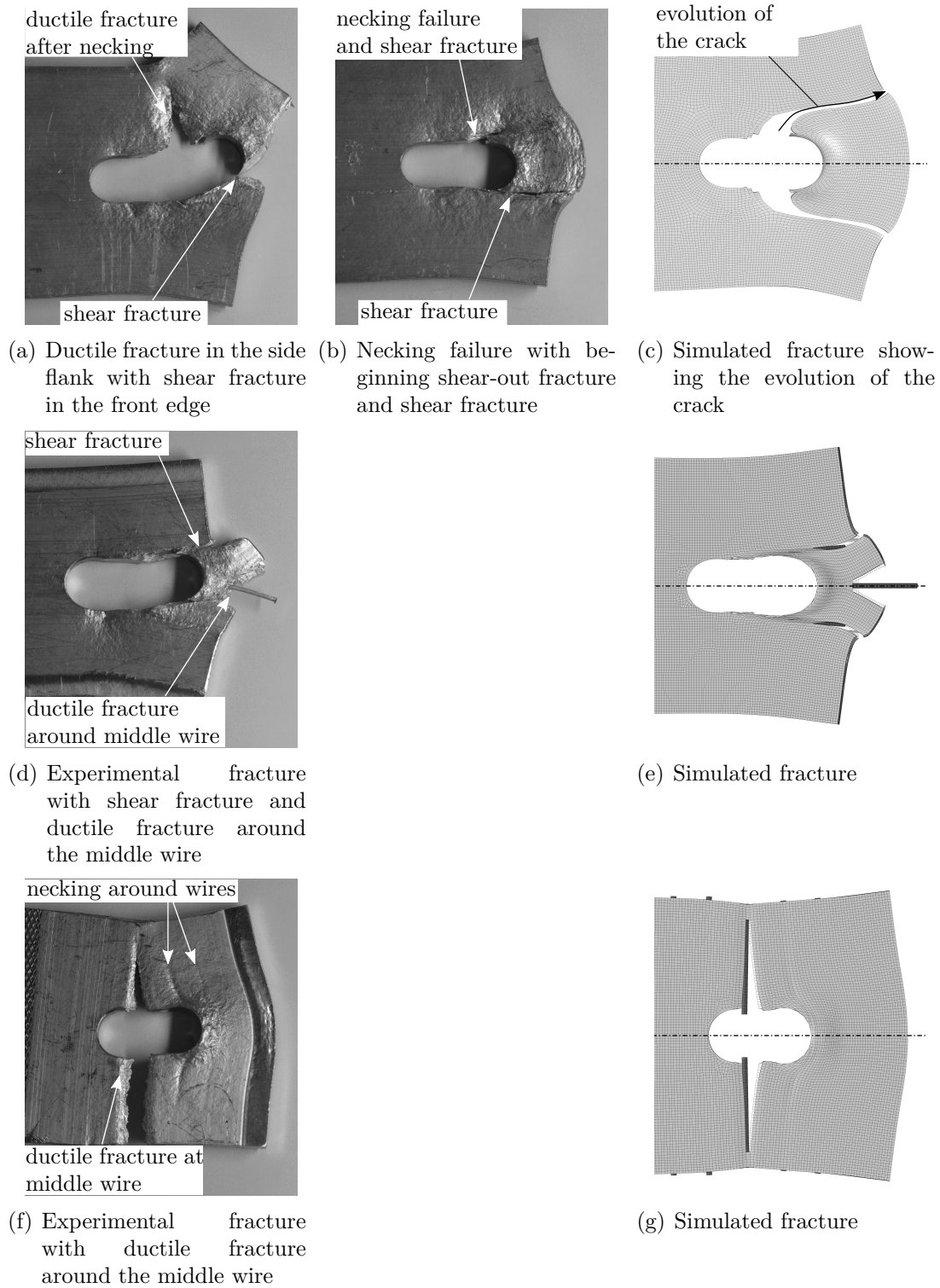
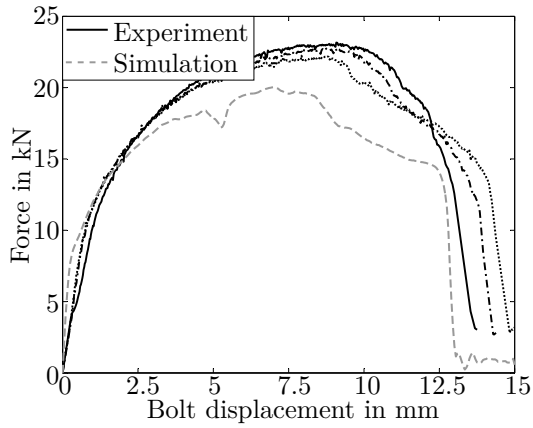
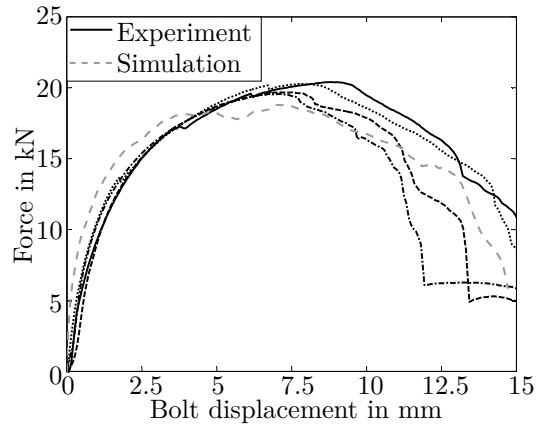


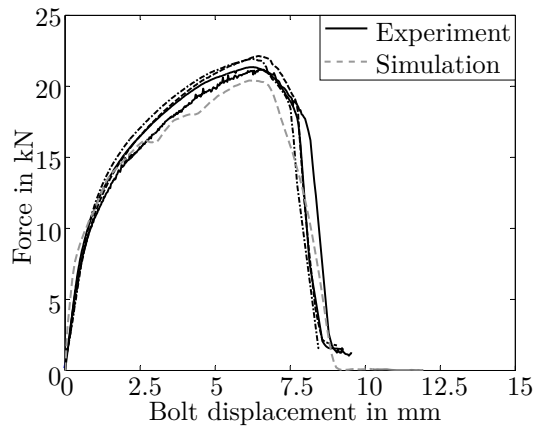
Figure 5.2.: Experimental and simulated bolt-pull-out fracture modes for non-reinforced aluminum (a, b, c), SWRA in wire direction (d, e) and perpendicular to wire direction (f, g) [81]



(a) Force versus bolt-displacement curve for non-reinforced aluminum



(b) Force versus bolt-displacement curve for reinforced aluminum with pull-out in wire direction



(c) Force versus bolt-displacement curve for reinforced aluminum with pull-out perpendicular to wire direction

Figure 5.3.: Experimental and simulated force versus bolt-displacement curves [81]

A wire-matrix debonding results in a lower maximum force and the accelerated crack evolution in a lower fracture resistance. A second crack is due to a debonding of the middle wire and a growth of the created void in tension perpendicular to the middle wire. After total fracture of the specimen, the bolt is pulled through and the frictional contact results in a plateau formation of the pull-out force. Simulated and experimental fracture prediction in figure 5.2 show a very good agreement, as well as simulated and experimental force versus bolt-displacement curve in figure 5.3(b), falling within the experimental scatter of four tested specimens.

5.1.3. Bolt-pull-out in SWRA perpendicular to wire direction

Pulling the bolt perpendicular to the wire direction causes a fracture in the side flank of the specimen. The wire in the tensile stressed region debonds from the matrix and a void is created. The remaining cross section of the aluminum matrix fractures after a necking process, with a crack running along the debonded interface. Final fracture occurs at a much lower bolt displacement with a sudden rupture of one side flank. In addition to this crack, the aluminum matrix necks at the positions of the reinforcing wires, which is due to the non-homogeneous stiffness distribution and a debonding of the wires.

A curiosity is found with SWRA showing a higher maximum force for pull-out perpendicular to wire direction, than in wire direction. This can be explained by assuming that a total debonding of the wires for both tests, in and perpendicular to wire direction occurs. The critical remaining aluminum cross section, which has to withstand the pull-out load is equal for both load cases. For a pull-out in wire direction, the remaining cross section is mainly loaded in shear, whereas for pull-out perpendicular to the wire direction, the prevailing load is tension. The matrix's higher strength in tension compared to its shear resistance (see figure 4.2) explains the higher maximum force for a bolt-pull out perpendicular to the wire direction.

5.1.4. Summary and discussion of the bolt-pull-out test results

The bolt-pull-out in aluminum and SWRA leads to ambiguous results. Compared to non-reinforced aluminum, SWRA exhibits a maximum force which is 5% (pull-out perpendicular to wire direction) up to 13% lower (reinforcement in pull-out direction). For a reinforcement in pull-out direction, a crack arresting behavior was determined and the evolution of fracture is slower than in non-reinforced aluminum. For a reinforcement perpendicular to wire direction, a crack stimulating effect of the wire-matrix debonding is evident, with a sudden rupture of the specimen after the peak force.

Based on these findings, an increase in fracture toughness for pin-joint connections might be reached by reinforcing aluminum in a suitable way. Even though the aluminum matrix was weakened by a wire reinforcement, the results of the pull-out tests in wire direction points to an increased fracture toughness. An optimized positioning of the wires still offers further improvement. With respect to the capacity

of energy absorption, no significant benefits are found for reinforcement in pull-out direction, yet, a decrease for a reinforcement perpendicular to pull out direction is evident.

Based on the consistently good agreement between simulation and experiment of SWRA at two complex load and fracture scenarios, the modeling technique, as well as the material and fracture model is confirmed as valid. Differences in the simulated force level at non-reinforced aluminum mainly are mainly attributed to an age hardening of the aluminum matrix during the time between material characterization and bolt-pull-out testing. Plastic orthotropy of the aluminum matrix is one further cause of the differences and currently cannot be considered by the shear modified GTN model.

5.2. Axial crushing of extruded non-reinforced and steel-wire-reinforced aluminum crash tubes

An example for a crash-loaded structure made from SWRA is an axial crash tube. Prior to discussing the use of a steel wire reinforcement, a short theory on axial crash tubes is given.

5.2.1. Design constraints for axial crash tubes

Crash tubes in the front crumple-zone of a car are designed and used to absorb kinetic energy at frontal impacts. A progressive buckling mode (see figure 1.1(b)) developing in the crash tube converts the kinetic energy into plastic strain energy. In order for the progressive buckling to set in, the slenderness ratio must be chosen low enough to avoid a global buckling. For a global buckling of the crash absorber, the deformation confines to a small zone, thus, it offers a much lower capacity of energy absorption than the progressive buckling mode. Since the axial crash tubes are simply supported, the condition for the slenderness ratio λ to avoid global buckling, using equation (2.11) is

$$2 \cdot l \cdot \sqrt{\frac{A}{I}} (= \lambda) < \lambda_{\text{crit}}. \quad (5.1)$$

Rearranging equation 2.10 yields for the critical slenderness ratio λ_{crit}

$$\lambda_{\text{crit}} = \sqrt{\frac{\pi^2 \cdot E \cdot A}{F_{\text{max}}}} \quad (5.2)$$

with the peak force F_{max} , which is estimated based on the material's yield strength (here $R_{p0.2}$) and the cross section area of the crash tube by [122]

$$F_{\text{max}} = \sigma_y \cdot A. \quad (5.3)$$

Besides avoiding buckling, this initial peak force needs to be limited for two further reasons. Firstly, the supporting structure where the crash tube is mounted to has a limit load for failure, which must not be exceeded. Secondly, the forces and accelerations affecting the passengers must be limited to a tolerable range. This is reached by a proper design of crumple-zones, which dissipate the kinetic energy at a limit mean force over a certain interval of time.

Studies on the severity of whole-body accelerations on the human body suggest an absolute maximum bearable acceleration a of 200 times the normal acceleration g ($\frac{a}{g} = 200$) [69], yet only for very short impulse durations of $T_i < 6$ ms [104]. The longer the duration of the impact, the less acceleration is bearable and the higher is the risk of lethal injuries. A criterion for the occurrence of severe injuries, depending on acceleration and impulse duration is derived in [69]

$$T_i \cdot G^{2.5} = 1000 \quad (5.4)$$

with the pulse duration T_i in seconds and the dimensionless whole body acceleration $G = \frac{a}{g}$. For the typical pulse duration of car accidents of 100 ms to 200 ms [29], the bearable accelerations are about 30 g to 40 g. Similar criteria were deduced based on extensive experimental surveys for various body parts, such as the head injury criterion for head accelerations [54].

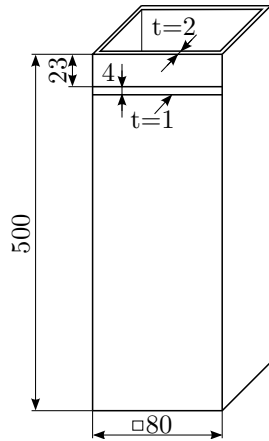
A stable progressive folding mode of the crash tube is started and facilitated by introducing a trigger, which predefines the shape of the first fold. Some exemplary trigger concepts are:

- hoop dents [1]
- local reduction of the tube's wall thickness [123]
- conical reduction of the tube's radius [119]
- thermally modified zones [86]

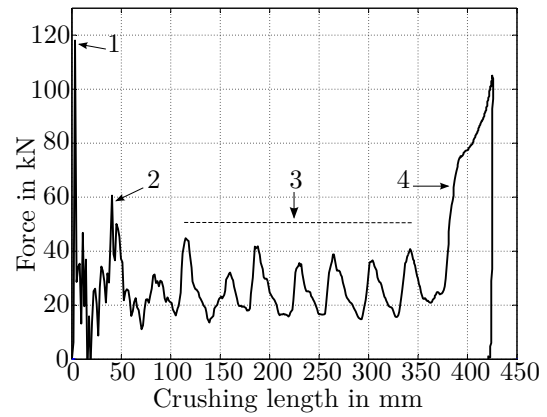
Figure 5.4(a) shows an exemplary extruded hollow crash tube with a square cross section and a wall-thickness reduction as trigger mechanisms. Figure 5.4(b) gives the corresponding force versus impactor–displacement plot evaluated in a drop-tower experiment, with the characteristic folding steps denoted

1. initial force peak at the moment of impact
2. peak for first fold
3. peaks for regular folding modes
4. compaction of the fully folded tube; the impact energy was too high for a complete absorption by folding.

The non-reinforced aluminum tube shows small cracks in the highly deformed folds, albeit no major cracks impair the structural response. The folding behavior of the triggered tube was reproduced by four crushed tubes and the force–displacement curve as well as the resulting fully crushed tube in figure 5.4(c) stands exemplary for all four tubes. Figure 5.4(d) shows simulation results, which were generated using material data provided by [88] and a phenomenological fracture model [82].



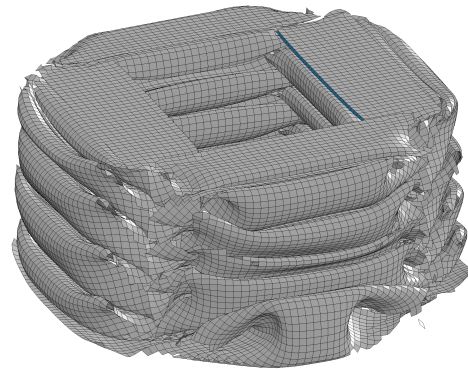
(a) Crash tube with square cross section and milled trigger, all dimensions in mm [123]



(b) Force versus crushing length for an impact of a rigid mass of 390 kg at a velocity of 8 m/s



(c) Crash tube after impact - experimental results



(d) Crash tube after impact - simulated results

Figure 5.4.: Geometry and force–displacement curve of a triggered extruded section with square cross section

5.2.2. Quasistatic compression behavior of steel-wire-reinforced crash tubes

First experiments considering the fracture behavior of steel-wire-reinforced aluminum crash tubes were performed by Wedekind¹. Circular crash tubes of the dimensions 44x5 mm with four reinforcing wires (90°-spacing) were impacted. Further analyses were made by the author with square reinforced sections as in figure 1.2(b).

Stubby tubes with a high thickness to width ratio are not appropriate for crash absorbing elements for three reasons:

- no proper progressive folding behavior [110]
- the high wall-thickness increases the initial peak force (see equation (5.3))
- a low slenderness ratio results in a low bending resistance, making it susceptible to global buckling, especially for off-axis crash events [134].

However, more suitable geometries were not available during the course of the investigations due to production limitations.

The results for stubby crash tubes made from SWRA, thus, should be understood as fundamental investigations considering the suitability of SWRA for crash tubes, since a general comparison of SWRA to non-reinforced aluminum is possible. Direct comparisons to standard automotive crash tubes are, at this technology readiness level, not significant.

Assessing the fracture behavior of crash tubes made from SWRA, Wedekind tested circular tubes with an impact energy of 1350 J. The impact caused a push-out of the high-strength steel wires into the mounting plate as shown in figure 5.5(b). This shows, that a total debonding of the steel wires occurred, which is predicted by simulation. Consequently, no further loads are transferred to the wire by interface shear stresses (except by contact) and the energy absorption of the wire is only due to bending in order to follow the folding of the aluminum matrix. This bending absorbs only little energy, as the deformation of the wire is confined to small areas in the fold [119].

Although the low impact energy only released one fold, the fracture behavior is evident. As already seen for the bolt-pull-out tests, the wires debond and the resulting void weakens the aluminum matrix, making it prone to fracture. The evolution of the crack is accelerated by the failed wire-matrix interface. With a progression of the crack through the crash tube, the energy absorption is reduced by the steel wires.

Crash tubes with a hollow square cross section and a higher reinforcement content were quasistatically tested by Matias [72]. Although not being tested dynamically, Jones [54] states that if the impacting mass is much larger than the tube mass and the impact velocities are in the order of up to some tens of meters per second, a quasistatic crushing test approximates the dynamic test reasonably well. This, is not true for materials with a pronounced strain rate sensitivity.

¹Max Wedekind, Lehrstuhl für Leichtbau, TU München



(a) Top view showing the first fold



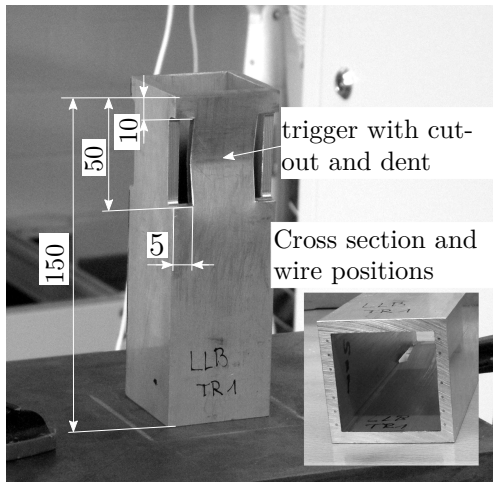
(b) Bottom view showing pushed-out wires

Figure 5.5.: Circular crash tube made from SWRA after impact with 1350 J (photos courteously provided by M. Wedekind)

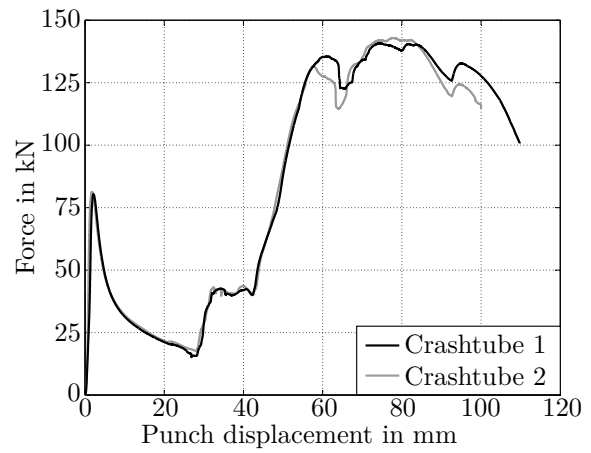
In order to release a stable folding, the tubes are triggered in a combined approach using both dents and cutouts as shown in figure 5.6(a). The folding stands exemplary for the folding behavior of two tested specimens. A third specimen did not enter a stable buckling and the test was aborted.

Analysing the force–displacement curve, a low initial peak force of about 80 kN is achieved by the triggering strategy. With the start of the second fold, the peak folding force rises above the initial peak force to 140 kN. This is caused by the geometrically stiff edges, which were cut out for the trigger but now have to follow the folding motion of the second fold. A further increase in the folding force is caused by contact of the folds, blocking their free motion. The folding behavior is almost exclusively defined by the geometry of the aluminum tube. This is confirmed by simulations of the SWRA tube and a non-reinforced tube, which show very similar folding patterns and force–displacement curves. With the currently manufacturable wall-thicknesses, the high crushing forces stand against a use of SWRA for crash tubes. Further, the failure and fracture characteristics of the SWRA tube leads to the conclusion, that the aluminum section does not profit from a steel wire reinforcement.

Figures 5.6(c), 5.6(d) summarize the characteristics of the fracture behavior of the square reinforced tube. The SWRA tube shows a push-out of the wires into the mounting plate, similar to the cylindrical tubes. With a total debonding of the wires, a reinforcement is no longer given and an increased energy absorption is unlikely. Initial cracks develop in the aluminum matrix at the corner positions of the cut-outs. These cracks turn into the direction of the closest wire element and split the aluminum matrix along the failed wire-matrix interface. More cracks are detected at further wire positions, hence, the wires encourage the formation of cracks and reduce the energy absorption of the tube.



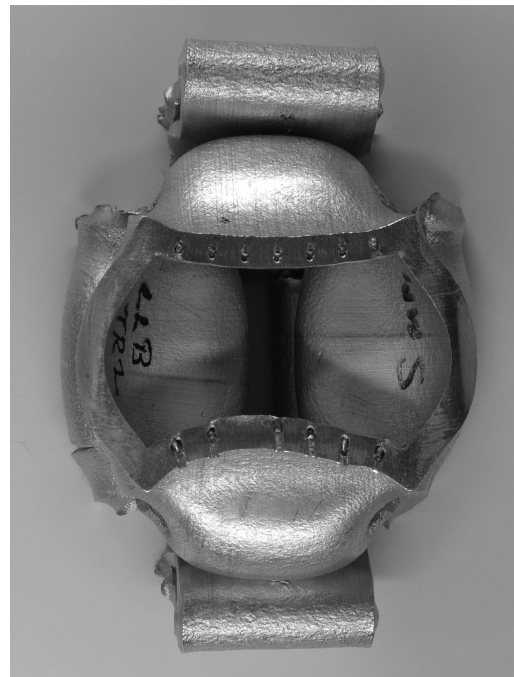
(a) Square crash tube made from SWRA with cut-out and initial dents as trigger



(b) Force-displacement curve for quasistatic crushing of square crash tube made of SWRA [72]



(c) Top view of SWRA square crash tube after quasistatic crushing



(d) Bottom view of SWRA square crash tube after quasistatic crushing

Figure 5.6.: Square crash tube made from SWRA before and after quasistatic crushing

5.3. Three-point bending with an impact load

A second type of crash absorbing element is analyzed with a reinforced section under a three-point bending load. This idealized load case is exemplary for an automotive B-pillar at a side-crash event. Previous research on this topic was done by Matias and Morasch [72], who used a SWRA profile with a square cross section and a drilled hole under a quasistatic three-point bending load, in order to examine a simplified material and fracture model for SWRA based on a shell-beam model. Matias used similar SWRA sections of the dimensions 50x50x5 mm and found, that no fracture occurs for non pre-damaged sections [72, 80]. Therefore, holes were drilled into the sections in order to release fracture for a validation of a simplified material and fracture model. The specimens are shown in figure 5.7. Stöckl [106] further used the same geometry to validate the here shown material and fracture modeling technique based on 3D-volume elements.

The results of the quasistatic tests were used in order to assess the energy absorption of the bending specimens and the experimental setup was transferred to an impact test conducted at the drop tower of TU Dresden².

5.3.1. Experimental test setup

All specimens were impacted with a mass of 46 kg dropped from a height of 4.45 m, resulting in an impact energy of approximately 2 kJ. Non-reinforced sections were impacted at the same conditions, in order to assess the effect of the wire reinforcement. At least three specimens of each type (16 mm and 26 mm hole, non-reinforced aluminum and SWRA) were tested and force and displacement of the impactor were recorded at a frequency of 20 kHz. The impact was filmed with a high-speed camera system and the force signal was post-processed with a 6th order butterworth filter and a corner frequency of 4 kHz.

5.3.2. Interpretation of test results

The three-point bending impact is shown exemplary for all tested specimens in the series of images in figure 5.8, each depicting corresponding force over impact displacement and impactor velocity together with a photo from high-speed imaging. The impact can be divided into four stages:

1. initial contact
2. plastic deformation
3. onset of fracture and evolution accompanied by loss of resistance
4. sliding of the fractured section into the gap between the supports

²Leichtbau-Zentrum Sachsen GmbH, www.lzs-dd.de

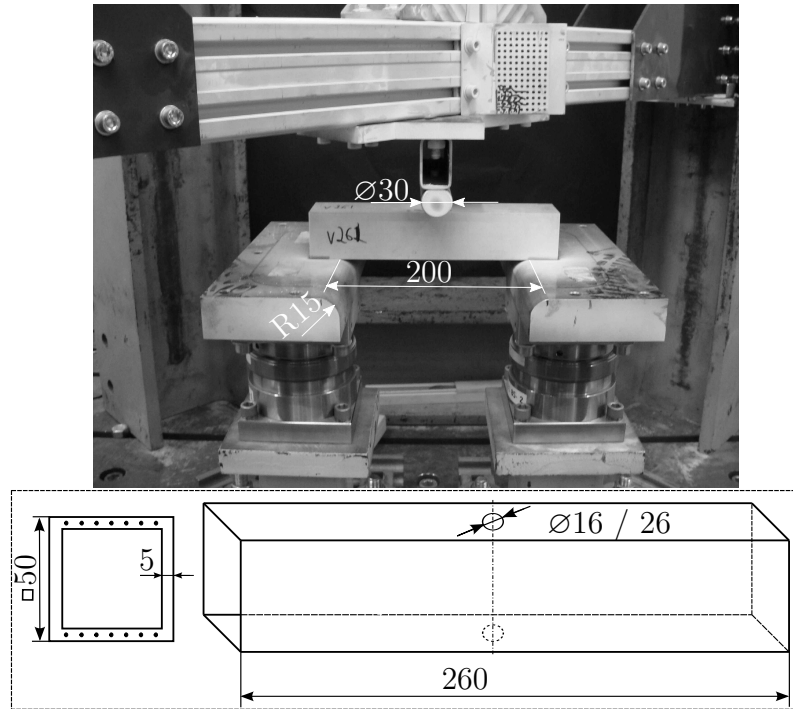


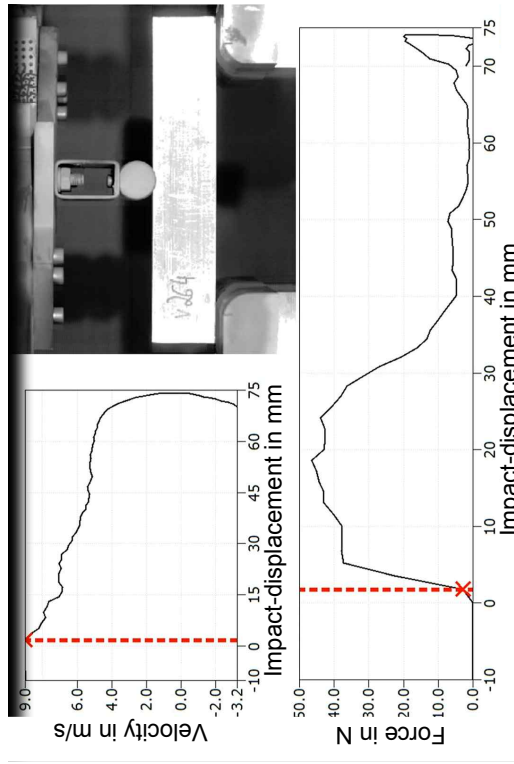
Figure 5.7.: Experimental setup and test specimen for three-point bending test with an impact load; pre-damaged SWRA section with drilled holes

After the initial impact, most energy is absorbed by means of elasto-plastic deformation of the bending section. The exact start of the fracture process is not recorded by the videos, since it starts for all specimens in the tension region at the drilled hole in the lower chord.

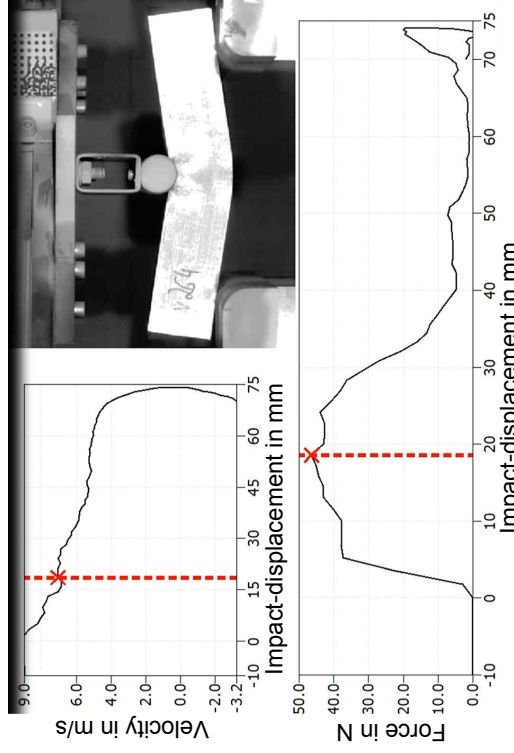
Simulations predict an onset of fracture shortly after reaching the maximum force, starting with a fracture of the first wire next to the drilled hole.

During the quasistatic bending tests of Matias [72], this behavior was observed with a clearly audible cracking noise of the wire, before a visible fracture of the matrix set in. The following loss of resistance is caused by crack growth and by softening due to the geometric nonlinearity of the problem. Non-reinforced and reinforced section with a small hole of 16 mm absorb all incoming energy before sliding into the gap between the supports, whereas the sections with a hole diameter of 26 mm do not. They rip up to the upper chord and are compressed into the supports, which finally absorbs the remaining kinetic energy. For evaluation of the absorbed crash energy, the compression of the sections with 26 mm hole is excluded.

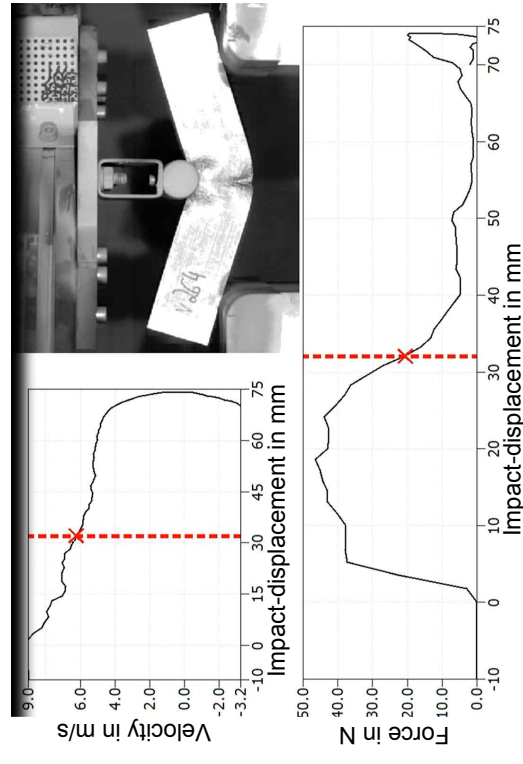
Comparing non-reinforced and reinforced sections, a crack arresting effect or a crack deflection along the wire-matrix interface when the crack strikes a steel wire is not observed. Since the wire content in the reinforced chords is low at only $\phi_w = 2\%$, the differences between reinforced and non-reinforced aluminum are small to negligible. This is obvious when comparing the force-displacement curves of reinforced and non-reinforced specimens in figure 5.9. Despite of the small differences, the



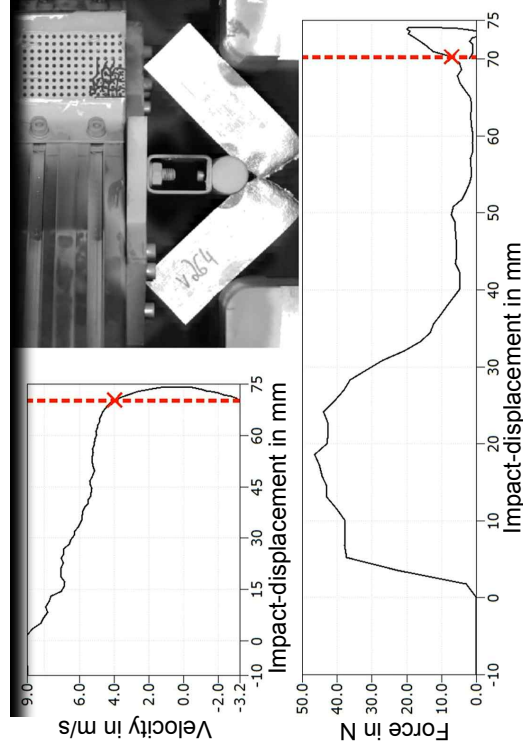
(a) Stage 1: Initial impact



(b) Stage 2: Elasto-plastic energy absorption



(c) Stage 3: Onset of fracture and evolution accompanied by loss of resistance



(d) Sliding of the fractured section and compaction between supports

Figure 5.8.: Four characteristic stages of the three-point bending test with an impact load

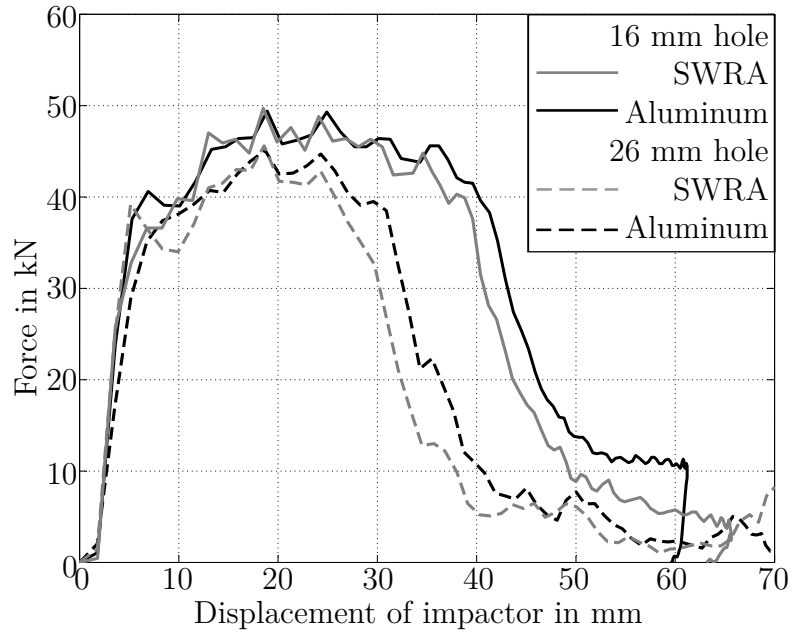


Figure 5.9.: Force–displacement curves for non-reinforced and reinforced specimens with drilled holes of 16 mm and 26 mm diameter

energy absorption of all tested reinforced sections is lower than of the corresponding non-reinforced sections.

An overview on experimental results is given in table 5.1. The energy absorption is calculated via the force–displacement curve and shows continuously lower absorption capacities for the SWRA specimens. However, the differences in averagely absorbed energy between non-reinforced and reinforced specimens are maximally 9.4% at this low wire content. This is also reflected in the force–displacement curves shown in figure 5.9.

Even with constantly lower energy absorptions during the three-point bending tests, a concluding statement on benefits or disadvantages of a steel-wire reinforcement on the energy absorption cannot reliably be made. Firstly, the sections were pre-damaged in order to release fracture for an evaluation of a crack arresting effect of the wires and a validation of a fracture model. Thus, some of the reinforcing wires are cut and do not fully participate in the energy absorption. Secondly, the load case causes a deformation that concentrates on a narrow area as seen from figure 5.8 and the high-strength of the wires is only used in the center area. For these reasons, a validation of the simulation methodology also for dynamic impact conditions is done. With valid simulation models, a reliable assessment of the crash performance of SWRA is made.

Table 5.1.: Energy absorption of bending sections with drilled holes made from SWRA and non-reinforced aluminum

Specimens non-reinforced, 16 mm hole	Impactor velocity before impact in m/s	Kinetic energy in J	Absorbed energy in J
UV161	9.16	1930	1948
UV162	9.09	1900	1994
UV163	9.17	1934	1997
UV164	9.12	1913	1999
Average			1985
Specimens SWRA, 16 mm hole	Impactor velocity before impact in m/s	Kinetic energy in J	Absorbed energy in J
V161	9.07	1892	1866
V162	9.12	1913	1893
V163	9.10	1905	1880
Average			1880
Specimens non-reinforced, 26 mm hole	Impactor velocity before impact in m/s	Kinetic energy in J	Absorbed energy in J
UV261	8.97	1851	1464
UV262	8.95	1842	1440
UV263	9.05	1884	1554
Average			1486
Specimens SWRA, 26 mm hole	Impactor velocity before impact in m/s	Kinetic energy in J	Absorbed energy in J
V261	8.97	1851	1347
V262	8.97	1851	1316
V263	8.98	1855	1368
V264	9.00	1863	1401
Average			1358

5.4. Validation of the simulation methodology by dynamic three-point bending test with an impact load

The discussed SWRA sections subjected to the dynamic impact load as in figure 5.7 are modeled for correlation and validation purposes under dynamic conditions. The simulation methodology, which was validated for quasistatic conditions with bolt-pull-out tests is used. Since the dynamic impact tests took place four months after the bolt-pull-out tests, the aluminum matrix further age hardened. In order to account for the higher strength, the strain hardening curve from layered-compression tests (see appendix A.5) is taken, which were conducted after the dynamic impact tests. It is further assumed that the fracture properties of the stronger aluminum matrix remain unchanged. As determined in specimen tests, strain rate hardening effects are very small and, therefore, are neglected.

The two-fold symmetric simulation model is shown in figure 5.10. Contact between impactor and section, as well as between section and bending support is modeled via contact conditions. Therefore, a segment based contact model is utilized, which is favorable over a standard node penalty based contact at detecting penetrations for edge-to-edge contact [66]. Changing contact surfaces of the section due to material erosion and fracture are taken into account by using an erosive contact model.

Table 5.2 lists the energy absorption of experiment and simulation for the two considered SWRA specimens. The differences between the simulated and experimental values are below 15 %, which presents a good agreement considering the complexity of the problem. The force–displacement curves shown in figure 5.11 match in terms of maximum force, fracture onset and fracture evolution, so that the simulation methodology and the material model is validated also for highly dynamic loads. A higher energy absorption in the simulation stems from a higher strain hardening based on the layered-compression tests, which were performed after the impact tests.

Table 5.2.: Comparison of energy absorption of reinforced bending sections with drilled holes from experiment and simulation

Specimen	16 mm hole	26 mm hole
Average energy absorption in J from experiment	1880	1358
Simulated energy absorption in J	1994	1550
Difference in %	6.06	14.1

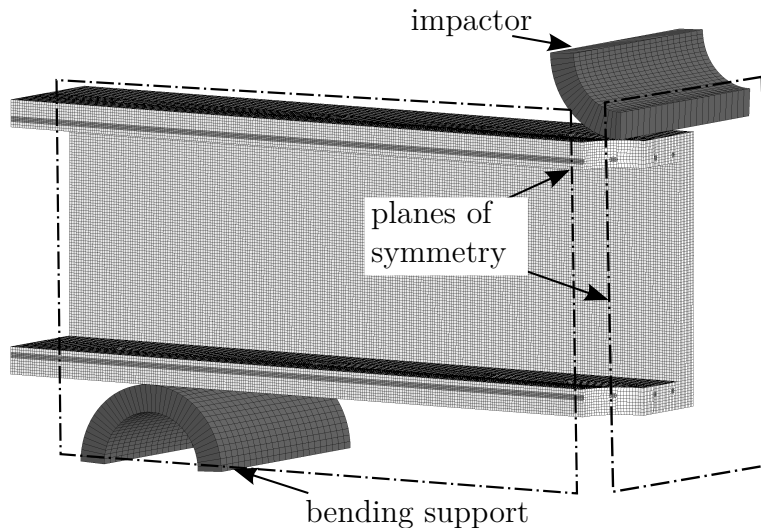


Figure 5.10.: Twofold-symmetric simulation model of reinforced section with drilled holes under impact load and bending support

5.5. Fully clamped section under impact load

An idealized load case which is considered to make best use of the high-strength of the steel wires is a fully clamped section under a bending impact load. With clamped wires, the impact load is introduced even when the interface between wire and matrix completely fails. The clamping is experimentally hard to ensure, yet could be done by welding the sections to load bearings. However, the aluminum matrix would be weakened in the heat-affected zone and a clamping of the wires is not possible by welding. This makes the section prone for failure at the fixture, not allowing for a meaningful analysis. With these experimental difficulties in mind, a comparison between fully clamped SWRA and aluminum sections is done solely based on numerical simulation.

In order to retain comparability to the pure three-point bending tests, the fully clamped sections rest on the same bending supports as used before. Exploiting the twofold symmetry, only a quarter of the problem is simulated with the simulation model of the dynamic impact bending simulation in figure 5.12. An impacting mass of 390 kg at 8 m/s, results in a total impact energy of 12.48 kJ for the quarter model and 49.92 kJ for the full section. This impact energy was sufficient to completely fracture the fully clamped sections and allows for the evaluation of the totally absorbed energy.

Fracture in the non-reinforced aluminum is predicted in the middle of the section where the impactor strikes, with a small crack at the fixture. For the SWRA section, the bending impact causes a debonding of the wires. The then unsupported wires start necking and fracture early. Please note, that even though a total debonding of the wires occurred, interface friction and bending of the wires caused a

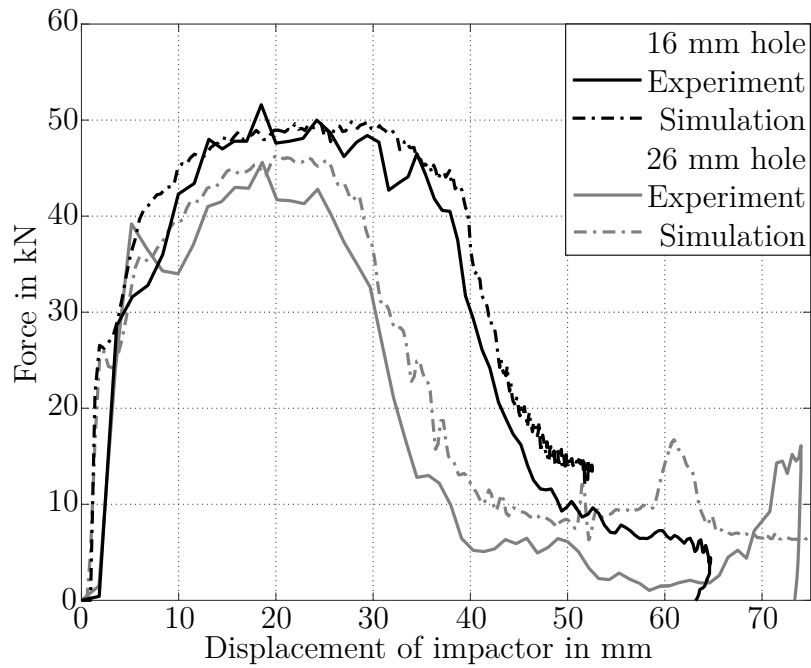


Figure 5.11.: Experimental and simulated force–displacement curves for reinforced specimens with drilled holes of 16 mm and 26 mm diameter

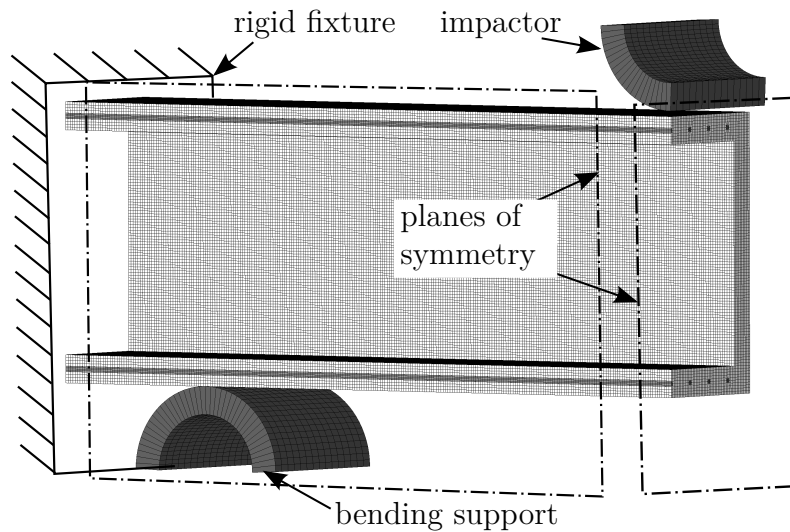


Figure 5.12.: Twofold-symmetric simulation model of fully clamped reinforced hollow section under impact load and bending support

multiple fracture of the wires, shown in figure 5.13(c). The aluminum matrix subsequently necks and fractures at the position where the wires have fractured (see figure 5.13(b)). This happens at a lower global deformation than in non-reinforced aluminum, additionally, the evolution of the crack is faster in the by wire-fracture pre-damaged aluminum matrix.

The totally absorbed energy of the SWRA section, therefore, is with 8.14 kJ about 23% lower than the absorbed energy by the non-reinforced aluminum section with 10.54 kJ. However, the position of the wire fracture is decisive for the position of fracture in the aluminum matrix and will lead to a different energy absorption of SWRA. Changing the fracture model of the wires from the softening model from section 4.6.2 to a model without softening and a fracture strain of $\varepsilon_{fr}^p = 0.4$ shifts the wire fracture and causes a fracture in SWRA similar as in the non-reinforced aluminum section. The absorbed energy of SWRA then is higher with 10.17 kJ.

In any case, it can be concluded, that the energy absorption of SWRA is sensitive to the position of wire fracture which defines the position of matrix fracture and weakens the resistance of the aluminum matrix. The energy absorption of the wires does not significantly contribute to the totally absorbed energy and is for both analyzed wire fracture models in the range of 374 to 438 J.

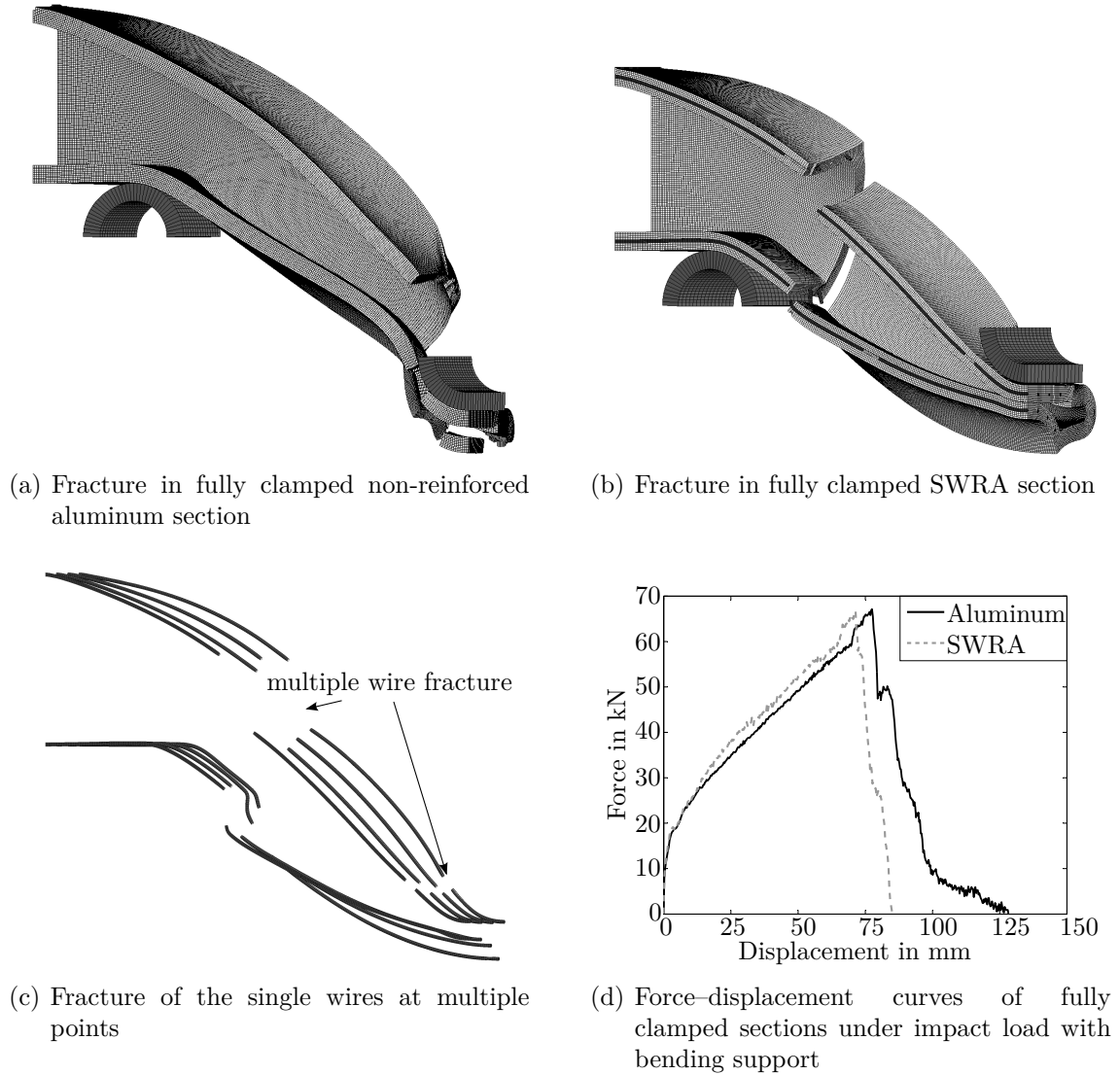


Figure 5.13.: Fracture of a fully clamped, wire reinforced section under dynamic impact crushing and bending support

6. Outlook on improvements to steel-wire-reinforced aluminum with respect to energy absorption

It was shown that the currently fabricable sections of SWRA do not offer a better performance for crash absorbing structures compared to non-reinforced aluminum. Moreover, fabrication restraints further limit the use of SWRA in crash absorbers. Bearing in mind that the composite extrusion technology is rather young, future improvements are probable and will allow for a higher reinforcement content, a better interface strength and, with higher press capacity, also aluminum matrices with higher strengths. For flat extruded members, the aluminum alloy EN AW-6082 has already been fabricated with a reinforcement content of $\phi_w \approx 13\%$ and a wall-thickness of 3 mm (see figure 6.1).

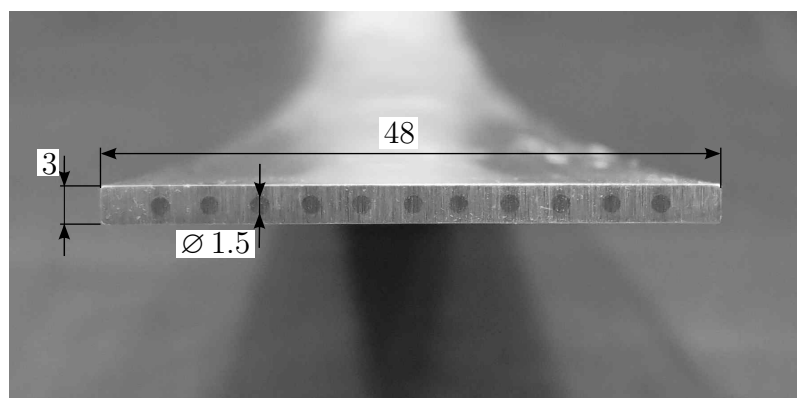


Figure 6.1.: Flat reinforced section with a wire content of $\phi_w = 13.5\%$

In this chapter, the effects of future improvements on the energy absorption of SWRA structures is predicted. This will help finding profitable ways of improving SWRA. For quasistatic loading and on a specimen scale, expectable improvements have already been discussed in section 4.6, so that further analyses are made at the example of the fully clamped bending section under impact load. All analyzed section geometries are summarized in figure 6.2. For a better readability, the sections are abbreviated according to their cross section and wire content as in figure 6.2.

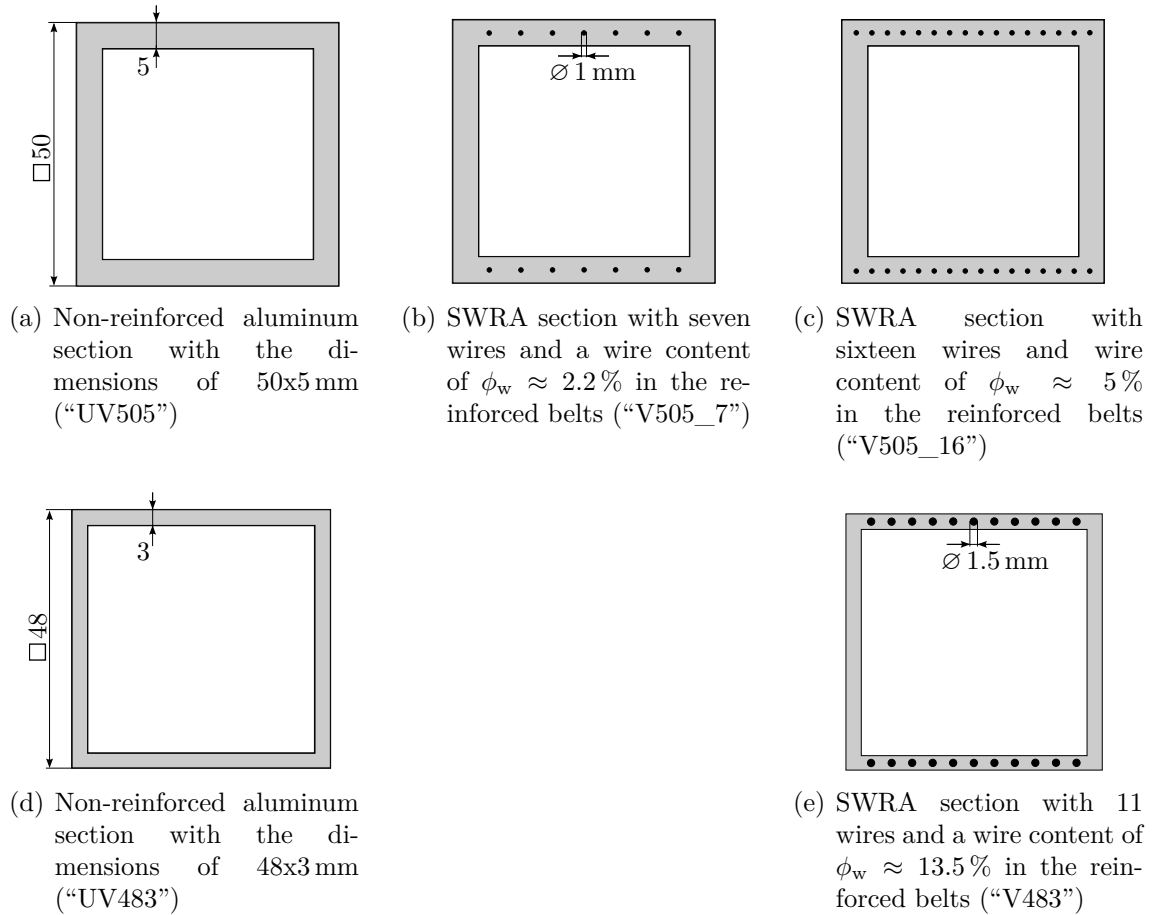


Figure 6.2.: Cross section geometries of simulated sections with prospective improvements

6.1. Improved interface strength

By improving the interface strength, the wire is kept from necking, which is the main reason for wire fracture. The high strength of the wire is sustained for higher strains, which results in a higher energy absorption. For an optimal use of the wire’s strength, an infinitely strong interface is considered. This, however, does not allow for a crack deflection along the wire-matrix interface and further hinders the matrix from deforming freely.

Since wire fracture occurs even without prior debonding, a fracture strain of $\varepsilon_{fr}^p = 0.7$ is applied. For this case, fracture of the matrix is not initiated by fracture of the wires. The wires are supported until fracture of the matrix so that the interface with infinite strength is considered as best case scenario. Due to the local deformation of the impact bending load, high strains in the wires are only local and the by the wires absorbed energy is low. The increase in energy absorption by the infinite interface strength by 54% compared to the original interface strength, therefore, has to be attributed to the fact, that fracture of the matrix is no longer

initiated by wire fracture. The results are listed in table 6.2.

6.2. Increased wire content

A higher wire content is simulated based on the three sections in figures 6.2(b), 6.2(c), 6.2(e). Firstly, the higher wire content is obtained by increasing the number of wires in the reinforced belts from 7 to 16 wires, with the wire content in the reinforced belts rising from $\phi_w = 2.2\%$ to $\phi_w = 5\%$. Secondly, based on the shown flat sections with a wire content of $\phi_w = 13.5\%$ (figure 6.1), a reinforced hollow section is modeled. The material properties of the thicker wires, as well as the thinner matrix are assumed to be unchanged.

The resulting energy absorptions for a higher wire content are summarized in table 6.3. A higher wire content leads to a less aggravated capability of energy absorption. Since the sections with higher reinforcement content are stiffer, the bending deformation is more homogeneous and less concentrated to the impact area. This causes a better participation of the steel wires and increases the toughness of the section. However, the energy absorption is still lower than for the non-reinforced aluminum section.

6.3. Aluminum matrix with higher strain hardening

Aluminum matrices for composite extrusion were reviewed by Weidenmann [124], with extrudability as one main criterion. He suggested three alloys EN AW-6060, EN AW-6063 and EN AW-6005A, which, aside from extrudability, offer age hardening, weldability and a good resistance to corrosion. The extrudability of these alloys, however, comes with a low strength. During the course of the project TR10, a quenching was included into the manufacturing chain of composite extrusion. Hammers [43] concentrated on the influence of quenching, heat treatment and stretch-forming of composite extruded members and analyzed reinforced aluminum with matrices of EN AW-6056 and EN AW-2099. EN AW-6056(T6) and EN AW-2099(T6) both offer an increased UTS of 260 MPa and 249 MPa, respectively. Merzkirch [77] examined steel-wire-reinforced aluminum with an EN AW-6082 alloy with an UTS 210 MPa. Possible improvements due to an increased strength of the aluminum matrix are assessed in the following.

For a material characterization of EN AW-6082T6, Reeb supplied tensile test data from axisymmetric circular specimens, taken from an extruded section with a wall-thickness of 5 mm. Based on the test data, the strain hardening parameters of Voce's function are identified in a constrained fitting approach; they are summarized in table 6.1. With the experimentally determined strain hardening, the axisymmetric GTN parameters are evaluated. Therefore, the GTN parameters of EN AW-6060 as in table 4.1 were tried as starting values, which already led to an almost perfect

Table 6.1.: Identified strain hardening parameters of Voce’s function for EN AW-6082T6

Yield strength σ_y	Saturation stress σ_s	Prestrain ε_0
145.23	347.44	0.0803

agreement between simulated and experimental force–strain curve (see figure 6.3). Thus, no further adjustment was necessary. Since shear test data was not available for this alloy, the shear damage parameter is assumed to be unchanged. This assumption conveniently leads to a separate examination of the effect of a higher strain hardening of the aluminum matrix on the crashworthiness of steel-wire-reinforced aluminum, decoupled from changing fracture parameters. Since the axial interface shear strengths of the by Hammers [43] and Merzkirch [77] analyzed systems are close to the one of the discussed SWRA system, the interface properties are also assumed to be unchanged.

Table 6.4 summarizes the energy absorption of non-reinforced and SWRA sections with EN AW-6082T6 matrix. It is obvious, that the stronger aluminum matrix leads to a higher energy absorption in every simulated case. The wires absorb a little more energy, since the higher strength of the matrix leads to a more global deformation of the section in contrast to high local deformations around the impactor for the ductile matrix. Therefore, a more even loading of the wires leads to a higher energy absorption. However, an improvement of the total energy absorption due to a wire reinforcement is not detectable for the stronger matrix alloy.

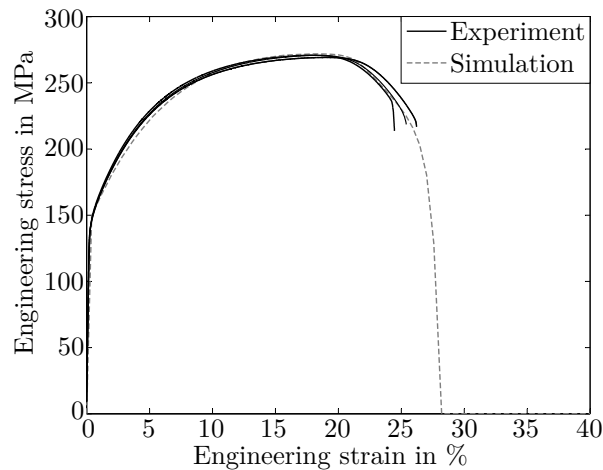


Figure 6.3.: Experimental and simulated stress–strain curves with optimized Gurson parameters for EN AW-6082

Table 6.2.: Energy absorption of fully clamped sections under impact bending load, SWRA with varying interface strength

Interface strength	non-reinforced	$\sigma_{n_{\max}} = 25$	$\sigma_{n_{\max}} = \infty$, wire fracture $\varepsilon_{fr}^p = 0.7$
Cross section	UV505	V505_7	V505_7
Energy absorption in J	10542	8139	12585
Energy absorbed by the wire in J	0	374	688

Table 6.3.: Energy absorption of fully clamped sections, SWRA with varying wire content

Wire content	0 %	0 %	2.2 %	5 %	13.5 %
Cross section	UV505	UV483	V505_7	V505_16	V483
Energy absorption in J	10542	4179	8139	9156	3832
Energy absorbed by the wire in J	0	0	374	806	452

Table 6.4.: Energy absorption of fully clamped sections under impact bending load, SWRA with increased matrix strength

Higher aluminum strength (EN AW-6082)					
Cross section	UV505	UV483	V505_7	V505_16	V483
Energy absorption in J	14458	5766	12654	13959	5420
Energy absorbed by the wire in J	0	0	402	772	522

6.4. Summary and discussion of energy absorption of SWRA with prospective improvements

An increased interface strength is one approach to an improvement of SWRA. As best case scenario, an infinitely strong interface was assumed, which significantly improved the energy absorption of SWRA. This is for one part due to a better use of the high strength of the steel wires, which can be seen from a higher energy absorption of the wires. For the other part, the aluminum matrix is not weakened by internal wire fracture. For the case that a much stronger interface can be reached, the increase in energy absorption compared to non-reinforced aluminum is 18.5 % for the considered load case. An infinitely strong interface is not possible and the sensitivity analyses in section 4.6 showed, that increasing the interface's normal strength even by one order of magnitude from currently $\sigma_{nmax} = 11$ MPa to $\sigma_{nmax} = 110$ MPa, does not lead to noteworthy improvements. Higher improvements are doubtful considering an already attentive pre-treatment of the wires for a good bonding [124]. Therefore, increasing the interface's strength is not a viable way to improve the performance of SWRA in crash events.

A higher steel wire content slightly improved the performance of SWRA, since the bending sections are deforming more homogeneously and the wires participate more in an energy absorption. However, the performance of the non-reinforced aluminum alloy was not reached.

From a structural point of view, it is for this clamped bending section much more beneficial to switch to a non-reinforced aluminum section with higher strength, than to reinforce a ductile matrix with steel wires. The improvement in energy absorption for the stronger aluminum matrix was found to range from 37.1 % to 41.4 % for the two cross section geometries. Since the clamped bending scenario is assumed being a best case scenario, a better energy absorption of SWRA at other impact load cases is improbable.

7. Conclusion

The basic idea of a hybrid material is that the strengths of two materials are combined and their weaknesses are reduced or even eliminated. SWRA, therefore, has to compete against non-reinforced aluminum alloys and the mechanical benefits must not only outweigh negative aspects of the hybridized material, but also outweigh higher costs due to a higher complexity of the production process. This work evaluated on the mechanical performance of SWRA, focusing on its fracture behavior, with a possible application in automotive crumple-zones in mind.

Analyzing the material's elastic properties, the rule of mixture was confirmed for the calculation of Young's modulus of SWRA. Sections under pure bending are an interesting application for SWRA, since the mass-specific stiffness increases in comparison to non-reinforced aluminum. Thermal residual stresses lead to a decrease in tensile yield strength and an increase in compressive yield strength. A stretch-forming of the extruded sections will release the residual stresses and with them the strength-differential effect. If no stretch-forming is done, an increased compressive yield strength is beneficial for instance for axially compressed struts.

Focusing on the material's plastic properties and on failure and fracture behavior, the process of debonding of the wires was shown to be a major source of material failure for all load cases different from uniaxial loading in wire direction. Subsequently to debonding, the wires neck and fracture and the resulting gaps weaken the aluminum matrix, which fractures earlier than the non-reinforced aluminum alloy. Therefore, neither a higher fracture toughness nor a higher capacity of energy absorption are reached by steel-wire reinforcement. This was shown by quasistatic and dynamic impact simulations and was confirmed by experiments. Prospective improvements of SWRA were evaluated, yet, neither a higher wire content, nor the use of a stronger aluminum matrix led to an improved energy absorption compared to the non-reinforced aluminum alloy. Considering the best case of an infinitely strong, non-failing interface between wire and matrix, the attainable improvements in fracture toughness and capacity of energy absorption turned out to be rather limited.

Based on the performed analyses, a steel-wire reinforcement for aluminum sections undergoing dynamic impact loadings is not recommended.

References

- [1] W. Abramowicz. Thin-walled structures as impact energy absorbers. *Thin. Wall. Struct.*, 41:91–107, 2003.
- [2] W. Abramowicz and N. Jones. Dynamic axial crushing of square tubes. *Int. J. Impact Engng.*, 2:179–208, 1984.
- [3] T. Altan and A.E. Tekkaya, editors. *Sheet metal forming – Fundamentals*. ASM International, 2012.
- [4] H. Altenbach and V.A. Kolupaev. Classical and non-classical failure criteria – Examples of failure behavior. International centre for mechanical sciences (CISM) - Udine, Italy, September 30 – October 4, 2013. Failure and damage analysis of advanced materials.
- [5] M. Arcan, Z. Hashin, and A. Volosin. A method to produce uniform plane-stress states with applications to fibre-reinforced materials. *Exp. Mech.*, 18:141–146, 1978.
- [6] M.F. Ashby. *Materials selection in mechanical design*. Butterworth-Heinemann, 3rd edition, 2005.
- [7] O.S. Aslan. Buckling analysis of metal matrix composites and structural optimization of space frame with buckling and displacement constraints using semi analytical gradient calculation. Master’s thesis, Technische Universität München, 2010.
- [8] ASME B31.1a-2008. Addenda to ASME B31.1-2007, Power Piping, ASME Code for Pressure Piping, B31, 2008.
- [9] D. Banabic. *Sheet metal forming processes – Constitutive modelling and numerical simulation*. Springer-Verlag Berlin Heidelberg, 2010.
- [10] D. Banabic, H.-J. Bunge, K. Pöhlandt, and A.E. Tekkaya. *Formability of metallic materials - Plastic anisotropy, formability testing, forming limits*. Springer-Verlag Berlin Heidelberg, 2000.
- [11] F. Barlat, J.C. Brem, J.W. Yoon, K. Chung, R.E. Dick, D.J. Lege, F. Pourboghrat, S.-H. Choi, and E. Chu. Plane stress yield function for aluminum alloy sheets – Part I: theory. *Int. J. Plasticity*, 19:1297–1319, 2003.

- [12] F. Barlat and M.-G. Lee. Constitutive description of isotropic and anisotropic plasticity for metals. International centre for mechanical sciences (CISM) - Udine, Italy, September 30 – October 4, 2013. Failure and damage analysis of advanced materials.
- [13] F. Barlat, D.J. Lege, and J.C. Brem. A six-component yield function for anisotropic materials. *Int. J. Plasticity*, 7:693–712, 1991.
- [14] F. Barlat and J. Lian. Plastic behavior and stretchability of sheet metals. Part I: A yield function for orthotropic sheets under plane stress conditions. *Int. J. Plasticity*, 5:51–66, 1991.
- [15] Z.P. Bažant. Easy-to-compute tensors with symmetric inverse approximating Hencky finite strain and its rate. *J. Eng. Mater. Technol.*, 120:131–136, 1998.
- [16] A.A. Benzerga and J.-B. Leblond. Ductile fracture by void coalescence. *Advan. Appl. Mech.*, 44:169–305, 2010.
- [17] F.A. Berg, P. Rücker, W. Niewöhner, E. Miltner, and K.M. Stein. Progress of passive safety in car-to-car frontal collisions: results from real-life crash analyses and from crash tests. DEKRA online document, <http://www-nrd.nhtsa.dot.gov/pdf/esv/esv17/Proceed/00198.pdf>, 2000(?). Visited on 20th of August 2015.
- [18] B. Bhushan and B.K. Gupta. *Handbook of tribology – Materials, coatings, and surface treatments*. McGraw-Hill, New York, 1991.
- [19] J.F.W. Bishop and R. Hill. A theory of the plastic distortion of a polycrystalline aggregate under combined stresses. *Phil. Mag.*, 42:414–427 and 1298–1307, 1951.
- [20] J. Both, T. Brüggemann, S. Dosch, J. Elser, M. Kronthaler, A. Morasch, M. Otter, D. Pietzka, A. Selvaggio, C. Weddeling, E. Wehrle, F.X. Wirth, H. Baier, D. Biermann, A. Brosius, J. Fleischer, G. Lanza, V. Schulze, A. Tekkaya, A. Zabel, and M.F. Zäh. Advanced manufacturing and design techniques for lightweight structures. *International Aluminium Journal*, (87):60–64, 2011.
- [21] P.W. Bridgman. *Studies in large plastic flow and fracture: with special emphasis on the effects of hydrostatic pressure*. Harvard University Press, 1964.
- [22] W. Callister and D.G. Rethwisch. *Materials science and engineering: An introduction*. Wiley, 8th edition, 2010.
- [23] J.D. Campbell and W.G. Ferguson. The temperature and strain-rate dependence of the shear strength of mild steel. *Philosophical Magazine*, 21:63–82, 1969.

- [24] N. Chandra and C.R. Ananth. Analysis of interfacial behavior in MMCs and IMCs by the use of thin-slice push-out tests. *Comp. Sci. Tech.*, 54:57–100, 1995.
- [25] Y. Chen, A.H. Clausen, O.S. Hopperstad, and M. Langseth. Stress–strain behaviour of aluminium alloys at a wide range of strain rates. *Int. J. Solids Struct.*, 46:3825–3835, 2009.
- [26] J.M. Choung and S.R. Cho. Study on true stress correction from tensile tests. *J. Mech. Sci. Technology*, 22:1039–1051, 2008.
- [27] M. Considère. Memoire sur l’emploi du fer et de l’acier dans les constructions. *Annales des ponts et chaussees*, 9:574, 1885.
- [28] G.R. Cowper and P.S. Symonds. Strain hardening and strain rate effect in the impact loading of cantilever beams. Brown University, Division of Applied Mathematics, report, 28, 1957.
- [29] D.J. Dalmotas and J.-L. Comeau. Crash pulse analysis using event data recorders. Proceedings of the 19th Canadian Multidisciplinary Road Safety Conference, Saskatoon, Saskatchewan, June 8–10, 2009, 2009.
- [30] E. Diez. Material modelling of steel wire reinforced aluminum for the assessment of its fracture locus. Master’s thesis, Technische Universität München, 2015.
- [31] DIN 29850. Luft- und Raumfahrt Wärmebehandlung von Aluminium-Knetlegierungen, 1989.
- [32] DIN 50106. Prüfung metallischer Werkstoffe - Druckversuch, 1978.
- [33] DIN 50115. Prüfung metallischer Werkstoffe - Kerbschlagbiegeversuch, Besondere Probenform und Auswerteverfahren, 1991.
- [34] DIN 50125. Prüfung metallischer Werkstoffe - Zugproben, Fassung DIN 50125:2009-07, 2009.
- [35] DIN EN 10045-1. Metallische Werkstoffe - Kerbschlagbiegeversuch nach Charpy - Teil 1: Prüfverfahren - Deutsche Fassung EN 10045-1:1990, 1991.
- [36] DIN EN ISO 6892-1:2009-12. Metallische Werkstoffe - Zugversuch - Teil I: Prüfverfahren bei Raumtemperatur (ISO 6892-1:2009); Deutsche Fassung EN ISO 6892-1:2009, 2009.
- [37] DIN ISO 10113. Metallische Werkstoffe - Blech und Band - Bestimmung der senkrechten Anisotropie (ISO 10113:2006, 2010).
- [38] F. Dunne and N. Petrinic. *Introduction to computational plasticity*. Oxford University Press, 2005.

- [39] E. El-Magd. Mechanical properties at high strain rates. *Journal de Physique IV*, 4, 1994.
- [40] T. Emde. *Mechanisches Verhalten metallischer Werkstoffe über weite Bereiche der Dehnung, der Dehnrates und der Temperatur*. PhD thesis, RWTH Aachen, 2008.
- [41] H. Gese. Material models of metals for crash simulation. Training course at carhs.training GmbH in Alzenau Germany, 2011.
- [42] A.L. Gurson. Continuum theory of ductile rupture by void nucleation and growth: Part I – Yield criteria and flow rules for porous ductile media. *J. Eng. Mater. Technol.*, 99:2–15, 1977.
- [43] T. Hammers. *Wärmebehandlung und Recken von verbundstranggepressten Luftfahrtprofilen*. PhD thesis, Karlsruher Institut für Technologie, 2012.
- [44] S.S. Hecker. Experimental studies of yield phenomena in biaxially loaded metals. *ASME Winter Symposium on constitutive relations in plasticity: Computational and engineering Aspects*, 1976.
- [45] A.V. Hershey. The plasticity of an isotropic aggregate of anisotropic face centered cubic crystals. *J. Appl. Mech. - Trans ASME*, 21:236–240, 1954.
- [46] R. Hill. A theory of the yielding and plastic flow of anisotropic metals. *Proc. Roy. Soc. London*, 193:281–297, 1948.
- [47] R. Hill. Elastic properties of reinforced solids: some theoretical principles. *J. Mech. Phys. Solids*, 11, 1963.
- [48] J.E. Hockett and O.D. Sherby. Large strain deformation of polycrystalline metals at low homologous temperatures. *J. Mech. Phys. Sol.*, 23:87–98, 1975.
- [49] J.H. Hollomon. Tensile deformation. *Trans. Met. Soc. AIME*, 162, 1945.
- [50] P. Hora. Advanced constitutive models as precondition for an accurate FEM-simulation in forming applications. Keynote presentation at 5th LS-DYNA Anwenderforum, Ulm, 2006.
- [51] N. Iosipescu. New accurate procedure for single shear testing of metals. *J. Mater.*, 2 (3):537–566, 1967.
- [52] G.R. Johnson and W.H. Cook. A constitutive model and data for metals subjected to large strains, high strain rates and high temperatures. In *Proc. 7th Int. Symp. on Ballistics*. 1983.
- [53] N. Jones. *Structural impact*. Cambridge University Press, 1997.

- [54] N. Jones. Part I - Structural impact. In *Crashworthiness - Energy management and occupant protection*, pages 1–82. CISM - International centre for mechanical sciences, 2001.
- [55] A. Karimi, M. Navidnakhsh, H. Yousefi, and M. Alizadeh. An experimental study on the elastic modulus of gelatin hydrogels using different stress–strain definitions. *J. Thermoplast. Comp. Mater.*, pages 1–12, 2014. in press.
- [56] J.R. Kattus and C.L. Dotson. Tensile, fracture, and short-time creep properties of aircraft-structural materials at very high temperatures after rapid heating. Southern Research Institute, december 1955. WADC TR 55-391.
- [57] T. Kayser. *Characterization of microstructure in aluminum alloys based on electron backscatter diffraction*. PhD thesis, Technische Universität Dortmund, 2011.
- [58] A. Kelly and G.J. Davies. The principles of the fibre reinforcement of metals. In *Metallurgical Reviews*, volume 10, pages 1–77. Institute of Metals London, 1965.
- [59] M. Kleiner and A.E. Tekkaya, editors. *Tätigkeitsbericht 2014*. Institut für Umformtechnik und Leichtbau, 2014.
- [60] J. Koplik and A. Needleman. Void growth and coalescence in porous plastic solids. *Int. J. Solids Struct.*, 24:835–853, 1988.
- [61] L.D. Landau and E.M. Lifschitz. *Elastizitätstheorie*. Akademie-Verlag Berlin, 1989.
- [62] K. Lange. *Umformtechnik*. Springer-Verlag Berlin Heidelberg New York, 2nd edition, 2002.
- [63] P. Larour. *Strain rate sensitivity of automotive sheet steels: influence of plastic strain, strain rate, temperature, microstructure, bake hardening and pre-strain*. PhD thesis, RWTH Aachen, 2010.
- [64] Y.-W. Lee. *Fracture prediction in metal sheets*. PhD thesis, Massachusetts Institute of Technology MIT, 2005.
- [65] J. Lemaitre. *Handbook of materials behavior models*. Acad. Press San Diego, 2001.
- [66] Livermore Software Technology Corporation (LSTC). *LS-DYNA Theory Manual*. LSTC, Livermore, CA, 2006.
- [67] Livermore Software Technology Corporation (LSTC). *LS-DYNA Keyword User’s Manual - Volume II Material Models, Version 971 R6.0.0*. LSTC, Livermore, CA, 2012.

- [68] P. Ludwik. *Elemente der Technologischen Mechanik*. Verlag von Julius Springer Berlin, 1909.
- [69] M.A. Macaulay. *Introduction to impact engineering*. Chapman & Hall, London, 1987.
- [70] A. Macke, B.F. Schultz, and FASM Pradeep Rohatgi. Metal matrix composites: offer the automotive industry an opportunity to reduce vehicle weight, improve performance. *Adv. Mater. Process.*, 03:19–23, 2012.
- [71] D.B. Marshall. An indentation method for measuring matrix-fibre frictional stresses in ceramic composites. *J. Am. Ceram. Soc.*, 67:259–260, 1984.
- [72] D. Matias Bóveda. Determination of a failure model for steel wire reinforced aluminum. Diploma thesis, Technische Universität München, 2013.
- [73] F.L. Matthews and R.D. Rawlings. *Composite materials: engineering and science*. Chapman & Hall, 1st edition, 1994.
- [74] F.A. McClintock. A criterion for ductile fracture by the growth of holes. *J. Appl. Mech.*, 35:363–371, 1968.
- [75] C. Möck. *Stahldrahtverstärkte Aluminiumverbundkörper mit und ohne äußere Vorspannungen*. PhD thesis, Universität Karlsruhe, 1982.
- [76] M. Meissner. Experimentelle und CAE-gestützte Untersuchung des Schädigungsverhaltens der unidirektional federstahldrahtverstärkten Aluminiumlegierung EN AW-6082 bei variierendem Verstärkungsanteil. Term paper, Karlsruher Institut für Technologie, 2010.
- [77] M. Merzkirch. *Verformungs- und Schädigungsverhalten der verbundstranggepressten, federstahldrahtverstärkten Aluminiumlegierung EN AW-6082*. PhD thesis, Karlsruher Institut für Technologie, 2012.
- [78] D.P. Moon and J.E. Campbell. Effects of moderately high strain rates on the tensile properties of metals. Defense Metals Information Center, Battelle Memorial Institute, December, 18th 1961. DMIC Memorandum 142.
- [79] A. Morasch. Nichtlineares Verhalten von werkstoffhybriden Faserverbundbauteilen. Diploma thesis, Technische Universität München, 2010.
- [80] A. Morasch, D. Matias, and H. Baier. Material modelling for crash simulation of thin extruded aluminium sections. *Int. J. Crash.*, 19:500–513, 2014.
- [81] A. Morasch, A. Reeb, K.A. Weidenmann, H. Baier, and V. Schulze. Characterization of debonding strength in steel-wire-reinforced aluminum and its influence on material fracture. *Eng. Frac. Mech.*, 141:242–259, 2015.

- [82] A. Morasch, M. Wedekind, D. Matias, and H. Baier. Thermo-mechanical behavior and material failure of steel wire reinforced aluminum. *Proc. CIRP*, 18:144–149, 2014.
- [83] K. Nahshon and J.W. Hutchinson. Modification of the Gurson Model for shear failure. *Eur. J. Mech. A-Solids*, 27:1–17, 2008.
- [84] P. Neff, I.-D. Ghiba, and J. Lankeit. The exponentiated Hencky-logarithmic strain energy. part i: Constitutive issues and rank-one convexity. *J. Elast.*, pages 1–92, 2015.
- [85] J. Peirs, P. Verleysen, W. Van Paepegem, and J. Degrieck. Novel pure-shear sheet specimen geometry for dynamic material characterisation. In *9th International Conference on the Mechanical and Physical Behaviour of Materials under Dynamic Loadings - DYNAM - Brussels*, pages 35–41. 2009.
- [86] N. Peixinho. Geometry and material strategies for improved management of crash energy absorption. In *New trends in mechanism and machine science — From fundamentals to industrial applications*, pages 251–260. Springer International Publishing Switzerland, 2015.
- [87] H. Petryk. Plastic instability: Criteria and computational approaches. *Arch. Comput. Method. E.*, 4:111–151, 1997.
- [88] T. Pfaffinger. Parameteridentifikation von analytischen Fließkurvenmodellen bei hohen Dehnungen. Term paper, Technische Universität München, 2014.
- [89] R.C. Picu, G. Vincze, F. Ozturk, J.J. Gracio, F. Barlat, and A.M. Maniatty. Strain rate sensitivity of the commercial aluminum alloy AA5182-O. *Mater. Sci. Eng. A*, 390:334–343, 2004.
- [90] H.R. Piehler. Plastic deformation and failure of silver-steel filamentar composites. In *Trans. Met. Soc. AIME*, volume 233, pages 12–16. 1965.
- [91] K. Pöhlandt and E. Lach. Beitrag zur Prüfung metallischer Werkstoffe im Torsionsversuch. *Rheol. Acta*, 20:536–541, 1981.
- [92] K. Pöhlandt, K. Lange, and M. Zucko. Concepts and experiments for characterizing plastic anisotropy of round bars, wires and tubes. *Steel Res.*, 69:170–174, 1998.
- [93] K. Pöhlandt, A.E. Tekkaya, and E. Lach. Prüfung des plastischen Verhaltens metallischer Werkstoffe in Torsionsversuchen. *Z. Werkstofftech.*, 14:181–189, 1983.
- [94] Prolam, alu profiles & components. Technical data sheet of alloy 6060 and aluminium profile. Online document, http://www.pro-lam.net/eur-1/download/parte1_en.pdf, 2015. Visited on 18th of September 2015.

- [95] A.-R. Ragab and S.E. Bayoumi. *Engineering solid mechanics: fundamentals and applications*. CRC press LLC, 1999.
- [96] M.V. Rastegaev. Neue Methode der homogenen Stauchung von Proben zur Bestimmung der Fließspannung und des Koeffizienten der inneren Reibung (russ.). *Zav. Lab.*, page 354, 1940.
- [97] P. Redanz, N.A. Fleck, and R.M. McMeeking. Failure of a porous solid from a deep notch. *Int. J. Fracture*, 88:187–2003, 1998.
- [98] J.R. Rice and D.M. Tracey. On the ductile enlargement of voids in triaxial stress fields. *J. Mech. Phys. Solids*, 17:201–217, 1969.
- [99] A. Rusinek, R. Zaera, and J.R. Klepaczko. Constitutive relations in 3-D for a wide range of strain rates and temperatures - Application to mild steels. *Int. J. Sol. Struct.*, 44:5611–5634, 2007.
- [100] M. Schikorra. *Modellierung und simulationsgestützte Analyse des Verbundstrangpressens*. PhD thesis, Technische Universität Dortmund, 2006.
- [101] F. Schmeing, M. Feucht, and A. Haufe. Forming and crash induced damage evolution and failure prediction - Part I: Extension of the Gurson model to forming simulations. In *6th LS-DYNA Anwenderforum, Frankenthal*, pages H-I-1 – H-I-10. DYNAMore GmbH, 2007.
- [102] M. Schomäcker, M. Schikorra, and M. Kleiner. Verbundstrangpressen. In *Fortschritt-Berichte VDI - Integration von Umformen, Trennen und Fügen für die flexible Fertigung von leichten Tragwerkstrukturen. Ergebnisbericht der Phase I*. VDI Verlag, 2007. Reihe 2 Nr. 661.
- [103] K.-H. Schwalbe, I. Scheider, and A. Cornec. SIAM CM 09 - The SIAM method for applying cohesive models to the damage behaviour of engineering materials and structures. GKSS Forschungsbericht 2009/1, 2009.
- [104] R.G. Snyder. Human survivability of extreme impacts in free-fall. Presentation at the 34th Annual Aerospace Medical Association meeting in Los Angeles, CA, April 29 – May 2, 1963, 1963.
- [105] Southern Research Institute. Short time elevated-temperature mechanical properties of metals under various conditions of heat treatment, heating, exposure time, and loading. Summary report to Army Ballistic Missile Agency, July, 17th 1959. Contract No. DA-01-009-ORD-491.
- [106] T. Stöckl. Versagensvorgänge in stahldrahtverstärktem Aluminium unter Berücksichtigung von Grenzflächencharakteristika. Master's thesis, Technische Universität München, 2014.

- [107] D.T. Sun, B. Voss, and W. Schmitt. Numerical prediction of ductile fracture resistance behavior based on micromechanical models. In *Defect assessments in components - fundamentals and applications ESIS/EGF9*, pages 447–458. Mechanical Engineering Publications London, 1991.
- [108] H.W. Swift. Plastic instability under plane stress. *J. Mech. Phys. Sol.*, 1:1–18, 1952.
- [109] G.I. Taylor and H. Quinney. The latent energy remaining in a metal after cold working. *Proc. Roy. Soc. Lon. - Series A*, 143:307–326, 1934.
- [110] S.P. Timoshenko and J.M. Gere. *Theory of elastic stability*. McGraw-Hill, 2nd edition, 1963.
- [111] V. Tvergaard. Influence of voids on shear band instabilities under plane strain conditions. *Int. J. Fract.*, 17:389–407, 1981.
- [112] V. Tvergaard and A. Needleman. Analysis of the cup-cone fracture in a round tensile bar. *Acta. Metall.*, 32:157–169, 1983.
- [113] U.S. Census Bureau. Statistical Abstract of the United States - Table 1104. Traffic Fatalities by State: 1990 to 2009. Census online document, <http://www.census.gov/compendia/statab/2012/tables/12s1104.pdf>, 2012. Visited on 20th of August 2015.
- [114] E. Voce. The relationship between stress and strain for homogeneous deformations. *J. Inst. Metals*, 74:537–562, 1948.
- [115] F. Vollertsen and S. Vogler. *Werkstoffeigenschaften und Mikrostruktur*. Carl Hanser Verlag München Wien, 1989.
- [116] M. Vrh, M. Halilović, and B. Štok. Characterization of mechanical behaviour of sheet metal: hardening at large strains and anisotropy identification. *AIP Conf. Proc. 1353*, pages 1441–1446, 2011.
- [117] J. Wang. Revision to paper “Plane strain transversely anisotropic analysis in sheet metal forming simulation using 6-component Barlat yield function”. Personal communication with author, April 15, 2013. Discussion and revision to the published paper.
- [118] J. Wang and J. Sun. Plane strain transversely anisotropic analysis in sheet metal forming simulation using 6-component Barlat yield function. *Int. J. Mech. Mater. Des.*, 8:327–333, 2012.
- [119] S. Weber. Crashverhalten von Stauchrohren aus unverstärkten und verstärkten Strangpressprofilen. Term paper, Technische Universität München, 2011.

- [120] A. Weck and D.S. Wilkinson. Experimental investigation of void coalescence in metallic sheets containing laser drilled holes. *Acta Mater.*, 56:1774–1784, 2008.
- [121] M. Wedekind. *Charakterisierung von Steifigkeit und Festigkeit heterogen verstärkter Verbundstrangpressprofile*. PhD thesis, Technische Universität München, 2013.
- [122] E.J. Wehrle. *Design optimization of lightweight space frame structures considering crashworthiness and uncertainty*. PhD thesis, Technische Universität München, 2015.
- [123] E.J. Wehrle, Q. Xu, and H. Baier. Investigation, optimal design and uncertainty analysis of crash-absorbing, extruded aluminum structures. *Procedia CIRP*, 18:27–32, 2014.
- [124] K.A. Weidenmann. Werkstoffsysteme für verbundstranggepreßte Aluminiummatrixverbunde. In *Schriftenreihe Werkstoffwissenschaft und Werkstofftechnik*, volume 33. Shaker Verlag, 2006.
- [125] K.A. Weidenmann, E. Kerscher, V. Schulze, and D. Löhe. Characterization of the interfacial properties of compound-extruded lightweight profiles using the push-out technique. *Mater. Sci. Eng. A*, 424:205–211, 2006.
- [126] H. Werner and H. Gese. Zur Bedeutung der dehnratenabhängigen Werkstoffkennwerte in der Crashsimulation. In *Kennwertermittlung für die Praxis*. Wiley-VCH, 2002.
- [127] T. Wierzbicky, Y. Bao, Y.W. Lee, and Y. Bai. Calibration and evaluation of seven fracture models. *Int. J. Mech. Sci.*, 47:719–743, 2005.
- [128] J. Woodthorpe and R. Pearce. The anomalous behaviour of aluminium sheet under balanced biaxial tension. *Int. J. Mech. Sci.*, 12:341, 1970.
- [129] M.-H. Yu. Advances in strength theories for materials under complex stress state in the 20th century. *Appl. Mech. Rev.*, 55:169–218, 2002.
- [130] M.-H. Yu. *Unified strength theory and its applications*. Springer-Verlag Berlin Heidelberg, 2004.
- [131] L. Yun. Uniaxial true stress–strain after necking. *AMP J. of Techn.*, 5:37–48, 1996.
- [132] D. Zaffino. Characterization of reinforced aluminium extrusion profiles. Diploma thesis, Technische Universität München and Università di Pisa, 2009.

- [133] M.F. Zäh, A.E. Tekkaya, M. Langhorst, M. Ruhstorfer, A. Schober, and D. Pietzka. Experimental and numerical investigation of the process chain from composite extrusion to friction stir welding regarding the residual stresses in composite extruded profiles. *Prod. Eng. Res. Devel.*, (3):353–360, 2009.
- [134] H. Zarei. *Experimental and numerical investigation of crash structures using aluminum alloys*. PhD thesis, Gottfried Wilhelm Leibniz Universität Hannover, 2008.
- [135] F.J. Zerilli and R.W. Armstrong. Dislocation-mechanics-based constitutive relations for material dynamics calculations. *J. Appl. Phys.*, 61:1816–1825, 1987.
- [136] K.S. Zhang and Z.H. Li. Numerical analysis of the stress–strain curve and fracture initiation for ductile material. *Eng. Frac. Mech.*, 49:235–241, 1994.
- [137] Z.L. Zhang. A sensitivity analysis of material parameters for the Gurson constitutive model. *Fatigue Fract. Eng. Mater. Struct.*, 29:364–383, 1999.
- [138] M. Źyczkowski. *Combined loadings in the theory of plasticity*. Polish scientific publisher, 1981.

A. Appendix

A.1. Mass-specific bending stiffness – SWRA in comparison to non-reinforced aluminum

The mass-specific bending stiffness S_ρ comprises of the geometrical bending moment of inertia I times the material's elasticity E , divided by the material's density.

$$S_\rho = \frac{EI}{\rho}. \quad (\text{A.1})$$

For the aluminum I-beam shown in figure 2.2, the geometrical moment of inertia is

$$I_{\text{Al}} = \frac{t \cdot (b - 2t)^3}{12} + 2 \cdot \left(\frac{a \cdot t^3}{12} + \left(\frac{b - t}{2} \right)^2 \cdot a \cdot t \right). \quad (\text{A.2})$$

The moment of inertia of the embedded steel wires is

$$I_{\text{St}} = \frac{\pi}{4} \cdot r_w^4 + \pi \cdot r_w^2 \left(\frac{b - t}{2} \right)^2. \quad (\text{A.3})$$

The mass-specific bending stiffness of the aluminum section, thus, is

$$S_{\rho, \text{Al}} = \frac{E_{\text{Al}} \cdot I_{\text{Al}}}{\rho_{\text{Al}}}. \quad (\text{A.4})$$

For the SWRA section with a number of n wires and a resulting wire content ϕ , the mass-specific bending stiffness is

$$S_{\rho, \text{SWRA}} = \frac{\sum_i E_i \cdot I_i}{\rho_{\text{Al}} + (\rho_{\text{St}} - \rho_{\text{Al}}) \cdot \phi_w}, \quad (\text{A.5})$$

with the sum over the bending stiffness of the aluminum matrix and the steel wires

$$S_{\rho, \text{SWRA}} = \frac{E_{\text{Al}} \cdot I_{\text{Al}} + n \cdot (E_{\text{St}} - E_{\text{Al}}) \cdot I_{\text{St}}}{\rho_{\text{Al}} + (\rho_{\text{St}} - \rho_{\text{Al}}) \cdot \phi_w}. \quad (\text{A.6})$$

Here, the bracket $(E_{\text{St}} - E_{\text{Al}})$ takes into account, that the steel-wires replace the aluminum material, so that the increased stiffness is due to the difference in the Young's moduli.

A.2. Temperature-dependent elasto-plastic material properties and CTE of aluminum matrix and steel wire

A.2.1. Temperature-dependent CTE

The averaged CTE of aluminum alloy EN AW-6060 is given by [94] and the corresponding tabulated data is given in table A.1. The measured CTE of the steel alloy 1.4310, extrapolated with Grüneisen's equation, is taken from [79] and shown in figure A.1.

Table A.1.: Temperature-dependent CTE of aluminum alloy EN AW-6060 [94]

Temperature range	CTE in 10^{-6} 1/K
20°C to 100°C	23
20°C to 200°C	24
20°C to 300°C	25

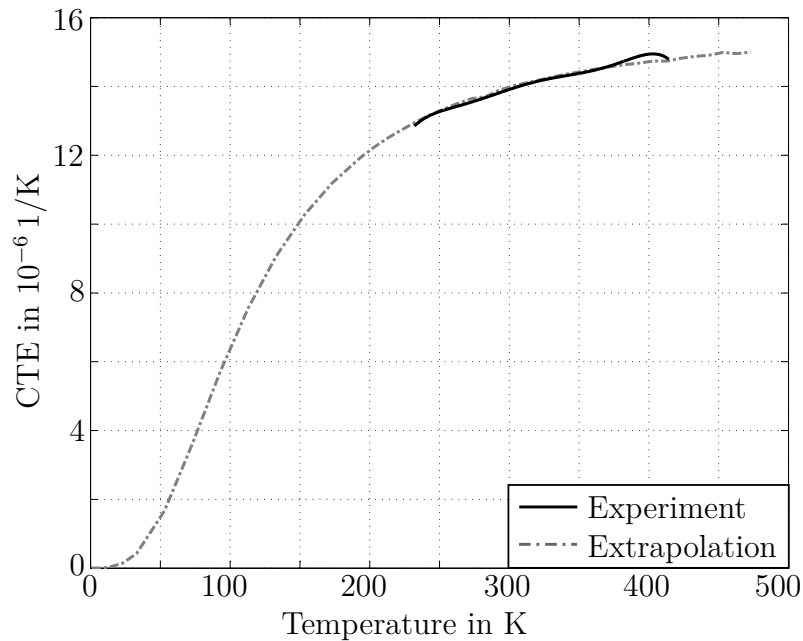


Figure A.1.: Temperature-dependent CTE of the steel wire alloy 1.4310 — adapted from [79]

A.2.2. Temperature-dependent elasto-plastic material properties

The temperature-dependent elasto-plastic properties of the aluminum matrix are evaluated from tensile tests at temperatures from $0^{\circ}\text{C} \leq T \leq 300^{\circ}\text{C}$, which were courteously provided by A. Reeb and M. Merzkirch¹. Based on the test data, the temperature-dependent Young's modulus and yield strength were evaluated. A plastic hardening for small plastic strains as occurring in the cooling simulation is considered by a plastic tangent modulus. The derived data is summarized in table A.2.

The steel wire is considered to behave fully elastic during cooling, so that only a temperature dependent Young's modulus has to be considered. Tabulated data on the temperature-dependent Young's modulus of austenitic stainless steel similar to 1.4310 is given by [8] and added to table A.2.

Table A.2.: Tabulated data on temperature-dependent elasto-plastic material data of EN AW-6060 and austenitic stainless steel [8]

Temperature	Young's modulus in MPa	Yield strength $R_{p0.2}$ in MPa	Plastic tangent modulus in MPa
EN AW-6060			
20°C	64980	70	1774
100°C	63377	70	1552
200°C	58497	70	1364
300°C	50338	60	1358
Austenitic stainless steel			
20°C	195000		
100°C	192000		
200°C	184000	fully elastic model for cooling simulation	
250°C	180000		
300°C	176000		

A.3. Geometry of the dynamic tensile test specimen

Figure A.3 shows the geometry of the tensile test specimen used for the characterization of the strain rate hardening of the aluminum alloy EN AW-6082.

¹A. Reeb and M. Merzkirch, Karlsruhe Institute of Technology, Karlsruhe

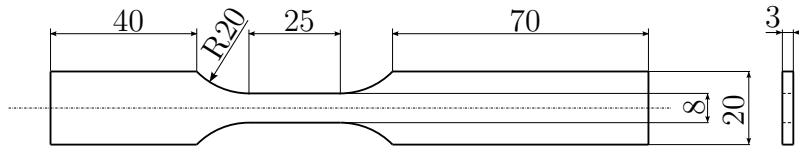
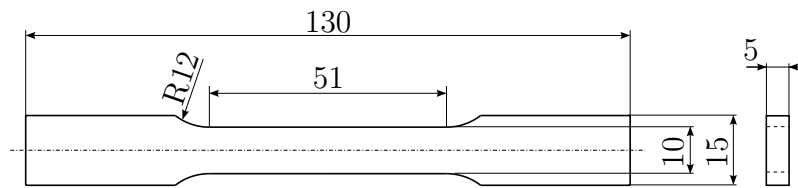


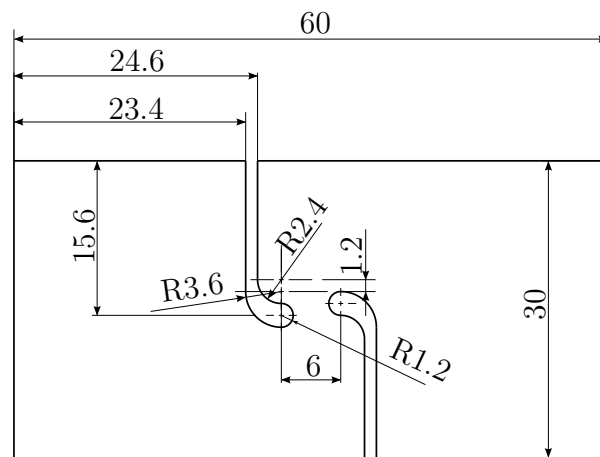
Figure A.2.: Geometry of dynamic tensile test specimen

A.4. Geometry of flat tensile specimen and flat shear specimen used for identification of the parameters of the shear-modified GTN model

Figure A.3(a) shows the geometry of the flat tensile specimen, figure A.3(b) the geometry of the flat shear specimen.



(a) Tensile test specimen



(b) Flat shear specimen

Figure A.3.: Specimens for determination of GTN model parameters

A.5. Age hardening of EN AW-6060T4(F)

The simulations of the bolt-pull-out tests in chapter 5 show a consistently under-predicted force-level in comparison to the experimental data. This was attributed

mainly to an age hardening of the aluminum matrix during the time between experimental material characterization and the bolt-pull-out tests (about 8 months). Additional layered-compression tests according to DIN 50106 [32] were performed 20 months after a first evaluation of the strain hardening curve had been done by tensile tests. The comparison of evaluated strain hardening curves in figure A.4 shows, that the alloy was not fully age hardened at the time of material characterization, which was taken into account in the present thesis.

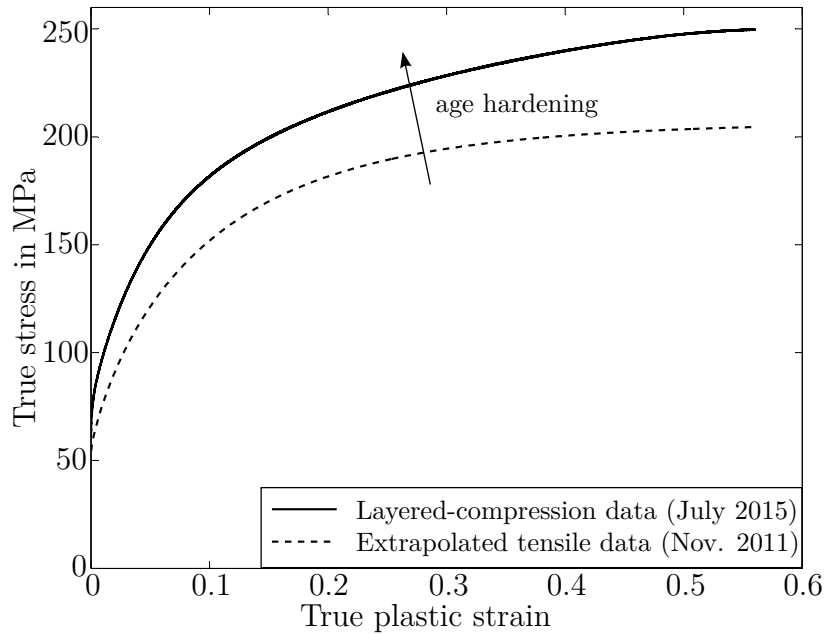


Figure A.4.: Derived strain hardening curves from tensile tests at the time of material characterization and from layered-compression tests 20 months after material characterization